

Constraining Primordial Gravitational Waves with BICEP/Keck Array Telescopes and Developing the BICEP Array Housekeeping System

A dissertation submitted to the
Graduate School of the University of Cincinnati
in partial fulfillment of the requirements
for the degree of Doctor of Philosophy in the Department of Physics
of the McMicken College of Arts and Sciences

by

Steven Michael Palladino
July 2021

supervised by
Dr. Colin Bischoff
Committee Member: Dr. Matthew Bayliss, Physics
Committee Member: Dr. Alexandre Sousa, Physics
Committee Member: Dr. Hans-Peter Wagner, Physics

Abstract

The Cosmic Microwave Background (CMB) has provided a wealth of information since its discovery in the 1960s. The blackbody nature and the temperature anisotropies of the CMB have helped form the current cosmological paradigm of a hot Big Bang and the Λ CDM model of the Universe. We are now looking to the polarization field of the CMB for answers about the early Universe. The theory of Cosmic Inflation postulates that the Universe went through a period of exponential expansion in the earliest moments. This theory generally predicts a stochastic background of primordial gravitational waves which would leave a faint *B*-mode pattern in the polarization of the CMB.

The BICEP/Keck Array telescopes are small aperture multi-frequency microwave polarimeters at the Amundsen–Scott South Pole Station. These telescopes continuously observe a $\sim 1\%$ patch of the Southern sky targeting degree angular scales where the amplitude of the primordial gravitational waves is predicted to peak. The multi-frequency observation allows for the disentanglement of galactic foreground signals from the CMB signal. To date, these experiments provide the tightest constraints on the tensor-to-scalar ratio at $r < 0.07$ at 95% confidence.

The discussion of this thesis is split into two parts. In the first part, it will discuss the design, development, and performance of the BICEP Array Housekeeping system. The Housekeeping system is an electronics data acquisition system designed to read out the thermistors of the cryogenically cooled receivers and provide temperature control. The second part of the thesis will discuss high level data analysis using a multi-component model of

the bandpower data. In particular, there will be discussion of a novel minimum variance quadratic estimator used as an alternative to the maximum likelihood estimator.

Acknowledgements

This dissertation was not written in a vacuum. It is the culmination of many people's work and sacrifice. This is true, not just of the content, but in every aspect of life that went into making it. Many people have given me support and love in an abundance of ways. This simple recognition of their contributions does not do their acts justice. Regardless, I hope this humble acknowledgment shows a fraction of my gratitude.

First, I would like to thank those I met on my journey through grad school. I would like to thank my advisor, Colin, who has always been readily available for questions and guidance throughout the whole process. I would like to thank my colleague and friend, Caterina, who taught me about science as well as Italian culture. To Denis, Justin, and Sam – you made my time at the South Pole meaningful and enjoyable even on the harsh continent. To Brian, Carrie, Josh, and Jon – I would like to thank you for helping me navigate Cincinnati and my years of grad school.

I would also like to thank all of those close to me who have been a continual source of support, encouragement, joy, and friendship. To the 'Chicago Boys' and their associates, in no particular order: James, David, Kory, Yaphet, Kevin, Micah, Shang, John, Christian, Jack, and Derek – Thank you for all of the times you provided a place to stay, a drink, a meal, or a free shirt. I will always be grateful and I hope to celebrate with you in all stages of life. To Claire – Getting to know you has been the best thing to come of this difficult year. Thank you for believing in me and providing constant love and support. I have enjoyed our many laughs, adventures, and meals together and I look forward to the many more to come.

Finally, I would like to thank my family for their unwavering love and support. To my siblings, Lisa, Matt, Andrew, Nathan, and their families – Thank you for all of the times we spent around a meal, or at the beach, or camping, or playing board games. You were always there for me when I needed you. To my mom and dad – There is absolutely no way I would have made it through this without your love. You have always welcomed me home with open arms and a full plate. I can never pay back what you have done for me but I hope to be able to pay it forward.

Contents

1	Introduction	1
1.1	Standard Cosmology	2
1.2	Cosmic Microwave Background	5
1.2.1	Blackbody	6
1.2.2	Temperature Anisotropies	6
1.2.3	Polarization	10
1.3	Inflation	15
1.3.1	The Horizon Problem	16
1.3.2	The Flatness Problem	17
1.3.3	Single-field Slow-roll Inflation	19
1.3.4	Perturbations	20
1.4	Foregrounds	23
1.4.1	Dust	24
1.4.2	Synchrotron	24
1.4.3	Gravitational Lensing	25
2	BICEP/Keck Experiment	29
2.1	Program History	29
2.2	Observing	31
2.2.1	Site	31

2.2.2	Strategy	33
2.3	Receiver Design	35
2.3.1	Cryostat	35
2.3.2	Detectors	37
2.3.3	Readout	39
2.3.4	Optics	40
2.4	Raw Data to Power Spectra	42
2.4.1	Time Ordered Data	42
2.4.2	Maps	45
3	BICEP Array Housekeeping Electronics	57
3.1	Design Overview	58
3.2	Backpack	61
3.2.1	Power Supply	63
3.3	Daughter Cards	63
3.3.1	Heater Amp	67
3.3.2	Heater Buffer	67
3.3.3	JFET	69
3.3.4	Cernox	69
3.3.5	Diode	72
3.3.6	NTD Overview	73
3.4	Auxiliary Readout	77
3.5	Performance and Improvements	78
3.5.1	Cernox and NTD Comparison	78
3.5.2	BA and Keck NTD Comparison	79
3.5.3	NTD Tuning	80
3.5.4	Cernox Output Gain	80
3.5.5	High Impedance Cernox Circuits	82

3.5.6	Dummy Loads	84
3.5.7	NTD Aliasing	84
3.5.8	BA NTD Scan Sync	87
4	Multi-component Data Analysis	91
4.1	Multi-component Model	93
4.2	Bandpower Covariance Matrix	95
4.2.1	Bandpower Covariance Matrix Conditioning	95
4.2.2	BPCM Scaling	99
4.3	Maximum Likelihood Search	103
4.3.1	ML Search with Reduced Number of Sims	105
4.3.2	Bias from Subsets of Sims	107
4.3.3	Exclude Sim Realization	109
4.3.4	BK Noise Correlations in BPCM	109
4.4	Quadratic Estimator	111
4.4.1	Formalism	111
4.4.2	Creating an Estimator	113
4.4.3	Estimator on BK15 sims	115
4.4.4	Estimating Scaling Parameters	117
4.4.5	Iterative Method	119
4.4.6	Alternative Foreground Sims	122
4.4.7	Direct Likelihood	123
4.5	Systematic Errors with CMB-S4	126
4.5.1	Uncorrelated Bandcenter Error	127
4.5.2	Correlated Bandcenter Error	128
4.5.3	Additive Systematic Errors	128
5	Conclusion	135

A	Appendix	151
A.1	NTD Tuning	151
A.2	Cernox Daughter Card Flavors	154

List of Figures

1.1	Hubble’s observation of the expanding Universe	3
1.2	FIRAS observation of the CMB blackbody	7
1.3	Planck satellite CMB temperature map	8
1.4	Planck temperature angular power spectrum of the CMB	9
1.5	Stokes parameters	11
1.6	Angular power spectrum of all CMB fields	13
1.7	Polarization from Thomson Scattering	14
1.8	Polarization from scalar perturbations	15
1.9	Polarization from tensor perturbations	16
1.10	E -mode and B -mode polarization	17
1.11	Inflation conformal diagram	18
1.12	Toy representation of a scalar inflation field	20
1.13	Density fluctuations during Inflation	21
1.14	Current BK r constraints	23
1.15	Foreground scaling with frequency and ℓ	25
1.16	Gravitational lensing example	26
2.1	BICEP3 and BICEP Array viewed from the roof	31
2.2	DSL and MAPO observatories	32
2.3	BK observing field	33

2.4	Motion of the telescope during one scanset	35
2.5	BICEP Array cryostat	36
2.6	Conceptual drawing of a bolometer	38
2.7	BICEP Array optical design	41
2.8	BA detector data from one scanset	43
2.9	Differences of elliptical Gaussian beams	49
2.10	Differential beam parameters for deprojection	51
2.11	BK15(150GHz) Fourier maps	55
3.1	BICEP2 Housekeeping block diagram	59
3.2	Bicep Array Housekeeping block diagram	60
3.3	BA Motherboard layout block diagram	64
3.4	BA Reroute layout block diagram	65
3.5	Two views of the Backpack enclosure model	66
3.6	Cernox daughter card PCB design and real product	66
3.7	Block diagram of the Heater Amp daughter card	68
3.8	Block diagram of the Heater Buffer daughter card	68
3.9	Block diagram of the JFET Power daughter card	70
3.10	Block diagram of the Cernox daughter card	71
3.11	Block diagram of the Diode daughter card	72
3.12	Topology of the NTD bridge circuit	74
3.13	Flow diagram of NTD modules	75
3.14	Block diagram of the NTD Bias daughter card	76
3.15	Block diagram of the NTD Lock-in daughter card	77
3.16	Cernox and NTD noise comparison	79
3.17	BA and Keck Array NTD noise comparison	80
3.18	Logarithmic Cernox output	81
3.19	Block diagram of the Cernox log amp	81

3.20	Output of Cernox servo-loop simulation	83
3.21	BA NTD aliasing example	85
3.22	Lab test PSD comparison of NTD Lock-in board versions	86
3.23	Operational PSD comparison of NTD Lock-in board versions	87
3.24	BA NTD full scanset temperature TODs and PSDs	89
3.25	NTD focal plane temperature averaged over halfscans	90
4.1	BPCM noise correlation masks for signal-noise terms	98
4.2	Fractional difference in BPCM scaling methods	104
4.3	Comparison of the BPCMs constructed from different numbers of sims . . .	106
4.4	Rlz-by-rlz difference of ML search with reduced number of sims	108
4.5	Rlz-by-rlz difference of ML search from sim subsets	109
4.6	Rlz-by-rlz difference of ML search when excluding sim	110
4.7	Rlz-by-rlz difference of ML search with and without noise correlation	111
4.8	Quadratic estimators of the amplitude parameters on the BK15 sims	116
4.9	Quadratic estimators of the dust scaling parameters on the BK15 sims . . .	118
4.10	Iterative quadratic estimator on ‘gdust’ BK15 sims (histograms)	120
4.11	Iterative quadratic estimator on ‘gdust’ BK15 sims (iteration mean and stan- dard deviation)	121
4.12	Quadratic estimator likelihood histograms	123
4.13	KS statistic for likelihood pdf fits	125
4.14	Quadratic estimator likelihood	130
4.15	Quadratic estimator confidence interval for BK15 and BK18lf	131
4.16	BK15 quadratic estimator likelihood curves	131
4.17	BK15 quadratic estimator real data likelihood curve	132
4.18	Bias on r caused by uncorrelated bandcenter uncertainties	132
4.19	Bias on r caused by perfectly correlated bandcenter uncertainties	133
4.20	Bias on r caused by various types of additive systematics	134

5.1	BICEP/Keck r sensitivity projections	137
A.1	NTD Bias daughter card PCB with tuning labels	152
A.2	NTD Phase tuning	153
A.3	Cernox Flavor Circuit Diagram (Servo-loop part 1)	156
A.4	Cernox Flavor Circuit Diagram (Servo-loop part 2)	156
A.5	Cernox Flavor Circuit Diagram (Post Lock-in)	157

List of Tables

2.1	BK Collaboration receiver history	30
3.1	BA HK daughter card channels by cyrostat MDM connector	62
3.2	High impedance Cernox flavors	83
4.1	Standard deviation from ML search with reduced number of sims	107
4.2	BK15 comparison of the quadratic estimator and ML search (amplitude parameters)	117
4.3	BK15 comparison of the quadratic estimator and ML search (dust scaling parameters)	119
4.4	Modified sims values for direct likelihood calculation.	124
A.1	Cernox Flavor Circuit Components	155

Chapter 1

Introduction

Cosmology is the study of the origins of the Universe and how it evolved into what we see today. The Big Bang theory is the current cosmological paradigm describing the origins of the Universe. The contents and interactions used to model the Universe is known as Λ CDM cosmology. In this model, the Universe is comprised primarily of dark energy (Λ) and cold dark matter (CDM). These theories, along with initial conditions, seem to describe the physics of the Universe well. However, as our technology and measurements improve, these standard theories of cosmology do not completely describe the phenomena we observe.

The theory of Cosmic Inflation or simply Inflation, was introduced to describe some of the inconsistencies between standard cosmology and observation. In particular, the theory was presented to address the horizon problem, the flatness problem, and the magnetic monopole problem. By probing the polarization field of the Cosmic Microwave Background (CMB), the BICEP/Keck (BK) Collaboration seeks to constrain the level of primordial gravitational waves (PGWs). If detected, these waves, along with other observed phenomena, will provide very strong evidence in favor of Inflation.

In Chapter 1 of this dissertation, I will introduce some of the basics of standard Λ CDM cosmology. I will then discuss the CMB and how it is used as the primary probe for experimentally verifying Inflation. Lastly, I will discuss how Inflation is an extension of Big Bang

cosmology. Chapter 2 will be an overview of the BICEP/Keck experiments and the observation of the polarization of the CMB. Chapter 3 will describe, in detail, the Housekeeping (HK) subsystem of the BICEP Array experiment. Finally, Chapter 4 will be a collection of high level analyses using the BK Collaboration data in the form of bandpowers.

1.1 Standard Cosmology

Modern cosmology is built on the fundamentals of general relativity and the Cosmological Principle. The Cosmological Principle states that the Universe is spatially homogeneous and isotropic [1]. On large scales, the dynamics of the Universe are described by general relativity expressed through the Einstein Field Equations (EFE) [2]:

$$R_{\mu\nu} - \frac{1}{2}Rg_{\mu\nu} + \Lambda g_{\mu\nu} = \frac{8\pi G}{c^4}T_{\mu\nu} \quad (1.1)$$

Where $R_{\mu\nu}$ is the Ricci tensor, R is the Ricci Scalar, $g_{\mu\nu}$ is the metric tensor, Λ is the cosmological constant, and G is Newton's constant. $T_{\mu\nu}$ is the stress-energy tensor and under the spatial isotropic and homogeneous assumptions, can be modeled as a perfect fluid. The EFE relate the content of the Universe with the geometry of the space-time.

The Friedmann-Robertson-Walker (FRW) metric is the result of applying the Cosmological Principle with the formalism of general relativity. The FRW metric is expressed as:

$$ds^2 = c^2 dt^2 - a^2(t) \left(\frac{dr^2}{1 - kr^2} + r^2 d\theta + r^2 \sin^2 \theta d\phi^2 \right) \quad (1.2)$$

Where $c^2 dt^2$ describes the temporal component and the spatial component is described in spherical coordinates (r, θ, ϕ) with a spatial curvature, k . For a spatially flat universe, $k = 0$. In a universe with a positive curvature $k = +1$, which is sometimes referred to as closed or spherical. For a negative curvature $k = -1$, the universe is open or hyperbolic. The scale factor, $a(t)$, describes the expansion of the Universe with time. When the FRW metric is

applied to the EFE, the resulting equations are the well known Friedmann equations [3].

The first Friedmann (1.3) can be derived from the 00 or tt component.

$$H^2 = \left(\frac{\dot{a}}{a}\right)^2 = \frac{8\pi G\rho}{3} + \frac{\Lambda c^2}{3} - \frac{kc^2}{a^2} \quad (1.3)$$

Where H is Hubble's parameter which is used to describe the expansion rate of the Universe and ρ is the mass density. Figure 1.1 shows the first observations of Hubble indicating an expanding universe. The value of the Hubble parameter at the present moment is referred to as Hubble's constant: $H_0 = \dot{a}(t_0)/a(t_0)$ where t_0 is present day.

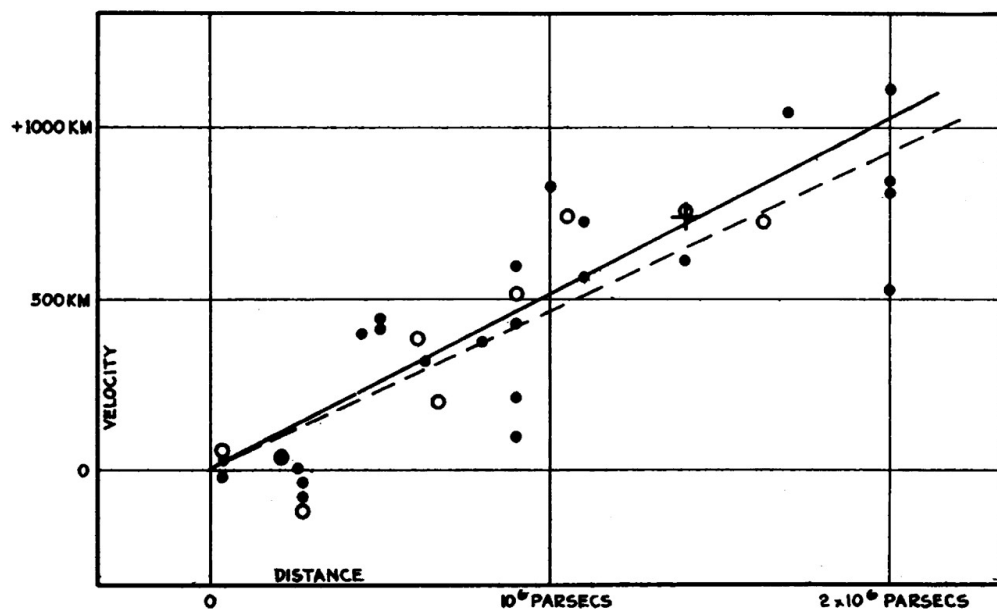


Figure 1.1: This figure from Hubble's observations [4] is the relationship between the radial velocity and distance of extra-galactic nebulae. Hubble's law ($v = H_0 D$) describes how the red-shifted velocity (v) of extra-galactic nebulae increases with the proper distance (D) and Hubble's constant (H_0). This was some of the first evidence that the Universe is dynamic and expanding.

The second Friedmann equation can be obtained by combining the first equation (1.3) with the spatial components of the EFE (1.1):

$$\dot{H} + H^2 = \frac{\ddot{a}}{a} = \frac{-4\pi G}{3} \left(\rho + \frac{3p}{c^2} \right) \quad (1.4)$$

Where p is the hydrostatic pressure term in the stress-energy tensor and the cosmological constant was absorbed for convenience. This equation describes the rate of acceleration of the Universe with respect to the mass-energy density and the fluid pressure. This equation is sometimes referred to as the *acceleration equation*.

If we consider the conservation of energy ($\nabla_\mu T^\mu_0 = 0$) and the FRW metric for an isotropic and flat universe, the energy density can be related to the scale factor [5]:

$$\dot{\rho} = -3\frac{\dot{a}}{a}(\rho + p) \quad (1.5)$$

The equations of state for the various content of the Universe can be expressed as $\omega = \frac{p}{\rho}$. Where $\omega = 0$ for non-relativistic matter, $\omega = 1/3$ for relativistic particles (radiation), and $\omega = -1$ for vacuum energy (Λ). With these in mind, the scaling for non-relativistic matter, radiation, and vacuum energy are, respectively:

$$\rho \propto a^{-3} \quad (1.6)$$

$$\rho \propto a^{-4} \quad (1.7)$$

$$\rho \propto a^0 \quad (1.8)$$

In other words, for non-relativistic matter, the density scales proportional to the volume increase. For radiation, the density scales proportional to the volume increase and the redshifting of the wavelength. The vacuum energy is constant with the expanding universe.

There is a critical density $\rho_c = \frac{3H^2}{8\pi G}$ which results in a spatially flat universe. The density parameter is often defined as the unitless density parameter, $\Omega \equiv \frac{\rho}{\rho_c}$. So now, $\Omega = 1$ corresponds to a spatially flat universe, $\Omega > 1$ corresponds to a positive geometry, and $\Omega < 1$ corresponds to a negative geometry. The first Friedmann Equation (1.3) can now be expressed as:

$$\frac{H^2}{H_0^2} = \Omega_{0,R}a^{-4} + \Omega_{0,M}a^{-3} + \Omega_{0,k}a^{-2} + \Omega_{0,\Lambda} \quad (1.9)$$

Where the densities are the fractional contents of the cosmic fluid: radiation (R), matter (M), curvature (k), and vacuum energy (Λ). $\Omega_{0,M}$ can be further split into baryonic and dark matter $\Omega_{0,M} = \Omega_{0,b} + \Omega_{0,d}$. The terms use the naught notation to indicate present day values. This equation describes the dynamics of an expanding universe according to standard cosmology.

1.2 Cosmic Microwave Background

The Big Bang theory postulates that the early universe was once much hotter and much denser than today. During this time, all of matter and energy were in a tightly coupled photon-baryon plasma (ionized hydrogen). As the Universe expanded, the temperature cooled proportional to the scale factor, $T \propto a^{-1}$. Eventually, the Universe was cool enough for protons and electrons to combine into neutral Hydrogen ($T \sim 3000K$); this epoch is referred to as Recombination. The idea of the lighter elements being produced in the early Universe (Big Bang nucleosynthesis) was first proposed in the famous $\alpha\beta\gamma$ paper in the 1940s [6].

After Recombination, the photons scattered one last time and began to free stream. These photons from the early Universe are referred to as the Cosmic Microwave Background (CMB). Because the Universe continued to expand, the photons went through a cosmological redshifting. This would decrease the temperature of the photons until being observed at a much lower temperature today [7]. The temperature decreases with the scale factor as $T \propto a^{-1}$. Cosmological redshifting (z) can then be related to the scale factor as $1+z = a_{now}/a_{then}$ which results in a redshift of $z \approx 1100$ and a current temperature of $T \approx 3K$.

Despite the CMB being predicted and calculated, at the time, there was little interest in pursuing any astronomical observations. It wasn't until the 1960s when the CMB was first observed by two radio astronomers working for Bell Labs. Arno Penzias and Robert Wilson built a telescope intended for radio astronomy and satellite communication. Upon observa-

tion, they discovered a consistent excess antennae loading of about $4K$ [8]. After further investigation and discussion, it was determined to be the CMB. Since this first observation of the CMB, there have been increasingly more accurate and precise measurements; current satellite measurements indicate the temperature of the CMB is $T = 2.72548 \pm 0.00057K$ [9].

1.2.1 Blackbody

The CMB resulted from a time in the early universe when all the matter and energy were in a tightly coupled plasma. As seen in Figure 1.2, the functional form of the CMB is extremely well described as a blackbody and Planck's law:

$$B_\nu(\nu, T) = \frac{2h\nu^3}{c^2} \frac{1}{e^{h\nu/k_B T} - 1} \quad (1.10)$$

Where B is spectral radiance, ν is photon frequency, T is temperature, h is Planck's constant, and k_B is the Boltzmann constant. The blackbody nature of the CMB implies the plasma was thermalized through constant interactions, namely, Thomson and Rutherford (Coulomb) scattering.

1.2.2 Temperature Anisotropies

One of the reasons Penzias and Wilson were not immediately aware of their discovery is that the CMB is extremely uniform and isotropic. Even though the CMB is a near perfect blackbody, there are small (1 part in 10,000) but significant temperature fluctuations referred to as anisotropies which can be seen in Figure 1.3. These temperature anisotropies (ΔT) can be described in spherical harmonics as:

$$\Delta T(\theta, \phi) = \sum_{\ell=1}^{\infty} \sum_{m=-\ell}^{\ell} a_{\ell m} Y_{\ell m} \quad (1.11)$$

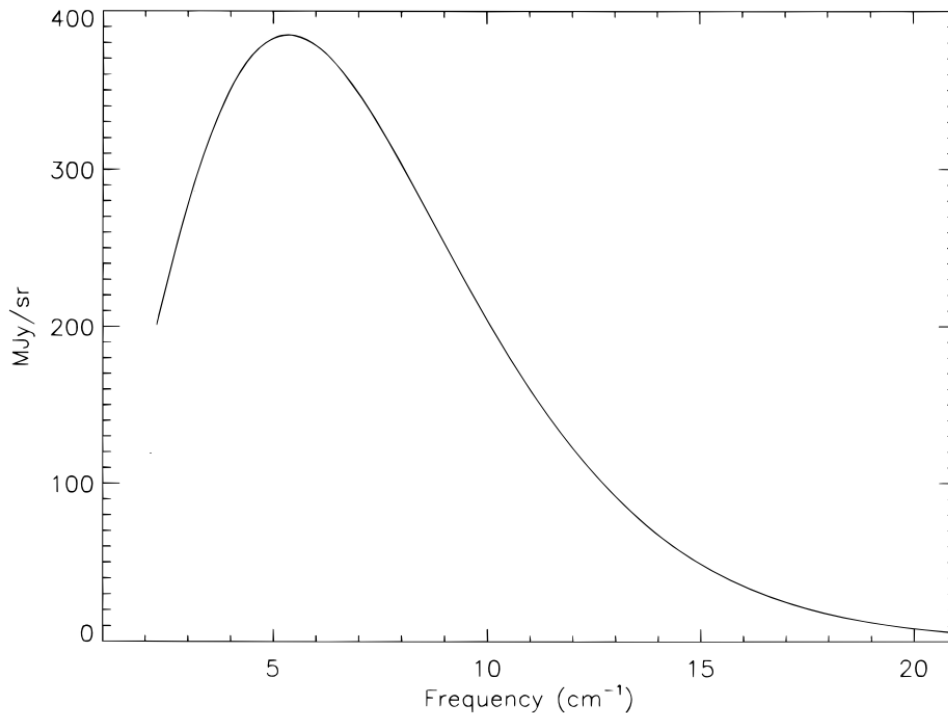


Figure 1.2: FIRAS observation of the CMB blackbody from COBE satellite [10]. The error bars are a fraction of the thickness of the best-fit line

Where θ and ϕ are the angles describing the celestial sphere. The multipole, ℓ , describes the angular scale of the mode and m describes the different number of modes at each scale. Large angular scales correspond with low ℓ and, for intuition's sake, go as roughly $\theta \sim 180^\circ/\ell$.

The information contained in the CMB comes from the statistical distribution of the anisotropies rather than their specific location in the Universe. With the assumption that the anisotropies are drawn from a random Gaussian field, all of the information is contained within the 2-point correlation function. This can be described by an angular power spectrum (APS) which is the variance of the amplitude coefficients:

$$C_\ell \delta_{\ell\ell'} \delta_{mm'} = \langle a_{\ell m} a_{\ell' m'}^* \rangle \quad (1.12)$$

Where the brackets $\langle \rangle$ indicate the average value. However, in practice, there is only one realization of the Universe that we are able to observe. This means the angular power

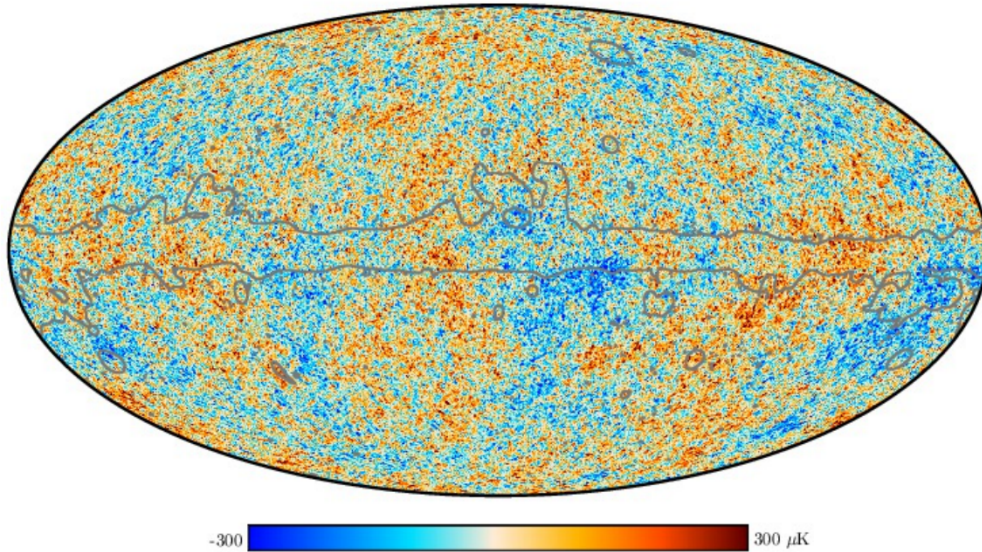


Figure 1.3: Planck Satellite CMB temperature map showing the mean subtracted deviations [11]. A mask was applied to remove the Galactic plan which is indicated by the gray line. Residual foregrounds were also removed from this map.

spectrum is limited to a finite sum over the number of modes at each ℓ :

$$C_{\ell}^{TT} = \frac{1}{2\ell + 1} \sum_{m=-\ell}^{\ell} a_{\ell m}^T a_{\ell m}^{T*} \quad (1.13)$$

The T superscripts indicate that this is an APS of the CMB temperature¹. This will become more relevant when the polarization of the CMB is discussed in the next section (1.2.3). The sample variance is considered an incomplete representation of the true variance because it is limited by the number of modes $(2\ell + 1)$. This variance of the variance is referred to as the cosmic variance and is given by:

$$\frac{\Delta C_{\ell}}{C_{\ell}} = \left(\frac{2}{2\ell + 1} \right)^{\frac{1}{2}} \quad (1.14)$$

The cosmic variance is the theoretical limit to our measurement of the angular power spectrum of the CMB. Because there is inevitably measurement noise, the cosmic variance is most restricting at small ℓ s when it becomes the largest source of uncertainty. Figure 1.4

¹Often the scaled angular power spectrum, $D_{\ell} = \ell(\ell + 1)C_{\ell}/2\pi$ is used.

shows a current measurement of the angular power spectrum of the temperature CMB.

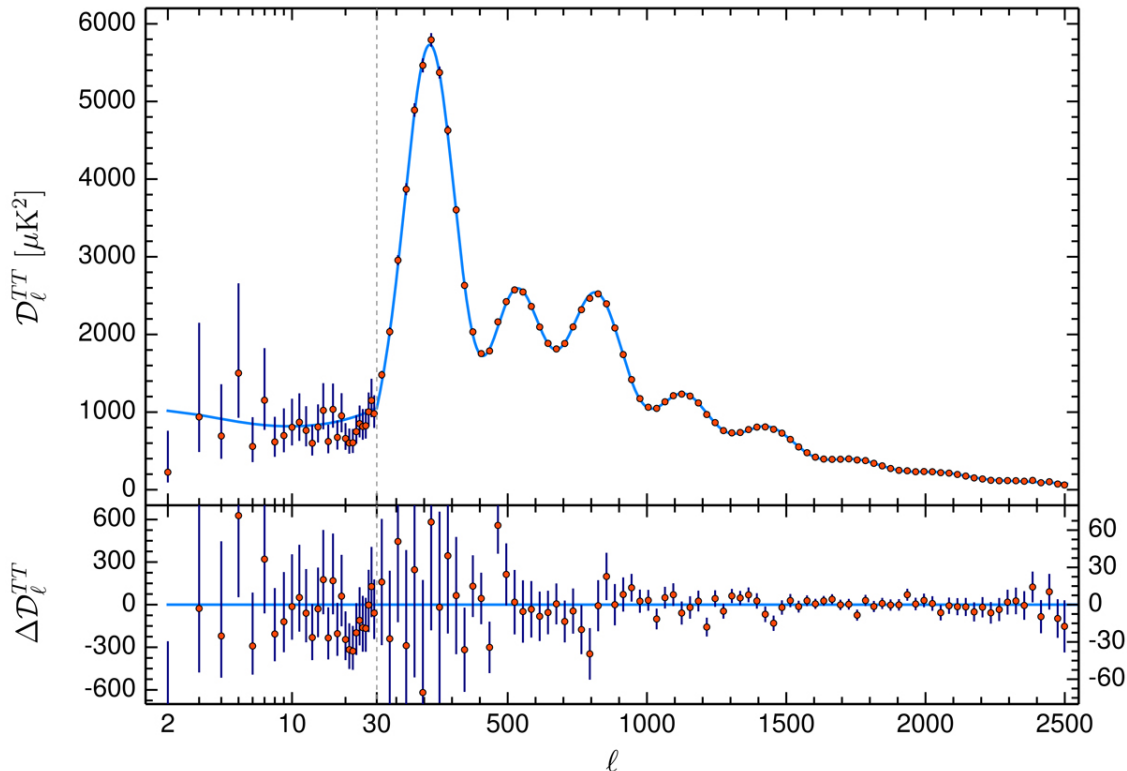


Figure 1.4: The angular power spectrum of the CMB temperature according to the Planck Collaboration [11]. The top panel shows the APS with measured points in red and the best fit ΛCDM model in the blue line. The bottom panel shows the residual between the measured points and the best fit line. Cosmic variance is included in the error bars. Note: the x-axis scale changes at $\ell = 30$ from a log scale to a linear scale.

The angular power spectrum of the temperature CMB is a snapshot of the physics that was happening at the time of last scattering. From Figure 1.3 and Figure 1.4 it is clear there is a structure to these anisotropies. This structure is well described by the ΛCDM model of cosmology and is an imprint from when the Universe was still a plasma. During this time, there were competing forces in over-dense regions with the gravity acting inwardly and radiation pressure acting outwardly. This tension in the primordial fluid caused baryonic acoustic oscillations (BAO) which traveled at relativistic speeds through the tightly coupled baryon-photon plasma.

The compressions and rarefactions from the BAO translate to the peaks and troughs seen in the TT angular power spectrum. Along with the speed of sound in the plasma,

the location of first peak acts as a "standard ruler". The distance this first extrema of the BAO traveled was "frozen" into place during recombination. The location of the first peak is used to constrain the spatial curvature of the Universe. The measurements [12] of the APS are consistent with a flat universe (or at least very close to flat). The relative heights of the second and third peak allow us to constrain the fraction of baryons and dark matter [13]. This is because changing the inertial loading to the BAO changes the relative heights between the odd-numbered peaks (compression) and the even-numbered peaks (rarefaction). For the higher peaks (dampening tail), the scale of the dampening is dependent on the mean free path of the photons at the time of recombination [14]. This provides a consistency check for the baryon density and the age of the Universe at recombination.

1.2.3 Polarization

During the epoch of recombination, photons were constantly Thomson scattering off of electrons. If the incident photons scattered off an electron located in a local temperature quadrupole, it resulted in a net linear polarization. Because only $\sim 10\%$ of the CMB is polarized [15], the resulting signal is quite faint. The polarization field of the CMB was first detected by DASI [16], nearly 40 years after the detection of the temperature of the CMB. Before introducing the mechanisms for creating a local quadrupole in the CMB temperature field, it will be useful to first go over some notation and formalism of polarization used in CMB cosmology.

Stokes Parameters

If we consider the light from the CMB propagating in the \hat{z} direction, then the polarization of the electromagnetic wave is described as:

$$E(x, t) = E_x \cos(\omega t - \theta_x) \quad (1.15)$$

$$E(y, t) = E_y \cos(\omega t - \theta_y) \quad (1.16)$$

Where E is the electric field and the corresponding amplitudes (E_x and E_y), and ω is the frequency. This polarized light is often expressed in Stokes parameters (Equation 1.17). A drawing representing Stokes parameters can be seen in Figure 1.5.

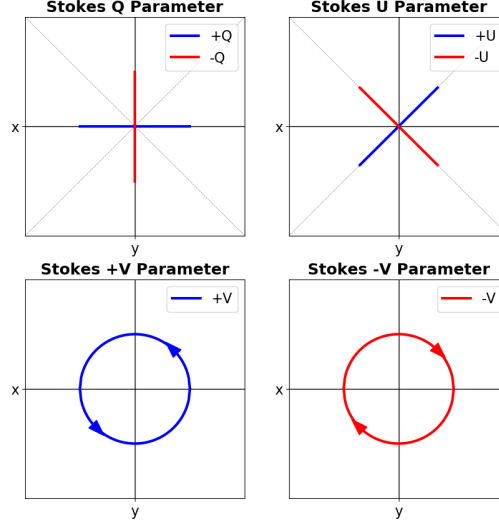


Figure 1.5: Drawings representing Stokes parameters in x-y coordinates. The diagonal dashed gray lines in the Q and U represent a 45° rotation from the x and y axes. The $+V$ parameter is a counter-clockwise rotation and the $-V$ parameter is a clockwise rotation.

With these parameters, $(\hat{\mathbf{x}}, \hat{\mathbf{y}})$ and $(\hat{\mathbf{a}}, \hat{\mathbf{b}})$ are Cartesian bases defined at 45° with respect to each other and $(\hat{\mathbf{R}}, \hat{\mathbf{L}})$ is a circular basis (*right, left*).

$$\begin{aligned}
 I &\equiv |E_x|^2 + |E_y|^2 \\
 Q &\equiv |E_x|^2 - |E_y|^2 \\
 U &\equiv |E_a|^2 - |E_b|^2 = 2\text{Re}(E_x E_y^*) \\
 V &\equiv |E_R|^2 - |E_L|^2 = -2\text{Im}(E_x E_y^*)
 \end{aligned} \tag{1.17}$$

Where I is the intensity, Q and U are linearly polarized light, and V is circularly polarized light. While I and V are invariant under rotations of x and y , Q and U are dependent on the coordinate system. It is worth noting that Thomson scattering can only produce linear polarization and, thus, V can be ignored in the CMB polarization field

E and B Polarization Basis

Similar to the temperature field, the polarization field can be expressed in spherical harmonics. However, in this case, a spin ± 2 weighted harmonic is needed. Equation 1.18 shows the different CMB fields in their corresponding spin-weighted bases.

$$\begin{aligned} T(\hat{\mathbf{n}}) &= \sum_{\ell, m} a_{\ell m}^T {}_0Y_{\ell m}(\hat{\mathbf{n}}) \\ (Q \pm iU)(\hat{\mathbf{n}}) &= \sum_{\ell, m} a_{\ell m}^{(\pm 2)} {}_{\pm 2}Y_{\ell m}(\hat{\mathbf{n}}) \end{aligned} \quad (1.18)$$

The polarization coefficients can be further changed to a basis where they are rotationally invariant (like temperature) [17]:

$$\begin{aligned} a_{\ell m}^E &= -(a_{\ell m}^{(+2)} + a_{\ell m}^{(-2)})/2 \\ a_{\ell m}^B &= i(a_{\ell m}^{(+2)} - a_{\ell m}^{(-2)})/2 \end{aligned} \quad (1.19)$$

Under parity transformation E remains unchanged but B flips signs. In this way, E -mode polarization is analogous to a curl-free electric field and B -mode polarization is analogous to a gradient-free magnetic field. So while the CMB polarization is easiest to observe in the coordinates of Q and U , the E and B basis is preferred because it is independent of coordinate choice.

In the same way the power spectrum for temperature (TT) was constructed (Equation 1.13), a combination of the three CMB fields (T , E , and B) can be taken to form six different spectra:

$$C_{\ell}^{XY} = \frac{1}{2\ell + 1} \sum_{m=-\ell}^{\ell} a_{\ell m}^X a_{\ell m}^{Y*} \quad (1.20)$$

Where X and Y are the possible CMB field types; temperature, E -modes, or B -modes. Figure 1.6 shows the different angular power spectra as measured by the Planck satellite.

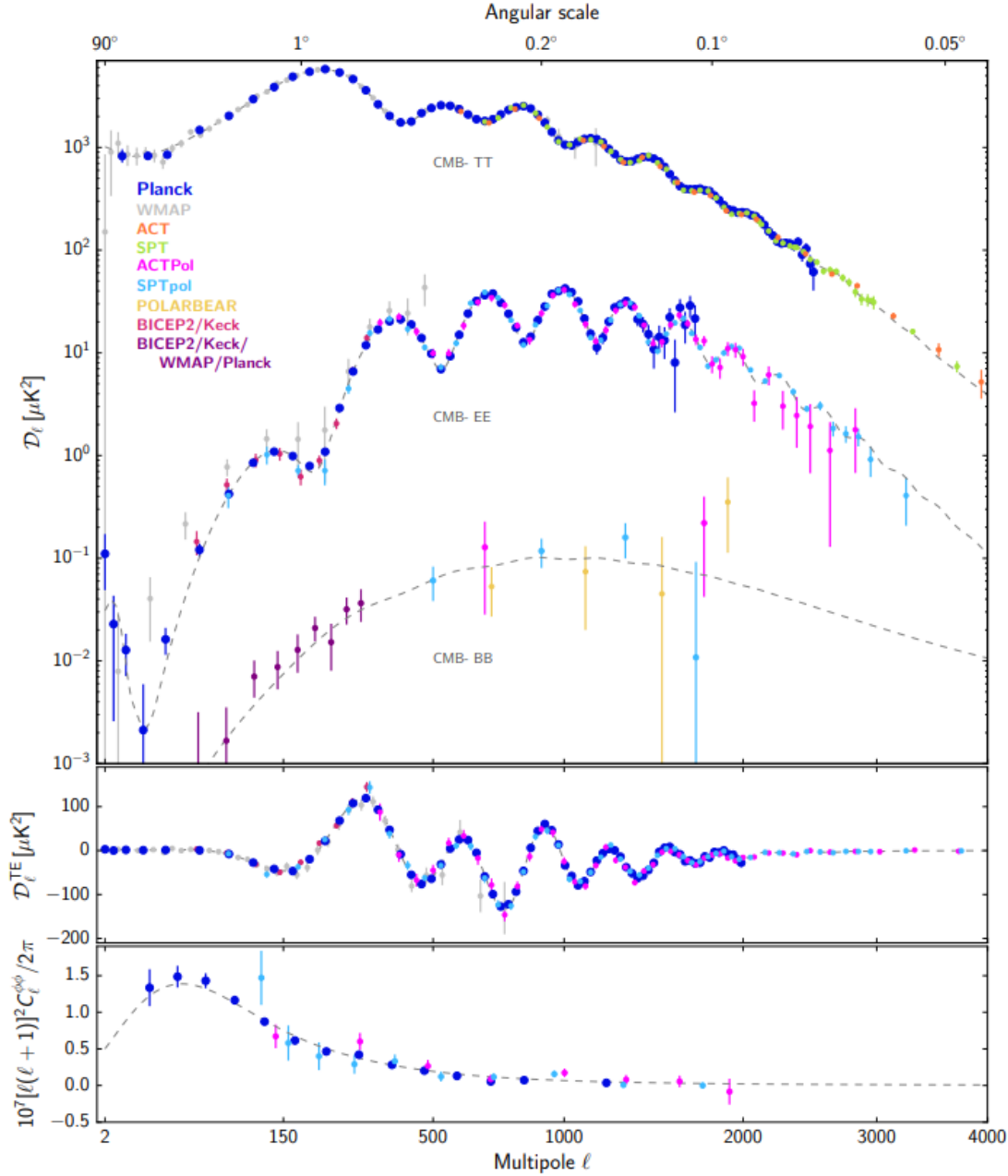


Figure 1.6: The top panel shows the angular power spectra for the CMB including TT , EE , and BB . The middle panel shows the TE cross-spectrum and the bottom panel shows the lensing deflection power spectrum. As can be seen by the various colors, many different experiments were compiled into these spectra. The dashed lines show the best-fit ΛCDM model for the Planck data. Figure from the Planck 2018 results [11]. WMAP data from [18], ACT and ACTpol data from [19] [20] [21]. SPT and SPTpol data from [22] [23] [24] [25]. PolarBear data from [26]. BICEP2/Keck data from [27] [28].

Sources of E-modes and B-modes

Shown in Figure 1.7, the polarization in the CMB arises from incident photons Thomson scattering off of electrons in a local temperature quadrupole. Through the mechanisms that source the quadrupoles, we are able to probe the polarization of the CMB to understand the physics during and before recombination. During recombination, there are two ways to

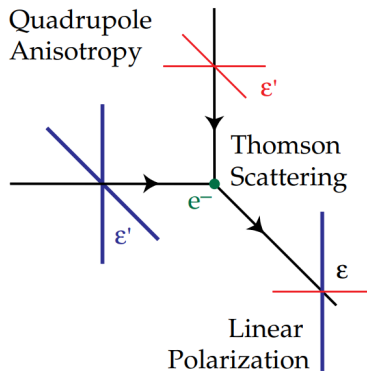
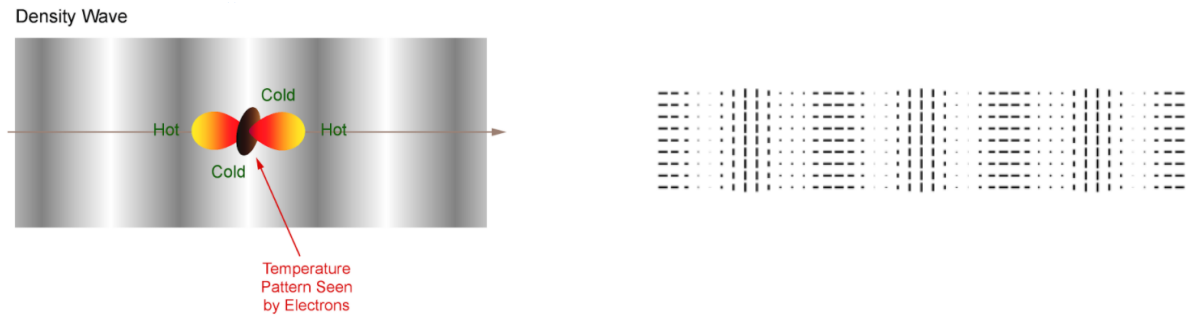


Figure 1.7: Diagram conveying how a local quadrupole anisotropy creates a linearly polarized photon from Thomson Scattering. Figure courtesy of Hu and White [15].

generate a local quadrupole, and thus, ways of forming polarization. The first way is through the BAO generating regions of higher and lower densities in the plasma. In this case, the density waves traveling perpendicular to the surface of last scatter generate polarization seen by the observer. Figure 1.8 shows a simplified visual representation of the mechanism with the resulting polarization. This source of polarization is referred to as a scalar perturbation ($m = 0$) because the polarization pattern is only dependent on the direction the density wave is traveling (one degree of freedom). As seen in Figure 1.8b, the polarization is either parallel or perpendicular to the direction of the density wave is traveling. Figure 1.10a shows how a collection of density waves creates a gradient pattern known as an *E*-mode.

The second source of polarization comes from primordial gravitational waves (PGW). As a PGW passes through the spot occupied by an electron in the plasma, the space-time is distorted elliptically. This distortion causes a redshifting and blueshifting of the photons which is seen by the electron as a temperature quadrupole (Figure 1.9). Because



(a) A cartoon depiction of how an electron experiences a local quadrupole from a density wave.

(b) The resulting polarization pattern from a single density wave. The polarization is either parallel or perpendicular to the wave direction.

Figure 1.8: The polarization caused by density waves, also called a scalar perturbation. Figure courtesy of the BK Collaboration.

of the $m = \pm 2$ nature of the quadrupole created by the PGW, it is referred to as a tensor perturbation. So while the wave can be oriented to give an E -mode, it is also possible for the orientation of the PGW to result in a polarization pattern which is $\pm 45^\circ$ to the direction of wave propagation [29]. Thus, the unique signature of a tensor perturbation is the curl pattern known as a B -mode which can be seen in Figure 1.10b.

So not only does changing to the E/B basis make the polarization field independent of coordinate choice, it also makes it easier to distinguish the source which produced the polarization. In the CMB, the gradient-like E -modes are produced by *both* scalar and tensor perturbations. The curl-like B -modes are only produced by tensor perturbations [30]. For this reason, any detection of B -modes is a powerful tool in understanding the physics of the Universe at the early epochs.

1.3 Inflation

The Λ CDM model of cosmology accurately describes much of the observed phenomena in the Universe. However, there are some notable limitations with this theory; the origin of initial perturbations, the horizon problem, and the flatness problem. Cosmic Inflation, or

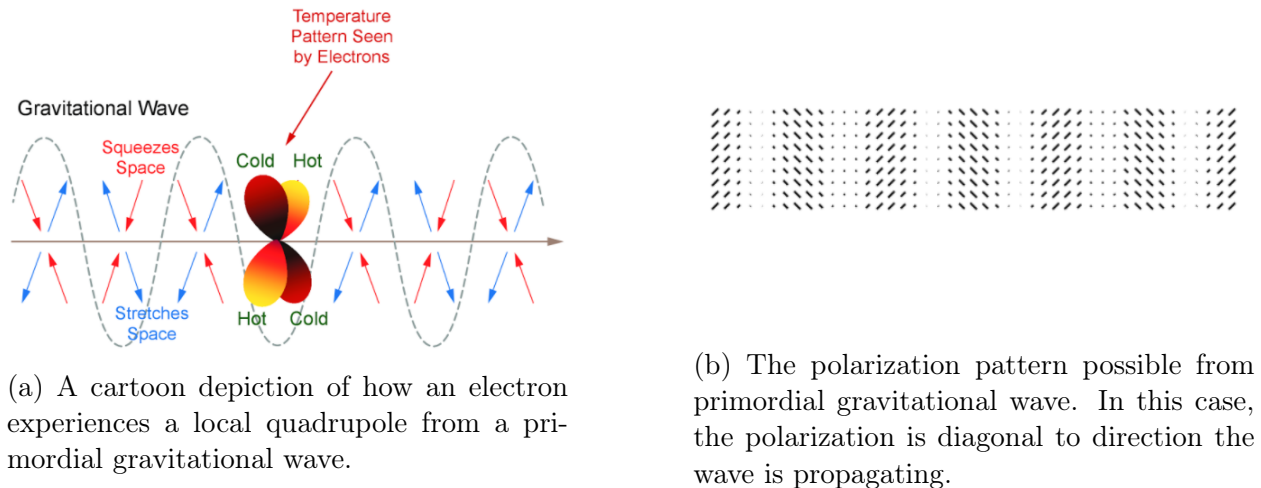
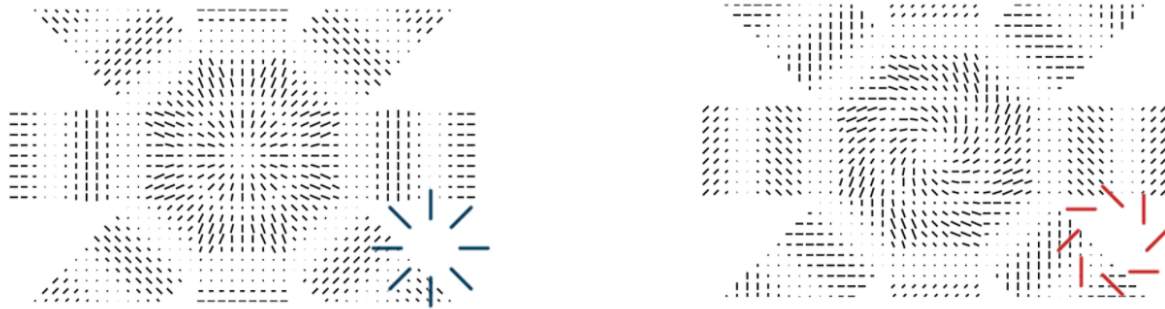


Figure 1.9: The polarization caused by a primordial gravitational wave, also called a tensor perturbation. Figure courtesy of the BK Collaboration.

simply Inflation, is an extension of the Λ CDM paradigm proposed by Alan Guth in 1970s as an explanation [31]. Inflation, in short, is an extremely rapid and accelerated expansion of space-time during the earliest moments of the Universe. Quantum fluctuations were the seeds for the initial perturbations as the Universe expanded by ~ 60 e -folds before the Universe acted according to the standard Big Bang cosmology. In this section, I will discuss perhaps the most prominent but simple model of Inflation, known as single-field slow-roll (SFSR). I will discuss how extending the paradigm to include Inflation address some of the shortcomings of Λ CDM cosmology. I will also discuss how observations provide evidence in support of Inflation and how future observations could provide *unique* evidence.

1.3.1 The Horizon Problem

As noted earlier, the temperature of the CMB is extremely uniform throughout the entire observable Universe; no matter which direction we look. This implies that the observable universe was in thermal equilibrium by the time of recombination. However, according to standard Big Bang cosmology (no inflation), the photons from opposite sides of the surface of last scattering should not be in causal contact. In other words, the predicted particle horizon is sufficiently small ($\theta_{hor} \sim 2^\circ$) compared to what we observe. This is known as the horizon



(a) The E -mode polarization pattern which can be created from a scalar or tensor perturbation.

(b) The B -mode polarization pattern which can only be created from a tensor perturbation.

Figure 1.10: The polarization patterns caused by density waves and PGW. Figure courtesy of the BK Collaboration.

problem.

Inflation offers a solution to this problem by extending the early Universe to include a time of rapid acceleration of the scale factor. So if $\ddot{a} > 0$, this implies that the comoving Hubble radius, $(aH)^{-1}$ must be shrinking. The comoving Hubble radius is a way to describe how far the particle horizon extends, i.e., the maximum distance photons can travel and be causally connected. During the time of inflation, the particles were able to be in causal contact and thermal equilibrium on large angular scales. Figure 1.11 shows a conformal diagram of how adding a period of inflation extends the area of causal contact before recombination by shrinking the comoving Hubble radius.

1.3.2 The Flatness Problem

With current measurements, we observe that the spatial curvature of the Universe is consistent with a flat Universe [11]. In section 1.1 we included a spatial curvature term (Ω_k) in the Friedman equation and discussed the critical density $\rho_c = 3H^2/8\pi G$ for a flat universe. If we look at the first Friedmann equation in terms of the unitless energy density, Ω_0 , then we get the following:

$$1 - \Omega_0 = \frac{-kc^2}{H_0^2 a_0^2} \quad (1.21)$$

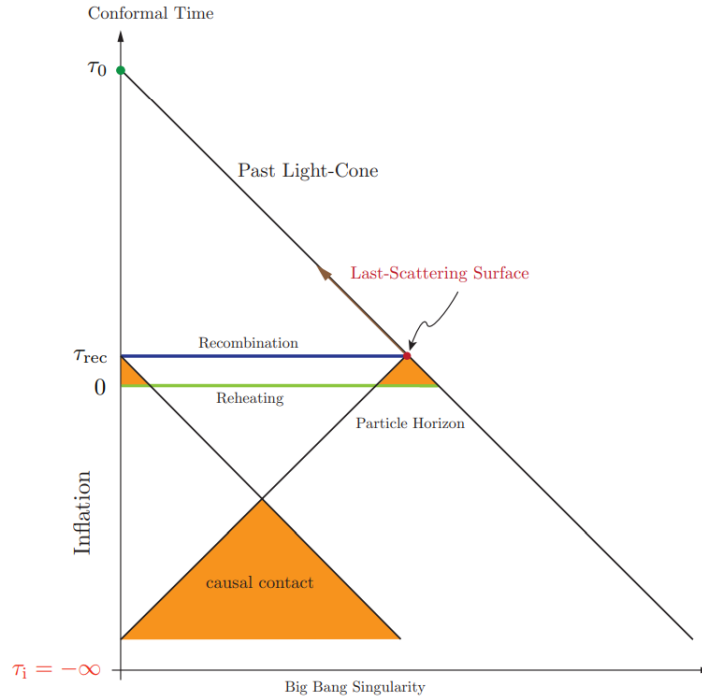


Figure 1.11: A conformal diagram of the time period of inflation leading into the epoch of recombination. The orange shading represents times of causal contact. The green line labeled "reheating" is when inflation ends and is where standard Big Bang cosmology begins. Figure courtesy of Daniel Baumann [32].

A flat universe corresponds to $\Omega_0 = 1$ but it could easily been any other value. The fact that our measurements correspond very precisely with a flat universe at our current time means that the universe would have had to be even flatter at early times. So why do we observe such a ‘special’ value and is it merely a coincidence? This fine-tuning problem is known as the Flatness problem.

Inflation offers a solution by the way of exponential expansion of the scale factor. During the time of inflation, the energy density was dominated by a form of dark energy and the scale factor scales as $a \propto e^{H_0 t}$ with time. So Equation 1.21 would look like $1 - \Omega_0 \propto e^{-2H_0 t}$ and the energy density would be $\Omega \sim 1$. In other words, the observable universe is locally flat because it is on a much smaller scale than the inflated universe.

1.3.3 Single-field Slow-roll Inflation

In the SFSR Inflation paradigm, there is a single scalar field ϕ which is the inflation and a potential which is dependent on this field, $V(\phi)$. During inflation, the Universe is accelerating and thus $\ddot{a} > 0$. From the second Friedmann equation (Equation 1.4), this implies that in the equation of state, $w < -1/3$. In other words, the Universe must be in a regime dominated by some form of dark energy. The density and pressure are then written, respectively, as:

$$\rho = \frac{1}{2}\dot{\phi}^2 + V(\phi) \quad (1.22)$$

$$p = \frac{1}{2}\dot{\phi}^2 - V(\phi) \quad (1.23)$$

Using the the Friedmann equation and the equation of state, an equation of motion for the scalar field can written as:

$$\ddot{\phi} + 3H\dot{\phi} - V'(\phi) = 0 \quad (1.24)$$

Where the prime notation in $V'(\phi)$ indicates a derivative with respect to ϕ . So the equation of motion is just the equation of a simple dampened harmonic oscillator. The dampening term, $3H\dot{\phi}$, is dependant on the Hubble parameter and is referred to as the Hubble friction.

For slow-roll, there are two conditions which must be met in order for there to be inflation. The first condition requires the kinetic energy from the scalar field to be much less than the potential, $\dot{\phi} \ll |V(\phi)|$. Thus the scalar field is "slow rolling" towards the minimum of the potential. The second condition requires that the kinetic scalar term does not grow too fast. So in order for the kinetic term to not overtake the potential term, the acceleration must be much less than the friction term, $|\ddot{\phi}| \ll 3H\dot{\phi}$. These conditions are often defined with the two parameters [33]:

$$\epsilon = 3 \frac{\dot{\phi}^2/2}{V + \dot{\phi}^2/2} \simeq \frac{M_{pl}^2}{2} \left(\frac{V'}{V} \right)^2 \ll 1 \quad (1.25)$$

$$\eta = -2 \frac{\ddot{H}}{H^2} - \frac{\dot{\epsilon}}{2H\epsilon} \simeq \frac{M_{pl}^2}{2} \left(\frac{V''}{V} \right)^2 \ll 1 \quad (1.26)$$

Where M_{pl} is the reduced Planck mass ($M_{pl} = (8\pi G)^{-1/2}$). When these slow-roll conditions are no longer met, inflation ends and reheating or thermalization begins. During this period, the energy density of the inflation field is converted into standard model particles which begins a radiation-dominated regime of the Universe. Figure 1.12 shows an example of what a SFSR inflation model might look like.

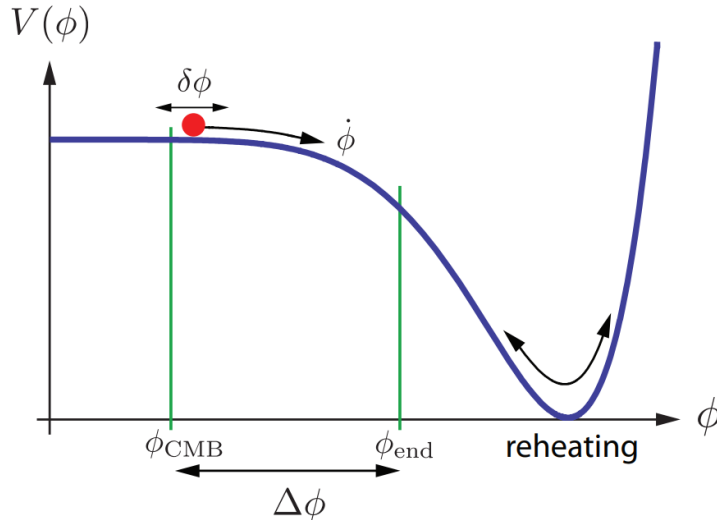


Figure 1.12: A toy representation of what a scalar field and potential would look like for SFSR inflation. Between ϕ_{CMB} and ϕ_{end} , CMB perturbations ($\delta\phi$) are created via quantum fluctuations. At ϕ_{end} , inflation ends and the energy density is converted into radiation. Figure courtesy of Daniel Baumann [32].

1.3.4 Perturbations

Adhering to the Heisenberg Uncertainty principle, quantum fluctuations create virtual particles that immediately annihilate. While the average of these fluctuations is zero, the variance is not. Inflation is such a rapid expansion, that it can act as a mechanism for a virtual particle to become real; similar to the mechanism of Hawking radiation with black holes. Spatially varying quantum fluctuations in the scalar field ($\delta\phi$) induce scalar perturbations in the space-time metric. These perturbations are created on all length scales; where k is the wavenumber of the Fourier modes. During periods of inflation, the wavelength of these modes grow faster

than the comoving Hubble radius and eventually become larger ($k < aH$). These perturbations exit the horizon and are "frozen" into the superhorizon scalar field [34]. Figure 1.13 shows a toy diagram of this process. Eventually, the perturbations will re-enter the horizon and become the density perturbations seen in the CMB. This consequence of Inflation gives an explanation for the origins of the initial perturbations seen in the CMB; something which was lacking in the Λ CDM cosmology paradigm prior to the theory of Inflation.

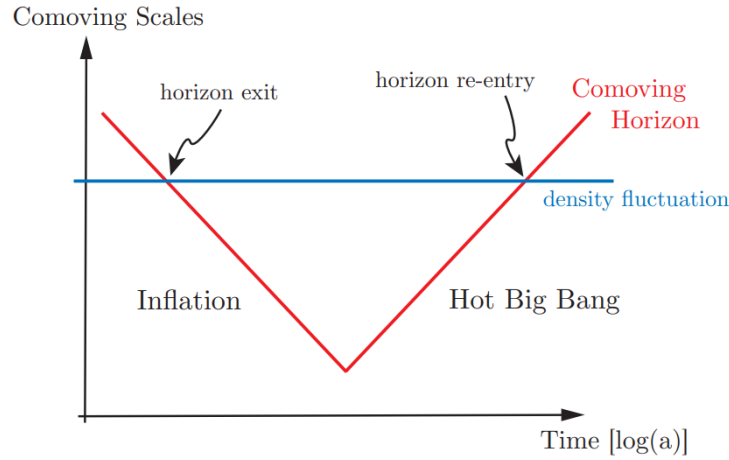


Figure 1.13: The density perturbations (blue) come from quantum fluctuations during the time of inflation when they exit the horizon (red). Upon re-entry, they become the seeds for the structure of the Universe. These density fluctuations can be seen in the CMB as anisotropies. Figure courtesy of Daniel Baumann [32].

In a similar manor to scalar perturbations, gravitational waves (also called tensor perturbations) create perturbations in the transverse and traceless components of the space-time metric. The power spectra of the initial scalar perturbations and tensor perturbations are given as [33]:

$$P_s(k) = \frac{1}{8\pi^2\epsilon} \frac{H^2}{M_{pl}^2} \quad (1.27)$$

$$P_t(k) = \frac{2}{\pi^2} \frac{H^2}{M_{pl}^2} \quad (1.28)$$

Where again, M_{pl} is the reduced Planck mass and ϵ is the slow-roll parameter defined in

Equation 1.25. These spectra are described by their spectral index:

$$n_s(k) - 1 = \frac{d \ln P_s}{d \ln k} \quad (1.29)$$

$$n_t(k) = \frac{d \ln P_t}{d \ln k} \quad (1.30)$$

Where scale-invariant spectra correspond to $n_s = 1$ and $n_t = 0$, respectively. From slow-roll Inflation, it is expected that n_s is very close to but a little less than one [35], $n_s = 1 - 4\epsilon - 2\eta$. In the same way, n_t can be related to the slow-roll parameters as $n_t = -2\epsilon$.

The amplitude of PGW are most often parameterized as a tensor-to-scalar ratio r which is defined as:

$$r = \frac{P_t(k)}{P_s(k)} \quad (1.31)$$

A detection of r would provide a measurement of PGW from the early Universe during inflation. This detection would give unique “smoking-gun” evidence in favor of Inflation. Discussed in Section 1.2.3, tensor perturbations result in *both* B -mode and E -mode polarization of the CMB while scalar perturbations result in *only* E -mode polarization. Because of this, a detection of primordial B -modes in the CMB means a detection of tensor perturbations and, thus, a detection of r .

A measurement of the amplitude of r would also provide information about the energy scale of Inflation. Particularly, a value of r large enough to be measured suggests that we are probing physics at the GUT (Grand Unified Theory) scale [36]. While SFSR Inflation is the most prevalent model of Inflation, there are choices in the model and even different Inflation models which predict different levels of observables. Figure 1.14 shows some of the more common models for Inflation and their current constraints.

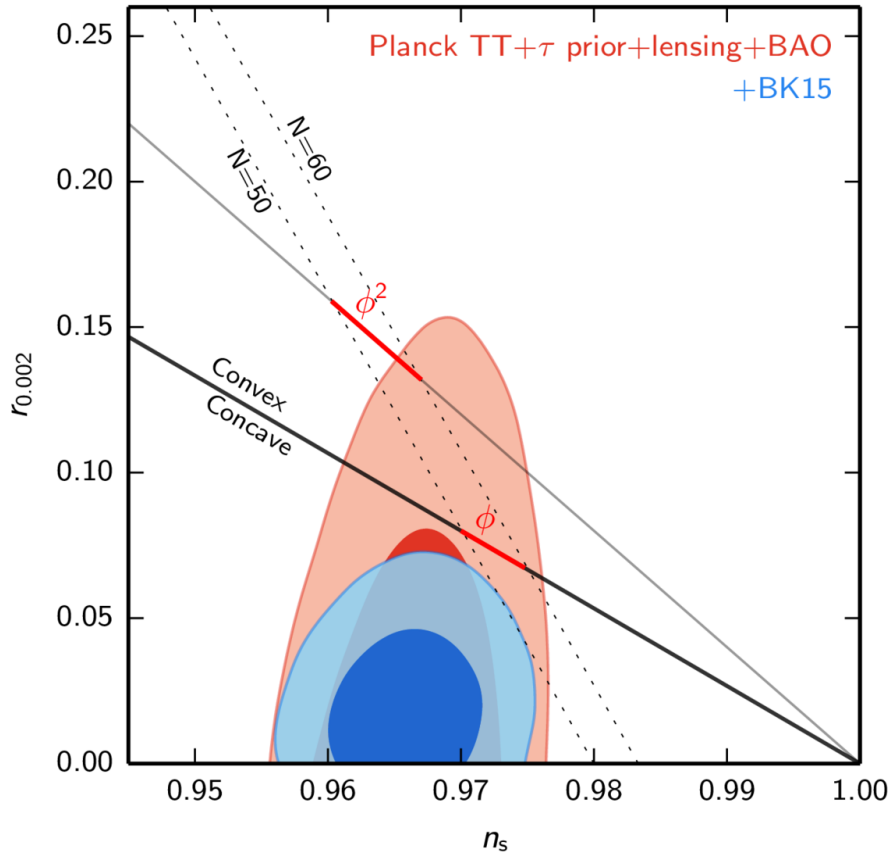


Figure 1.14: The current constraints on r and the spectral index (sometimes called spectral tilt) of scalar perturbations. The red contour shows the constraints from Planck and BAO and the blue contour adds in the BICEP/Keck data. The darker contour is 1σ and the lighter contour is 2σ . The constraint on n_s comes mostly from temperature power spectra and a little from E -mode power spectra. The constraints on r is driven mostly from B -mode power spectra. Different models of e -folding (N) and scalar inflation fields are shown. Figure courtesy of the BK Collaboration [37].

1.4 Foregrounds

The signal from the CMB is from the earliest light of the Universe. Consequently, when measuring the CMB, any astrophysical signal or distortion between the CMB and observer is considered a nuisance signal, otherwise known as a foreground. The three most relative foregrounds in measuring the CMB polarization field are: polarized galactic dust, synchrotron radiation, and gravitational weak lensing. Polarized galactic dust (or simply dust) and synchrotron radiation (or simply sync) are polarized microwave emissions in our own Milky Way

Galaxy. These two sources dilute the primordial B -mode signal used to detect PGW. Fortunately, dust and synchrotron scale differently in frequency when compared to the CMB. This means that with a multi-band observation it is possible to disentangle r from the galactic foreground measurements. The other foreground, gravitational lensing, is a distortion of the primordial E -modes by the gravitational fields of the matter between CMB and observer. It is another source of B -modes but it requires a more subtle approach in distinguishing between signals. Disentangling the foreground signals from primordial B -modes is crucial in constraining r .

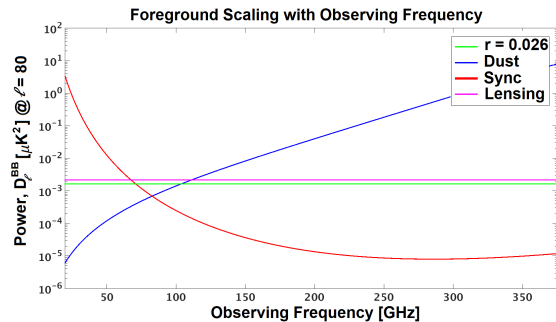
1.4.1 Dust

Galactic dust at a temperature of $T_d \sim 20K$ gives off a polarized thermal emission that overlaps with the polarization spectrum of the CMB. The physics of galactic dust emitting polarized radiation is complicated [38]. However, for the scope of this work, the grains of dust in the interstellar medium can be simplified to an elongated elliptical shape. These dust grains tend to align their major axis with the galactic magnetic field and polarized radiation is more efficiently emitted along their minor axis.

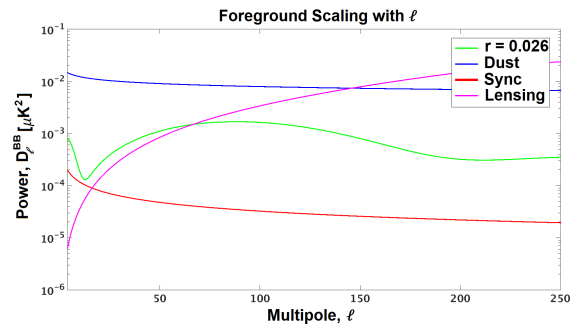
The level of dust in the sky varies from patch-to-patch and is most prevalent in the galactic plane. In terms of relevant CMB frequency, dust dominates at higher frequencies but drops off at lower frequencies. Dust is modeled using a modified blackbody spectrum (graybody) [39] as $I_d(\nu) \propto \nu^{\beta_d} B_\nu(T_d)$. Figure 1.15a shows how dust scales differently than the CMB, i.e., larger at higher frequencies. The difference in spectra makes it possible to disentangle the signals by a multi-band measurement.

1.4.2 Synchrotron

Cosmic-ray electrons in the magnetic field of our Galaxy emit polarized synchrotron radiation which is another source of galactic foregrounds. The particle distribution for these electrons with number density n_e and energies E is expressed as a power law $n_e \propto E^{-p}$ where p is the



(a) Foreground scaling with frequency. Synchrotron dominates at lower frequencies and dust dominates at higher frequencies. Lensing scales the same as r because they are both sourced by the CMB.



(b) Foreground scaling with ℓ . r peaks at $\ell \sim 80$ while the lensing amplitude scales larger at higher ℓ .

Figure 1.15: BB angular power spectra generated from the BK collaboration multi-component model. These plots demonstrate how r and foreground scale in terms of (a) frequency and (b) ℓ . In both cases, a level of $r = 0.026$ is shown for reference.

index [40]. The intensity of the synchrotron radiation is dependent on the number density of the cosmic-ray electrons, n_e , and the magnetic field perpendicular to the line of sight. This allows us to write the intensity of synchrotron radiation as a simple power law in terms of frequency [41]:

$$I_s(\nu) \propto \nu^{\beta_s} \quad (1.32)$$

Where β_s is the spectral index of polarized synchrotron. The frequency scaling can also be seen in Figure 1.15a where synchrotron is most present at lower frequencies. Much like dust, there is variation of the spectral index depending on galactic location. However, on average, synchrotron has a spectral index of $\beta_s \approx -3$ [42].

1.4.3 Gravitational Lensing

As the photons of the CMB traverse through the large scale structure of the Universe, they are deflected and distorted by the gravitational fields of matter. This results in weak gravitational lensing of the CMB temperature and polarization anisotropies. While the polarization direction and intensity remain the same, the position of the anisotropies are

translated [43]. The remapping of the temperature field $T(\hat{\mathbf{n}})$ and the polarization fields $Q(\hat{\mathbf{n}})$ and $U(\hat{\mathbf{n}})$ can be expressed as [44]:

$$T(\hat{\mathbf{n}}) = \tilde{T}(\hat{\mathbf{n}} + \nabla\phi) \quad (1.33)$$

$$(Q \pm iU)(\hat{\mathbf{n}}) = (\tilde{Q} \pm i\tilde{U})(\hat{\mathbf{n}} + \nabla\phi) \quad (1.34)$$

Where ϕ is the line-of-sight gravitational potential, $\hat{\mathbf{n}}$ is the direction of the sky, and the tilde represents the unlensed field. An exaggerated example of this can be seen in Figure 1.16.

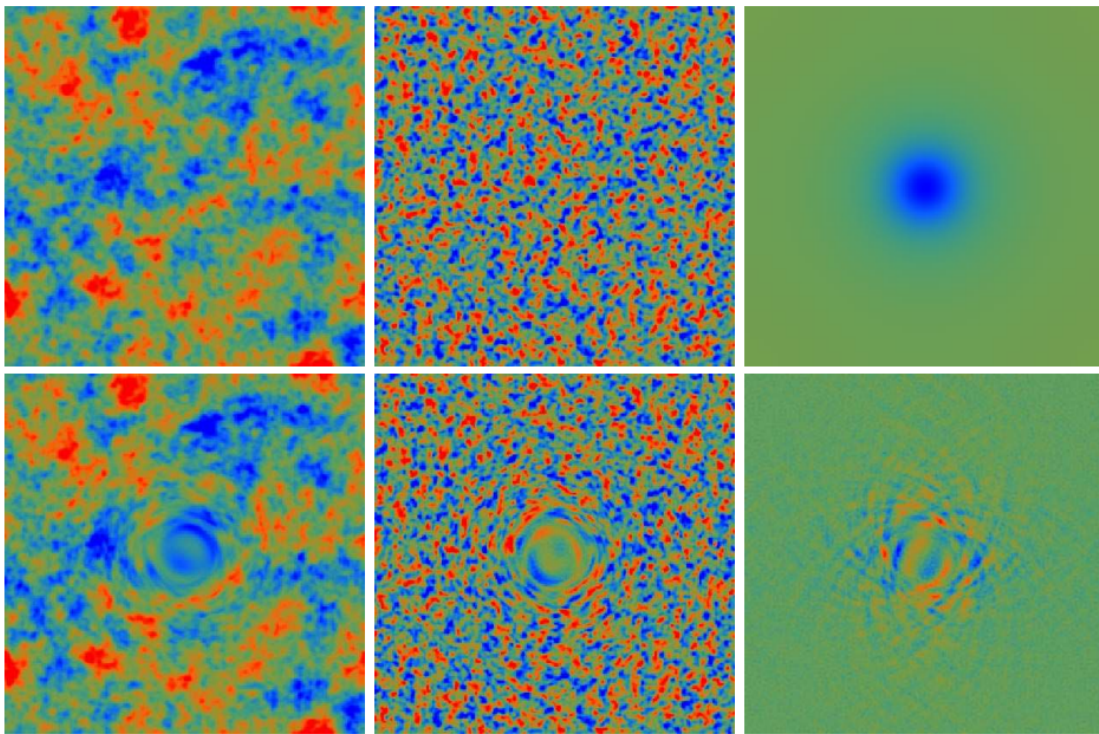


Figure 1.16: An exaggerated example of gravitational lensing acting on a 10 square degree patch of the CMB. The top left panel shows an unlensed temperature field and the top middle panel shows an unlensed E -mode polarization field. The top right shows a gravitational lensing source ϕ . The bottom panels show the effect of the source acting on the temperature field (left), the E -mode polarization field (middle), and lastly, the resulting B -mode polarization field from the lensed E -modes. Figure courtesy of Wayne Hu and Takemi Okamoto [44].

In short, the gravitational lensing creates B -modes by distorting primordial CMB E -

modes. Unlike the galactic foregrounds, gravitationally-lensed B -modes are sourced by the CMB and, therefore, have the same frequency scaling as the primordial B -modes (r), also from the CMB. As seen in Figure 1.15b, the lensed BB spectra peaks at higher ℓ than r because it follows the ℓ scaling of the unlensed EE spectra. While the galactic foregrounds can be disentangled from r by a multi-band measurement, lensed B -modes need to be treated differently. In order to improve r measurements, a process known as delensing is used. This process involves making a lensing template of the gravitational potential field and reversing the deflection [45].

Chapter 2

BICEP/Keck Experiment

The BICEP/Keck (BK) Collaboration operates a dedicated experiment to detect a signal from PGWs by measuring and constraining the tensor-to-scalar ratio, r , described in the previous chapter. The small aperture refracting telescopes are optimized to observe the polarization of the CMB at degree angular scales ($\ell \sim 80$) where the signal of PGWs is expected to be largest. A relatively small patch of sky (~ 500 sq. deg.) is continuously observed from the Amundsen-Scott South Pole Station. The modular design of the receivers allows for multi-frequency observation as well as regular upgrades.

2.1 Program History

The experiment started with BICEP1, which observed from 2006 through 2008. However, the current collaboration started with the next iteration of the experiment, BICEP2 (B2), which observed from 2010 through 2012. Keck Array, or simply Keck, was deployed in addition to the B2 receiver in 2011. The Keck Array telescope was composed of 5 receivers (Rx)¹ modeled after B2, which allows for multi-frequency observation while minimizing systematic uncertainties. BICEP3 (B3) replaced BICEP2 in 2015 with a factor of $\sim 5\times$ more detectors

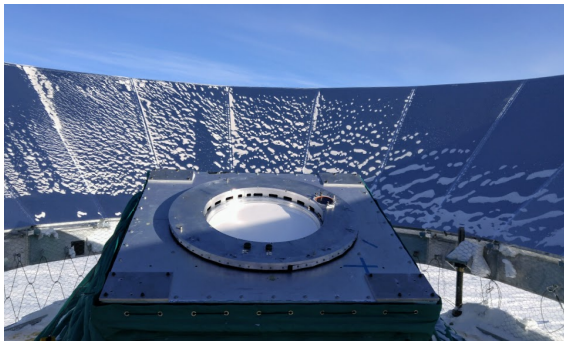
¹‘Receiver’ is often shorted to ‘Rx’ and used as a designation for receiver in an experiment, e.g. rx0 or rx1

and is still operating. In 2019 Keck was replaced with BICEP Array (BA) which allowed for use of upgraded B3 style receivers and detectors. Table 2.1 gives an overview of the program history.

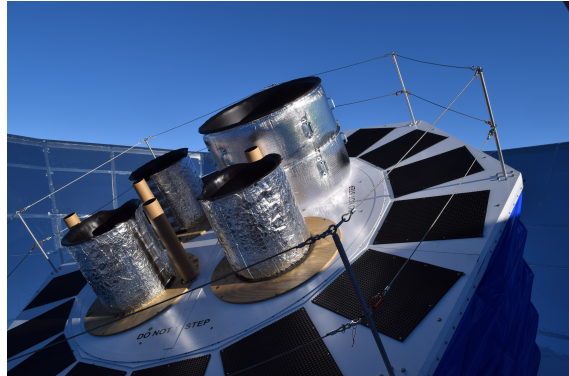
Receiver (# of receivers) Observing Band [GHz]	Years of Operation	Number of Detectors / Rx
BICEP2 (1) 150	2010 - 2012	500
Keck Array (5) 95 150 220 270	2011 - 2019	288 512 512 512
BICEP3 (1) 95	2015 - current	2560
BICEP Array (4) 30/40 95 150 220/270	2020 - current {2022} {2022} {2023}	192/300 {4056} {8664} {8112/13068}

Table 2.1: The BK Collaboration receiver history. Any dates and numbers in curly brackets are projected. While BICEP Array is waiting for additional receivers, Keck Array 220GHz and 270GHz receivers are placed in the empty slots. It should also be noted that several of the Keck Array receivers were changed throughout the operation of the experiment. However, for simplicity's sake, this is not shown.

Because BICEP Array receivers are being installed over several years, the empty slots available in the mount are filled with Keck receivers. The general strategy for each iteration of the instrument has been to upgrade receivers with a factor of $\sim 5\times$ more detectors and then expanding that to an array with multiple observing frequencies. The remaining discussion in this chapter will focus on the BICEP Array receiver. It is the newest iteration of the receivers and while there are slight differences between the different generations, they all operate with the same basic design. Figure 2.1 shows a picture of BICEP Array and BICEP3, the current telescopes being operated by the BK Collaboration.



(a) BICEP3 viewed from the roof. The fore-baffle was removed for summer calibrations.



(b) BICEP Array viewed from the roof. Figure courtesy of Mike Crumrine and the BK Collaboration.

Figure 2.1: On the left is BICEP3 viewed from the roof. The silver panels in a cone surrounding the receiver make up the ground shield. On the right is BICEP Array. Notice how the larger BA receiver on the top and the three smaller Keck receivers which surround it.

2.2 Observing

2.2.1 Site

The Amundsen-Scott South Pole Station is located at the geographical south pole and is logistically operated and funded by the United States Antarctic Program. From travel, to shipment, to living quarters, to power generation this provided infrastructure makes the operation of the BICEP/Keck experiments significantly easier. In addition to the built-in support, the extremely dry and atmospherically stable conditions at the South Pole are among the best on the planet [46] for observing the CMB. Within the Amundsen-Scott compound, the BK Collaboration operates the BICEP3 and the BICEP Array experiments in the Dark Sector, a designated area where radio communication is minimized in order to avoid excess signal picked up by our detectors. Figure 2.2 shows the two buildings that house BICEP3 and BICEP Array.

The main source of atmospheric interference in the microwave spectrum comes from the oxygen and water absorption lines. Thus, less atmosphere and less water vapor means better transmission. The Amundsen-Scott South Pole Station is on the Antarctic Plateau with an

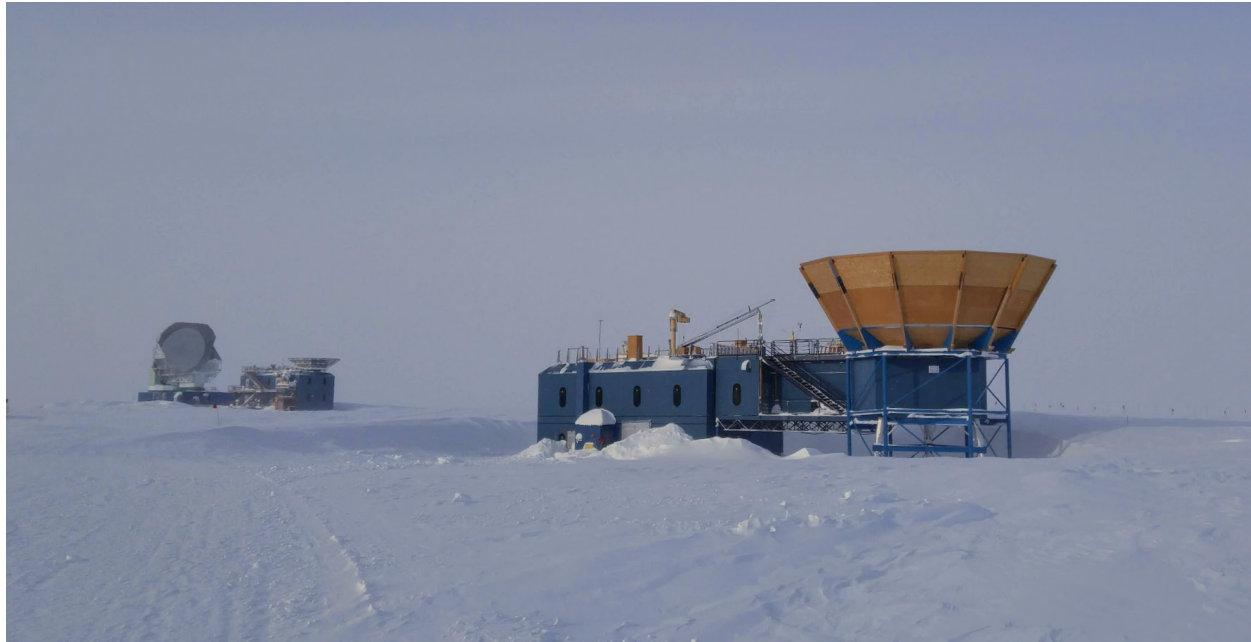


Figure 2.2: On the building on left is the Dark Sector Laboratory (DSL) where BICEP3 is located. Also located in DSL is South Pole Telescope which is not part of the BK Collaboration but does similar types of observations. The building on the right is the Martin A. Pomerantz Observatory (MAPO) which is where Keck Array previously operated but where BA currently operates.

elevation of $\sim 2800\text{m}$ above sea level which means there is less atmosphere to look through. With temperatures never reaching above 0°C , the year round extreme cold means there is reduced water vapor and minimal precipitation.

In addition to the high and dry atmosphere, there are several other advantages of being located at the geographic pole. The fact that the observation site is located on the axis of rotation of the Earth means the same sky is visible year round. This is conducive to our observation strategy (discussed in the next section) which involves observing the same patch of sky continuously. The day-night cycle of the South Pole is such that there is only one night and one day per year. This reduces time and spatial variation of the water vapor in the atmosphere, such as clouds.

2.2.2 Strategy

As mentioned previously, the general strategy is to continuously observe the same patch of sky with all of our receivers. Figure 2.3 shows the patch of sky centered at $RA = 0hr$, $dec = -57.5^\circ$ which we observe the CMB (also shown is a Galactic field). This patch is about $\sim 1\%$ of the sky ($\sim 500 \text{ degree}^2$) and was chosen for its low amounts of polarized galactic dust and synchrotron radiation [47]. It is often referred to as the ‘Southern Hole’.

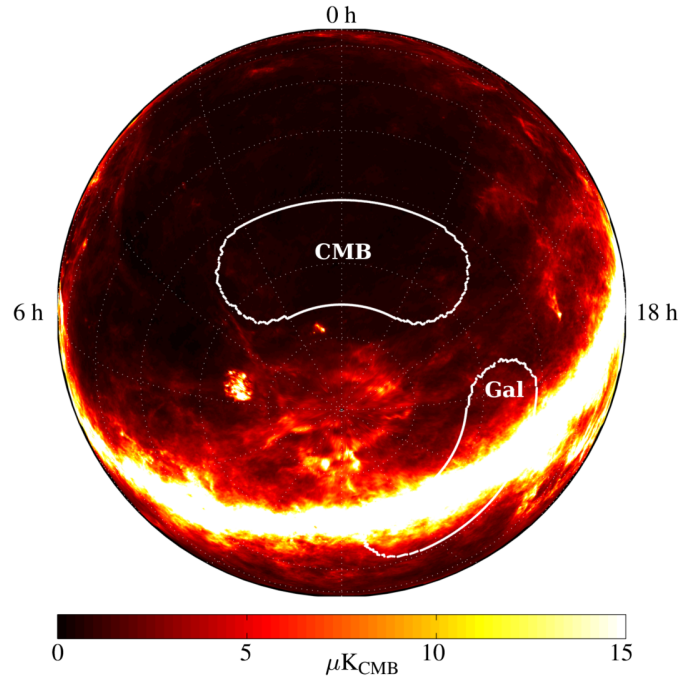


Figure 2.3: The Keck observing field referenced to the polarization amplitude predicted by Planck. This patch of the sky with low polarization foreground amplitude is often referred to as the ‘Southern Hole’. The patch labeled ‘CMB’ is used for CMB while the ‘gal’ patch is centered on the Galactic plane and can be used for Galactic science. This Galactic field is centered at $RA = 15 : 42hr$, $dec = -55.0^\circ$. Figure courtesy of the BK Collaboration [48].

Our telescopes use a horizontal (az-el) coordinate system for observation. Generally, we scan in azimuth for $\sim 50\text{min}$, step in elevation, and then repeat the scan in azimuth. Between schedules, there is a boresight rotation which is referred to as a deck (dk) rotation, not to be confused with declination (dec). Our observation schedule can be broken up into several different timescales and patterns described in detail below:

- **Elnod:** Elevation nod. The telescope moves 1.28° peak-to-peak in elevation about the

central elevation of the scanset. Complementary elnods are performed at the beginning (leading) and end (trailing) of a scanset. This technique is used for a relative gain calibration since the atmosphere is unpolarized.

- **Halfscan:** The telescope moves 64.4° in azimuth at a fixed elevation. The scan velocity is constant ($2.8^\circ/s$) except for the acceleration at the beginning and end of the halfscan, referred to as the turnaround. The halfscan is the smallest telescope movement which makes up a CMB observation.
- **Fullscan:** The telescope makes a halfscan in one direction, stops, and then makes a halfscan back to the starting azimuth location.
- **Scanset:** A scanset is made up of ~ 50 fullscans at roughly 1min/fullscan. Each scanset is sandwiched by a leading elnod at the beginning and a trailing elnod at the end. The entire scanset is at a fixed elevation. We also do detector calibration at the start and end of each scanset known as a partial load curve (PLC)².
- **Phase:** A phase consists of 7-10 scansets. Between scansets, the azimuth is updated to account for the rotating sky and there is a step in elevation. The Phases are labeled *A* through *F* and are described below.
- **Schedule:** A CMB schedule consists of five phases (*B* through *F*) at a constant dk angle. Between each schedule, there is a rotation in dk angle to one of eight positions. Each of the positions are spaced 45° apart and are used to observe the polarization.

The phases are broken up by the sidereal day (over two days) as a 6hr block followed by two 9hr blocks ($\times 2$ days). The first day begins with Phase *A* (6hr block) and is known as a fridge cycle where our sub-Kelvin sorption fridge is recycled. We then do two 10-scanset phases (*B* and *C*) of the CMB which fill the two 9hr blocks. The second day begins with

²A PLC is a voltage sweep of the detector bias. We start from a high bias and then sweep to the target bias. In this way, we are able to get an IV curve of the detector.

Phase *D* (6hrs) which is a 7-scanset phase used to observe the Galactic plane. Finally, Phase *E* and *F* are 10-scanset phases (9hr blocks) for observing our CMB patch. Figure 2.4 shows an example of the mount movement during a scanset.

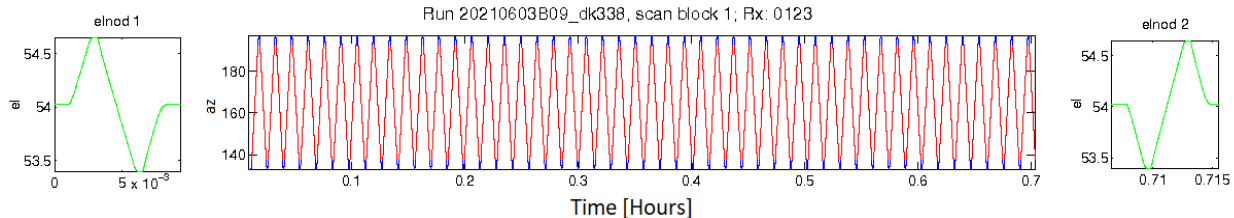


Figure 2.4: Motion of the telescope during one scanset. The x-axis is time in hours and a scanset takes ~ 45 min. The far left and far right plots in green are the leading (left) and trailing (right) elnods performed at the beginning and end of each scanset (the y-axis is elevation in these two plots). The center plot shows the azimuth motion of the telescope during one scanset (the y-axis is azimuth). The red lines indicate the scanning motion when the telescope is slewing with a constant velocity in azimuth ($2.8^\circ/\text{s}$). This period of constant velocity is what we use for our scanset data. The blue line indicates the the motion of the telescope during the azimuth turnaround, i.e., accelerating azimuth motion. The periods of turnaround are not used in the scanset data.

2.3 Receiver Design

2.3.1 Cryostat

The compact refracting telescope design of BA allows all of the optics to be contained within a cryostat [50]. The cryostat, which is under vacuum, houses various nested stages which get colder and colder until reaching the focal plane. In order to detect the faint signals of the CMB polarization, we operate the focal plane of the receivers at $\sim 250\text{mK}$. Each stage of the cryostat is designed to be thermally isolated with radiative shielding in between, reducing the radiative load reaching the detectors. The stages are mechanically supported by low thermal conductivity materials. Figure 2.5 shows a cross sectional view of a BA cryostat which gives a good idea of the general design. The stages from warmest to coldest are labeled as:

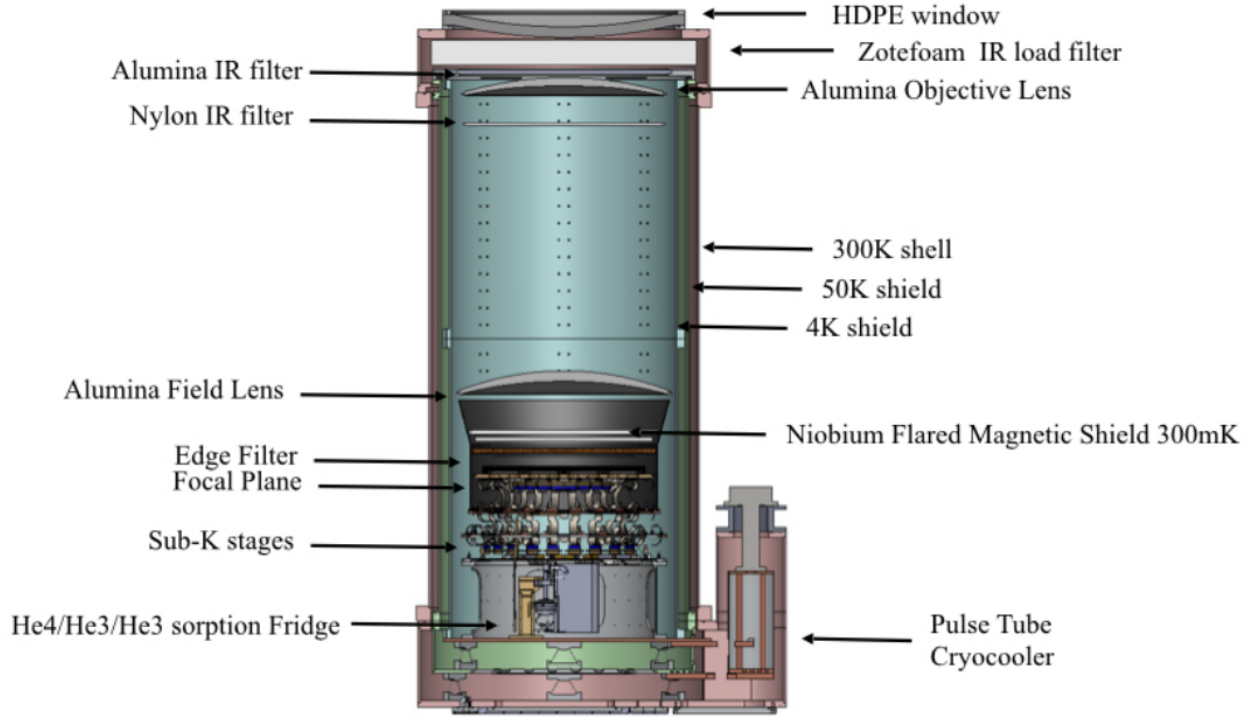


Figure 2.5: Cross section view of BICEP Array cryostat. Figure courtesy of the BK Collaboration [49].

1. **300K Vacuum Jacket** – The outer most shell which is in thermal contact with room temperatures.
2. **50K** – the first cold stage. Cooled by the Pulse Tube Cryocooler.
3. **4K** – the second cold stage. Cooled by the Pulse Tube Cryocooler.
4. **Sub Kelvin (Sub-K)** – the final cold stage which houses the focal plane. Cooled by a 3-stage sorption fridge. This is separated into three more thermal stages: 2K (He4 stage), 340mK (intermediate cold or IC), and 250mK (ultra-cold or UC).

The Pulse Tube Cryocooler is a closed loop helium cooler produced by Cryomech³. It provides the cooling power for the 4K and 50K stages. Prior to Keck, the receivers were cooled with liquid helium and would require frequent refilling.

³<https://www.cryomech.com>

A three stage sorption fridge [51], which is heat sunk to the 4K stage, provides the cooling power for the Sub-K stage. The fridge uses one He4 stage followed by two He3 stages and is controlled via heat switches. The Sub-K insert, sometimes referred to as the ‘wedding cake’ for its shape, mechanically supports the focal plane and is thermally connected to the fridge via heat straps [49]. Between the focal plane and heat straps, a stainless steel block acts as a passive low-pass thermal filter. There is also active temperature control on either side of the thermal block in order to maintain thermal stability of the focal plane. This active temperature control is done via thermistors and resistance heaters in a PID-controller. The thermistors and heaters are controlled by the Housekeeping subsystem which is the topic of the next chapter (Chapter 3).

2.3.2 Detectors

The BA detectors are arrays of perpendicular slot antennas connected to bolometers with Transition Edge Sensors (TES). The detectors work by reading out the temperature change of the bolometer via a change in resistance of the TES caused by optical loading of CMB photons. The bolometer consists of an absorber (the antennas) attached to a TES bolometer island at temperature, T_b , and heat capacity, C . The island is thermally linked (described by the thermal conductance, G) to a thermal bath with temperature, T_s . A conceptual drawing can be seen in Figure 2.6 which depicts the bolometer. There are three main sources of heat transfer on the TES [52]. (1) Optical power (P_R) from the incident photons on the absorber heats the TES bolometer. In the case of observing the CMB blackbody, the power of the photons is proportional to the temperature on the sky and can be approximated as linear because the anisotropies are small, $P_R \propto \delta T_{CMB}$. (2) Joule heating on the TES from a constant voltage bias also heats the island as $P_J \propto V^2/R$. (3) Lastly, the island is cooled via the thermal link to the heat bath as $P_B \propto G(T_b - T_s)$ for small signals about T_b . So while the P_R and P_J increase the temperature of the island, P_B will cool the bolometer and cancel

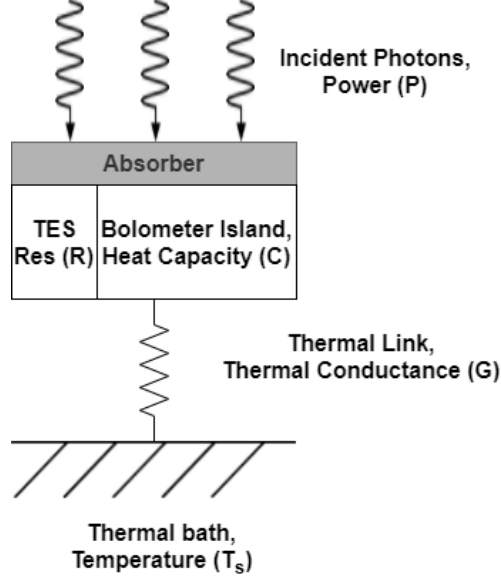


Figure 2.6: Conceptual drawing of a bolometer.

the loading power (assuming equilibrium). The thermal differential equation will look like:

$$C \frac{dT_b}{dt} = P_R + P_J - P_B \quad (2.1)$$

Where C is the heat capacity and T_b is the temperature of the TES bolometer island.

Because the TES is essentially reading out a temperature of the bolometer, the thermal design of the detector needs to be properly tuned in order to give an accurate measurement [53]. The time constant of the bolometer is given by, $\tau = C/G$, where G is the thermal conductance of the thermal link and C is the thermal capacitance of the island. If τ is too small, the sensitivity of the detector is decreased because extra power caused by optical loading will quickly be removed via the thermal bath. If τ is too large, the heat load on the island from the optical power is too great and will drive the detector off transition.

The TES is voltage biased in order to be held at temperature T_c which is on the superconducting transition, where the resistance steeply drops to zero. In addition to the sensitivity achieved with the steep IV transition curve of the TES, the joule heating of the TES bias provides a passive feedback loop. As the temperature (resistance) of the TES increases away

from T_c , the joule heating decreases which brings the temperature back to T_c . This built-in passive feedback loop helps to stabilize the temperature of the detectors and keep them on the sensitive transition curve. Each detector has both an aluminum and titanium TES in series [54]. The aluminium TES has a higher temperature transition ($T_c \sim 1.2K$) and is used for high optical loading environments in the lab or during calibration. A titanium TES with a lower temperature transition ($T_c \sim 0.5K$) is used for CMB observations which provides more sensitivity than the aluminium TES.

2.3.3 Readout

The TES are held at a fixed voltage bias, thus, the bias current changes in response to a change in optical power. The current from the TES is inductively coupled to a Superconducting Quantum Interference Device (SQUID) [55]. The SQUIDs provide a high impedance buffer for each TES while still maintaining sensitivity. Several stages of SQUIDs amplify the signal from the TESs and are read out by warm electronics in arbitrary feedback units (FBU). The TESs use a time-domain multiplexing (TMUX) architecture with a readout and biasing system designed by the University of British Columbia called the Multi-Channel Electronics (MCE) [56]. While the SQUIDs and detectors are all cryogenically cooled, the MCEs are at room temperature outside of the cryostat.

With the TMUX, each TES detector is inductively coupled to a first-stage SQUID (SQ1). A group of SQ1s are coupled to one second-stage SQUID (SQ2) through a summing coil. The SQ2 is referred to as a TMUX ‘column’. At a given interval of time, a single TMUX ‘row’ (which consists of one detector in each column) is connected to the readout line via a flux activated switch. In this way, the MCE cycles through the rows by connecting to them for a brief time interval. This technique of multiplexing allows for the read out of thousands of detectors on the focal plane using only a few wires instead of each detector being read out by a separate wire. The multiplexing framework is necessary because it drastically reduces the thermal loading on the focal plane from the readout wires. Additionally, it simplifies the

wire routing schematics and helps with space limitations.

2.3.4 Optics

BA is a dedicated experiment for the observation of primordial B -modes which peak at an angular scale of $\sim 2^\circ$ in the CMB. The optical design optimizes throughput while minimizing systematic uncertainties. The relatively large angular scale of the B -modes allows for a small aperture size (550mm) of the receivers while still achieving the required diffraction-limited resolution. The small aperture allows for a compact on-axis receiver design, which gives us the ability for a boresight rotation. The boresight rotation of the receiver gives us full polarization coverage of Q and U as well as controlling beam systematics. Furthermore, the entire optical system is cryogenically cooled which reduces thermal loading on the detectors.

Figure 2.7 shows a cross sectional view of the receiver with the optical elements labeled. The BA receivers use a simple two lens refracting design (diffraction-limited) which allows for a telecentric and flat focal plane surface with a focal plane diameter of 475.8mm [57]. The telescope has a f -ratio of $f/1.57$ and both the objective and field lenses are 650mm in diameter.

The internal optics of BA consists of several filters used to reduce radiative loading which dominates over the conductive loading in the receiver. A 1in. thick HDPE plastic window is needed to hold vacuum in the cryostat. The window lets in a fair amount of infrared radiation ($>100\text{W}$) so a Zotefoam⁴ IR load filter is placed between the window and the objective lens⁵. Both the objective and field lenses are made of HDPE⁶ and are thermally sunk to the 4K stage. Additionally, an alumina filter at 50K, a Nylon filter at 4K, and a metal-mesh low-pass filter at 250mK are placed in the optical path to reduce infrared loading.

⁴<https://www.zotefoams.com/>

⁵The top (skyward side) of the filter is at 300K but has an intentional temperature gradient to the 4K stage.

⁶Some of the BA receiver designs use alumina ceramic lenses instead.

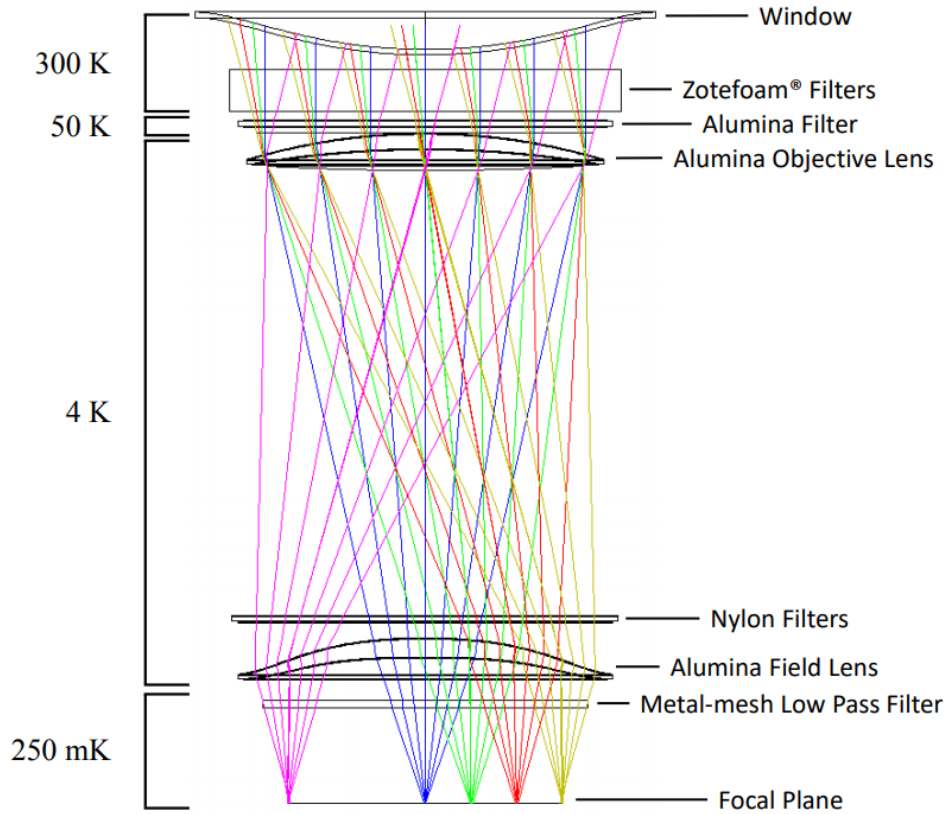


Figure 2.7: BICEP Array optical design diagram of the 30/40GHz receivers. Note: some BA receivers use HDPE for the objective and field lenses instead of alumina. All the optical components except the Zotefoam are anti-reflection coated. Figure courtesy of the BK Collaboration [49].

A 550mm cold (4K) aperture stop made from microwave-absorbing Eccosorb⁷ is located just above the objective lens (skyward side). The cryostat tube in the 4K stage between the lenses is baffled with Eccosorb to suppress far-sidelobe reflections.

Exterior to the cryostat are several additional optical elements which reduce systematics. For each receiver, a forebaffle is mounted at the top of the vacuum window and moves with the receiver which can be seen attached to the BA and Keck receivers in Figure 2.1b. The forebaffles, which are lined with Eccosorb, intercept the response to signals outside of the main beams. The telescope array sits inside of a cone shaped reflective ground shield which can also be seen in Figure 2.1. The ground shield prevents any line of sight from the ground

⁷Emerson & Cuming Microwave Products, Inc. Randolph, Massachusetts: Laird Technologies

to the receivers.

2.4 Raw Data to Power Spectra

This section will go into detail about how we take the raw data from the experiment and put it in a usable form (bandpowers) for our high level analysis. A detailed discussion of our analysis pipeline can be found in our BKII Collaboration publication [48] as well as a few Ph.D. thesis from collaboration members [58] [59]. As stated previously, the primary objective of the BK experiment is to measure a value of the tensor-to-scalar ratio, r . Because of this, the data analysis can be looked at as a giant data reduction process which condenses large amounts of time ordered data (TOD) into one value. Generally, the process goes as follows:

$$\text{raw TOD} \rightarrow \text{reduced TOD} \rightarrow \text{maps} \rightarrow \text{power spectra} \rightarrow \text{parameters}$$

The raw TOD is the data that comes from the TES detectors during a CMB observation. Most of the low level reduction of the raw TOD is done in the context of the scansets sandwiched by the leading and trailing elnods. The reduced TOD are data that has been filtered and put in a more usable form. The maps are made from coadding the reduced TOD from a season. The power spectra are the maps which have been transformed and put in the form of Equation 1.20 from Section 1.2.3. The parameters are the cosmological and foreground parameters we get from fitting our power spectra to a multi-component model. We use this parameterized model in our maximum likelihood (ML) search.

2.4.1 Time Ordered Data

Processing the TOD is the first step in our analysis pipeline. It is an automated process guided by graduate student members of the collaboration. Preliminary plots are generated from this process which are perused and discussed on a weekly basis. While this can be

somewhat tedious, the attention to detail and quick turnover rate ensures the experiment is running as intended. This is especially important for an experiment which is in limited communication and in a remote location. Figure 2.8 shows an example of the TOD detector data for a single scanset.

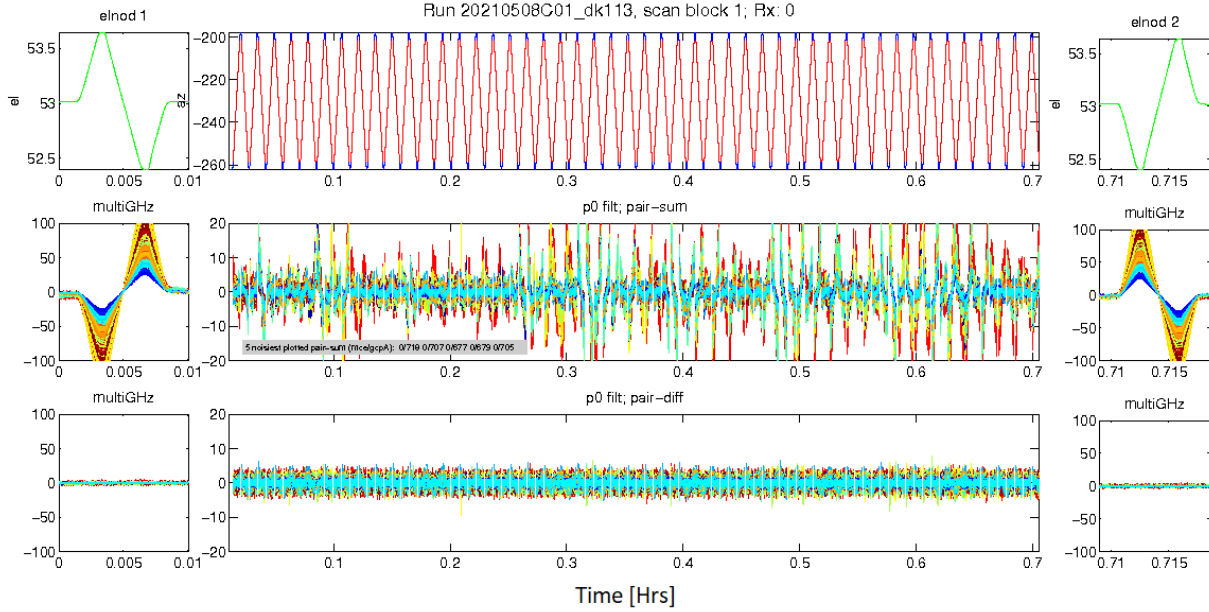


Figure 2.8: BA detector data from one scanset. The x-axis is time in hours where the whole scanset takes ~ 50 min. The top panels are the motion of the mount (explained more in Figure 2.4), the middle panels are the pair-sum of the detectors and the bottom panels are the pair-diff of the detectors. The far left (right) column of panels show the leading (trailing) elnods. The middle column shows the CMB scanset. The detector data is shown in arbitrary feedback units and after the round 2 cuts have been applied.

Deconvolution

As the TOD are collected by the TES detectors via time-domain multiplexing, the MCE downsamples after applying an anti-aliasing low-pass filter. The data are fed to GCP⁸ which further decimates and applies a finite impulse response low-pass filter. The resulting sampling rate of the detectors is ~ 20 Hz. Given our scan speed of $2.8^\circ/s$ in azimuth, this sampling rate is sufficient in targeting the B -modes contained in the $< 1Hz$ range. The first step in

⁸Generic Control Program (GCP) is a software control system responsible for reading out and storing the data from the telescopes.

processing the TOD is to deconvolve both the MCE and GCP filters (which are analytically known) [58]. This deconvolution also includes a low-pass filter to control noise [48].

Deglitching and Destepping

The next step in our data reduction is known as deglitching and desteping. Delta function spikes and discontinuous jumps sometimes show up in our TES data. For example, a spike can be caused by a cosmic ray hitting the bolometer island and a discontinuous jump can be caused by a change in the number of flux quanta, or ‘flux jump’, in the SQUIDs. Deglitching is the removal of a delta spike function in the TOD. The data 1sec before through 1sec after the spike are removed in this process. Destepping is the correction of discontinuous jumps in the data. In this data process, the jump is removed and the data from after the jump are matched with the data from before the jump.

Relative Gain

At this point, the TES detector data (in FBU) has been stored in the form of arbitrary analog-to-digit units (ADU), by the MCE. Because the data are read out in arbitrary units, each detector has a different gain. The relative gain or relgain process accounts for the different gain between each of the detectors on the focal plane by using the elnods. Both the leading and trailing elnods are used to fit $\sim 100\text{mK}$ unpolarized atmospheric temperature gradient for the detectors which is modeled by a secant function as $(1 \text{ airmass})/\cos(z)$ where z is the angle from zenith and 1 *airmass* equates to the amount of atmosphere when looking at zenith. The relative gain of each detector is then calculated against the median of all the receivers of the same observing frequency in the experiment. An absolute calibration later in the analysis converts the arbitrary ADU to μK_{CMB} . After the relgains, the sum and difference of orthogonal detector pairs are taken. The pair-sums will be used to make temperature maps and the pair-diffs will be used to make the polarization maps.

Data Cuts

With the relgain pair-sums and pair-diffs, we make a series of selections and cuts. These data cuts are made to exclude bad weather data and other atypical circumstances. A very common cut is made from the elnod goodness of fit which is an indicator of weather conditions. Another example is a cut made on focal plane temperature instabilities which can be caused by a fridge cycle running out early or the temperature control module not working. The cuts are made in two rounds. Round one cuts are made on halfscans and round two cuts are made on the full scanset. It is important to note that the selection and cuts still allow noisy data but they will be appropriately down-weighted. The purpose is to exclude data that are not easily compatible with our pipeline. Although, the cut statistics are calculated at this point, the data are not actually dropped until the map making stage.

Timestream Filtering

Some additional timestream filtering is applied to the remaining TOD. A third order polynomial is fit (in azimuth) to the individual halfscans and then subtracted. This reduces long time-scale drifts often caused by weather variations but does not interfere with our science bands. Another filter applied is called a ground subtraction and it removes signal that is azimuthally fixed in the scanset. The amount of power subtracted due to the filtering is tracked throughout the pipeline and accounted for later in the analysis; this is referred to as the suppression factor.

2.4.2 Maps

In short, making maps is the process of projecting the TOD signal from the detectors into celestial coordinates (RA and Dec). In this way, maps are a two dimensional binning of the weighted data accumulated over a certain amount of time into pixels⁹ of RA and Dec .

⁹The map pixels are 0.25° square in arc length.

Constructing Q and U

As described in Section 2.4.1, the detector pairs are summed and differenced. This can be related to the Stokes formalism described in Section 1.2.3 where a detector is sensitive to unpolarized T and linear polarization Q and U . If we take a pair of orthogonal detectors to be detector A and detector B , then the timestream signals can be described as:

$$d_A = T + Q\cos(2\phi_A) + U\sin(2\phi_A) + n_A \quad (2.2)$$

$$d_B = T + Q\cos(2\phi_B) + U\sin(2\phi_B) + n_B \quad (2.3)$$

Where d is the reggain normalized signal observed by the detector, T , Q , and U are Stokes temperature polarization parameters, and ϕ is the polarization angle of detector $A(B)$ with respect to Q . The noise of the A and B detectors are written as n_A and n_B , respectively. Here the noise of the detectors have zero mean but some variance. From a pair of detectors, the pair-sum and pair-diff will look like the following:

$$d^+ = \frac{1}{2} (d_A + d_B) \quad (2.4)$$

$$d^- = \frac{1}{2} (d_A - d_B) \quad (2.5)$$

Expanding out Equations 2.4 and 2.5 and, for simplicity, assuming the relationship that the detectors are orthogonal¹⁰ ($\phi_B = \phi_A + \pi/2 = \phi$) we get the following:

$$d^+ = T + \frac{n_A}{2} + \frac{n_B}{2} \quad (2.6)$$

$$d^- = Q\cos(2\phi) + U\sin(2\phi) + \frac{n_A}{2} - \frac{n_B}{2} = Q\alpha + U\beta + \frac{n_A}{2} - \frac{n_B}{2} \quad (2.7)$$

Where $\alpha = \cos(2\phi)$ and $\beta = \sin(2\phi)$. If we now consider that we make many observations of a pixel, then we can sum the data over the number of samples N . During this, we weight (w_i)

¹⁰In reality, we correct for non-orthogonality of the detectors in our pipeline through calibration measurements [60].

each respective detector pair by using the inverse variance of the timestream data during a scanset. In matrix form, We can now bin pair-sum and pair-diff which will allow us to eventually compute T , Q , and U :

$$\sum_i w_i \begin{bmatrix} d_i^+ \\ \alpha_i d_i^- \\ \beta_i d_i^- \end{bmatrix} = \sum_i w_i \begin{bmatrix} N & 0 & 0 \\ 0 & \alpha_i^2 & \alpha_i \beta_i \\ 0 & \alpha_i \beta_i & \beta_i^2 \end{bmatrix} \begin{bmatrix} T \\ Q \\ U \end{bmatrix} \quad (2.8)$$

Where the noise of the detectors sums to zero so the noise terms drop out (but still add variance). The temperature can simply be calculated through the pair-sum where as the pair-diff is a linear combination of Q and U . So the final calculation of our quantities requires a matrix conversion:

$$\begin{bmatrix} T \\ Q \\ U \end{bmatrix} = \left(\sum_i w_i \begin{bmatrix} N & 0 & 0 \\ 0 & \alpha_i^2 & \alpha_i \beta_i \\ 0 & \alpha_i \beta_i & \beta_i^2 \end{bmatrix} \right)^{-1} \left(\sum_i w_i \begin{bmatrix} d_i^+ \\ \alpha_i d_i^- \\ \beta_i d_i^- \end{bmatrix} \right) \quad (2.9)$$

Multiple detector angles are required in order to make the matrix invertible. These multiple angles are acquired through the boresight rotation of the telescope. The temperature can be decoupled from the polarization term if desired.

Systematic Beam Differences

In the calculation of Q and U it was assumed that detector pairs were perfectly orthogonal and matched. In reality, the beams are modeled with 2D elliptical Gaussians and even small mismatches in detector pairs cause a temperature-to-polarization ($T \rightarrow P$) leakage. Due to the relatively high CMB temperature signal compared to the CMB polarization signal, false polarization signals can come from a variety of pathologies. For modeling our elliptical Gaussian beams, we use a focal plane-fixed coordinates system that is specific to each detector $\vec{x} = (x, y)$. This coordinate system is defined for a detector pair by the intersection of two

orthogonal great circles with a common centroid of the detector beams. The six parameter 2D elliptical Gaussian looks like:

$$B(\vec{x}; g, \vec{\mu}, \sigma, p, c) = g \exp \left(-\frac{1}{2} (\vec{x} - \vec{\mu})^T \Sigma^{-1} (\vec{x} - \vec{\mu}) \right) \quad (2.10)$$

Where

$$\Sigma = \sigma^2 \begin{bmatrix} 1+p & c \\ c & 1-p \end{bmatrix} \quad (2.11)$$

The six parameters are: the normalization (or gain) constant g , the centroid of the beam $\vec{\mu} = (\mu_x, \mu_y)$, the beam width (standard deviation) σ , and the two ellipticity parameters, p for ‘plus’ ellipticity and c for ‘cross’ ellipticity.

If we consider two identical matched circular Gaussian beams from a pair of detectors A and B then the beams will point in the same direction ($\vec{\mu}_A = \vec{\mu}_B = \vec{\mu} = 0$) with well matched gains ($g_A = g_B = g$) and widths ($\sigma_A = \sigma_B = \sigma$). There will also be no ‘plus’ ellipticity ($p_A = p_B = p = 0$) or cross ellipticity ($c_A = c_B = c = 0$). Now, if we take the difference of these beams but perturb (δ) one of the six parameters (k), we can Taylor expand to first order. Doing this for all the parameters results in a set of six differential beam modes (B_δ) which only depend on the spatial derivatives in x and y . The six differential beam modes are [61]:

$$B_{\delta g} = \delta g B(x, y) \quad B_{\delta \sigma} = \sigma \delta \sigma (\nabla_x^2 + \nabla_y^2) B(x, y) \quad (2.12)$$

$$B_{\delta x} = \delta x \nabla_x B(x, y) \quad B_{\delta y} = \delta y \nabla_y B(x, y) \quad (2.13)$$

$$B_{\delta p} = \frac{\sigma^2}{2} \delta p (\nabla_x^2 - \nabla_y^2) B(x, y) \quad B_{\delta c} = \frac{\sigma^2}{2} \delta c (2 \nabla_x \nabla_y) B(x, y) \quad (2.14)$$

Where $\delta k = k_A - k_B$. The different types of $T \rightarrow P$ leakage are described by these six differential beam modes. Furthermore, these different types of leakages are characterized by their beam symmetries; monopole ($B_{\delta g}$ and $B_{\delta \sigma}$), dipole ($B_{\delta x}$ and $B_{\delta y}$), and quadrupole

($B_{\delta p}$ and $B_{\delta c}$). Figure 2.9 shows the $T \rightarrow P$ leakage which arises from the differential beam modes.

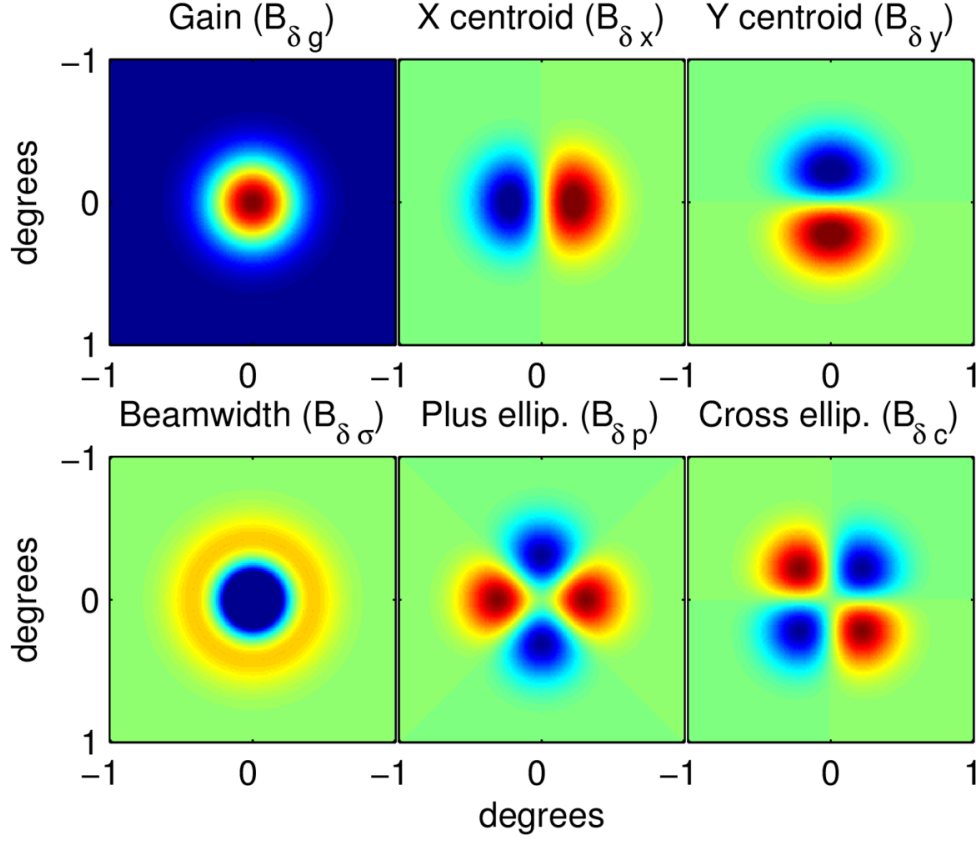


Figure 2.9: Differences of elliptical Gaussian beams. The ‘Gain’ and ‘Beamwidth’ panels are monopole symmetric $T \rightarrow P$ leakage. The ‘X centroid’ and ‘Y centroid’ panels are dipole symmetric $T \rightarrow P$ leakage. The ‘Plus ellip.’ and ‘Cross ellip.’ panels are quadrupole symmetric $T \rightarrow P$ leakages. Figure courtesy of the BK Collaboration [48].

A mismatch of gains in detector pairs (i.e., a circular Gaussian beam with a different height or width) leads to a $T \rightarrow P$ leakage which is monopole symmetric. The common mode signal is cancelled with the complementary deck angles which are 90° apart. This cancellation happens because under a 90° deck rotation, $Q \rightarrow -Q$ and $U \rightarrow -U$ with monopole symmetry. So assuming the sky coverage of a map pixel is the same at all deck angles, when the data are summed together (described in the previous section, 2.4.2), the $T \rightarrow P$ leakage will sum to zero. In the top left and bottom left of Figure 2.9, the monopole symmetric $T \rightarrow P$ leakage can be seen for a mismatch in Gaussian beam gain and beamwidth,

respectively.

Also seen in Figure 2.9 in the top center and top right panels are the dipole symmetric $T \rightarrow P$ leakages which arise from a mismatched centroid of beams among detector pairs. In this case, a dipole symmetric false polarization signal leaks into the the real map. Similar to the monopole, the dipole symmetric leakage is cancelled under deck rotation. In the case of a dipole symmetry, a 180° deck rotation results in $Q \rightarrow -Q$ and $U \rightarrow -U$. So again, assuming sufficient and equal coverage of deck angles which are 180° apart, the false polarization signal from the $T \rightarrow P$ leakage will be suppressed when the data are summed.

The most problematic leakage comes from the quadrupole symmetric signal which arises from a mismatched ellipticity in the beam difference seen in the bottom center and bottom right panels of Figure 2.9. The quadrupole $T \rightarrow P$ leakage from beam ellipticity mismatch looks like a real polarization pattern on the sky. This means that no combination of deck rotations will suppress this systematic error.

Deprojection

The various deck rotation combinations will cause much of the monopole and dipole $T \rightarrow P$ leakage signals to cancel. However, there will still be some false polarization left due to unequal detector and deck coverage. In order to deal with this remaining monopole and dipole leakage (and other potential problems), we apply a filter which we call deprojection. This involves using the Planck temperature map¹¹ (and its derivatives) as a template [62].

The differential beam modes ($B_{\delta k}$) described previously in Equation 2.12 are mapped onto the derivatives of the temperature map ($d_{\delta k}$) through convolution ($*$) of the temperature map (T) and the differential mode as $d_{\delta k} = T * (\nabla B_{\delta k})$. To make the deprojection maps, we apply a linear regression to fit the $T \rightarrow P$ leakage modes giving us six coefficients which characterize the $T \rightarrow P$ leakage and allow us to remove it. Figure 2.10 shows the six coefficients which we fit in the deprojection filter. With the monopole and dipole terms, we can simply use the

¹¹We use the Planck frequency which is closest to the observing frequency.

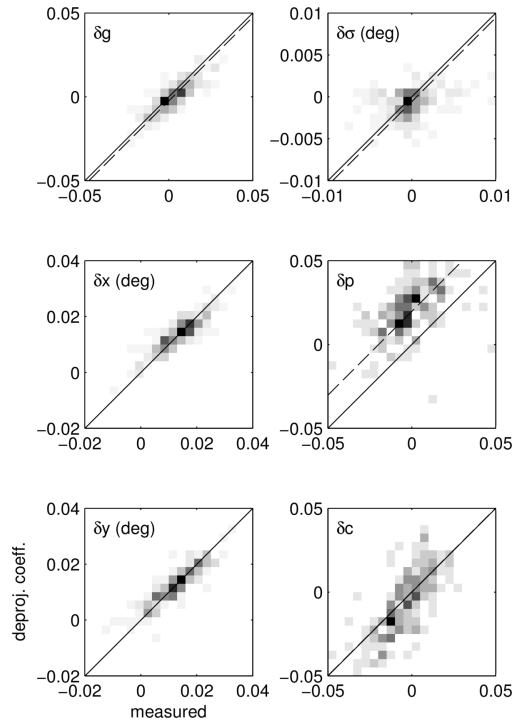


Figure 2.10: 2D histogram plots of detector pairs as they relate to the differential beam parameters. The horizontal axis of the plots are from the measured beam maps of the detector pairs. The vertical axis of the plots are the deprojection templates made from the Planck temperature maps. The solid line shows a line with a slope of 1 and y-intercept of 0. The dashed line shows a line with a slope of 1 but a y-intercept that is the bias calculated from simulations. Figure courtesy of the BK Collaboration[61].

deprojection templates and fits to remove them. However, because we expect real correlation between the E -mode polarization and temperature of the CMB, we deal with the quadrupole leakages slightly different. In this case, the measured beam maps are used to create the expected leakage from the mismatched beam ellipticity and subtracted from our maps.

Absolute Calibration

Up until this point, there was a relative detector gain calibration applied. It is now typical to perform an absolute calibration using the Planck temperature maps to convert the arbitrary units of ADU to μK_{CMB} . We use binned multipoles, called ℓ bins, to calculate the calibration

for a map. The calibration will look like:

$$g_\ell = \frac{\langle m_{ref} \times m_{cal} \rangle_\ell}{\langle m_{ref} \times m_{uncal} \rangle_\ell} \quad (2.15)$$

Where m_{cal} is the external temperature map used for the calibration. Typically, we use the Planck map with the closest bandcenter frequency as the receiver we are trying to calibrate. m_{ref} is another external map used for the calibration, conventionally Planck 143GHz. Because the maps have uncorrelated noise, the resulting cross spectra will be unbiased. Lastly, m_{uncal} is the map we wish to calibrate. It is also crossed with the reference map to make a noise debiased spectra. While we are primarily measuring polarization with our experiment, it is easier to use the temperature of the CMB to calibrate. This is because the temperature signal of the CMB is much higher than the polarization signal. It is also important to note that we account for the polarization efficiency of our detector in our absolute calibration [63].

Power Spectra

After data are binned into maps and calibrated, the next step is to make power spectra. As stated previously, the maps have pixels which are in the celestial coordinates of RA and dec . Because we are only using a small part of the sky, we use a flat sky approximation¹² to convert our real-space 2D maps into ℓ -space maps using a Fourier transform. In addition to using a Discrete Fast Fourier Transform (DFFT), we apply a window function to apodize the maps. The apodization downweights the edges of the map which are noisier due to being observed less often. Additionally, it provides a smooth transition for the edge of the map to zero which provides better conditions for a well-behaved transform. So instead of the spherical harmonics described in Equation 1.18 of Section 1.2.3, we use the analogous Fourier transformations, denoted by a hat: $\hat{T}(\ell_x, \ell_y)$, $\hat{Q}(\ell_x, \ell_y)$, and $\hat{U}(\ell_x, \ell_y)$. Where ℓ_x and

¹²These distortions are accounted for in our pipeline but have little effect since we are not looking for sharp features in the power spectra.

ℓ_y refer to the coordinates in Fourier-space and are a scaled version of the more familiar angular wave numbers k_x and k_y .

In order to get the Fourier maps in the more useful form of the multipole, we simply express (ℓ_x, ℓ_y) in radial coordinates (ℓ, ϕ) using $\ell = \sqrt{\ell_x^2 + \ell_y^2}$ and $\phi = \tan^{-1}(\frac{\ell_y}{\ell_x})$. We are now able to easily transform into E -modes and B -modes in Fourier-space through a rotation (described Equation 1.19 in Section 1.2.3):

$$\hat{E}(\ell) = \hat{Q}(\ell)\cos(2\phi) + \hat{U}(\ell)\sin(2\phi) \quad (2.16)$$

$$\hat{B}(\ell) = \hat{Q}(\ell)\sin(2\phi) - \hat{U}(\ell)\cos(2\phi) \quad (2.17)$$

Figure 2.11 shows how the signal shows up in the Fourier plane in Q and U and how that translates to a signal in E and B . The E -modes are much brighter which can be seen on the x and y axis of the Q Fourier plane and on the 45° rotated axes in the U Fourier plane. The red annuli are how we bin the ℓ values, where each bin spans ~ 35 multipoles wide. For our science bins, we use nine bandpowers spanning the range $20 < \ell < 340$. The ℓ bins are denoted with a prime, ℓ' and are the average of the ℓ values.

Lastly, we convert $\hat{E}(\ell)$ and $\hat{B}(\ell)$ into the quadratic power spectra by multiplying by another spectra:

$$C_{\ell'}^{TT} = \langle \hat{T}(\ell) \hat{T}(\ell)^* \rangle_{\ell'} \quad C_{\ell'}^{TE} = \langle \hat{T}(\ell) \hat{E}(\ell)^* \rangle_{\ell'} \quad (2.18)$$

$$C_{\ell'}^{EE} = \langle \hat{E}(\ell) \hat{E}(\ell)^* \rangle_{\ell'} \quad C_{\ell'}^{TB} = \langle \hat{T}(\ell) \hat{B}(\ell)^* \rangle_{\ell'} \quad (2.19)$$

$$C_{\ell'}^{BB} = \langle \hat{B}(\ell) \hat{B}(\ell)^* \rangle_{\ell'} \quad C_{\ell'}^{EB} = \langle \hat{E}(\ell) \hat{B}(\ell)^* \rangle_{\ell'} \quad (2.20)$$

This is now in the form of a CMB power spectra which was described in Section 1.2.2 in Equation 1.13. The binned quadratic power spectra are often referred to as bandpowers and are in units of μK . We use bandpowers in our multi-component model of cosmological parameters and foregrounds, which provides a constraint on r . High level analysis, including

extensive use of bandpowers, will be discussed further in Chapter 4.

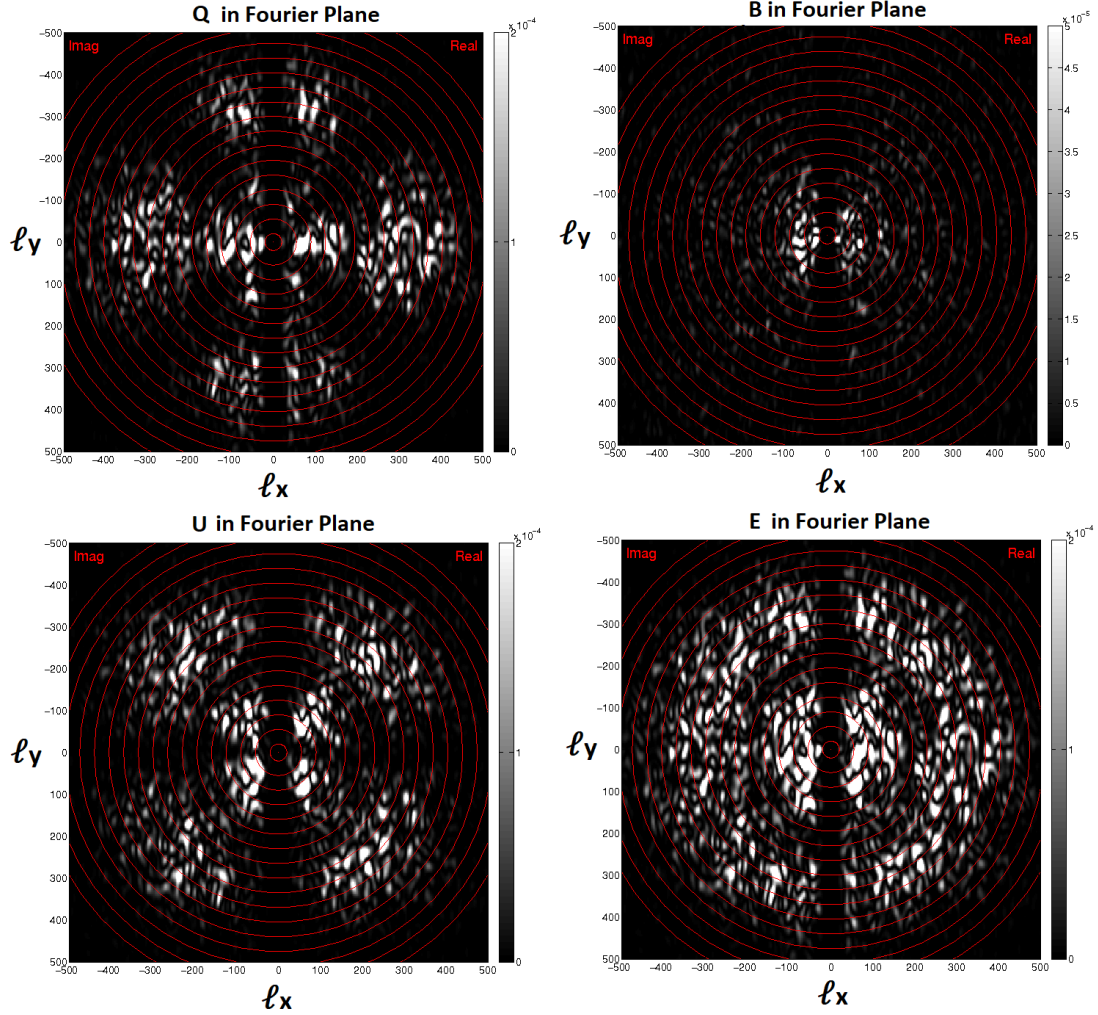


Figure 2.11: BK15 (150GHz) Fourier maps. Because E -modes are more prevalent, it shows up on the x and y axes of the Q map and the 45° rotated axes of the U map. The right side of the plots show the real part of the plane and the left sides show the imaginary part. The red annuli represent the bins which we average together to get our ℓ -bins. The trench close to $\ell_x = 0$ is due to the 3rd-order poly subtraction filter. The color scale units are in μK^2 .

Chapter 3

BICEP Array Housekeeping Electronics

The Housekeeping (HK) subsystem in BA has three functions: (1) reading out the temperatures at the various stages of the cryostat, (2) providing power for the resistance heaters used in the fridge and temperature control of the focal plane, and (3) providing auxiliary readout for forebaffle temperatures, calibration hardware, and any other miscellaneous electronics. There are four types of thermistors used to readout temperatures in the HK:

1. **Silicon diode thermistor** – A DT-670 Lake Shore¹ silicon diode. Primarily used to read out temperatures on the 50K and 4K stages.
2. **Lake Shore Cernox thermistor** – A thin film thermistor used for its high dynamic range (100mK to 400K) and increased sensitivity at lower temperatures. Used to read out temperatures on the 4K stage, the sub-K stage, and fridge.
3. **Allen-Bradley carbon thermistor** – A thermistor used to read out fridge temperatures. These thermistors use the same readout circuitry as the Cernox.
4. **Neutron transmutation doped (NTD) germanium thermistor** – A thermistor used at sub-Kelvin temperatures [64]. These are used with junction field-effect transistors (JFET) for a high impedance readout. The NTDs are used in the temperature

¹<https://www.lakeshore.com/>

control and readout of the focal plane.

In short, the diodes are the simplest to readout but are the least precise, the Cernox (and Allen-Bradleys) are more difficult to readout but provide better precision, and lastly, the NTDs are the hardest to readout but provide the best precision.

While all of the thermistors and heaters are located inside the cryostat, they all are routed to warm HK electronics located outside of the cryostat. There are 8 different types of daughter cards contained in the Backpack (Section 3.2) which are used for the analog signal processing of the different thermistors and heaters. These daughter cards are discussed in detail in Section 3.3. After the Backpack and daughter cards, the signals are routed to a commercial data acquisition (DAQ) electronics crate where they are digitized. A software system called GCP (Generic Control Program) is responsible for reading out and storing the data.

3.1 Design Overview

The design of the BA HK was built upon the previous design of the Housekeeping systems which were used in BICEP2, BICEP3, and Keck Array. Figure 3.1 shows a block diagram of the old HK design used for the warm electronics in BICEP2. The receiver (in orange) is connected to a Backpack (blue and green) where a multitude of analog and digital-to-analog converter electronics boards process the signals going to and from the receiver. The data acquisition is via the BLASTbus (red) which is a custom system made by University of Toronto [65].

One of the major changes in the new BA HK design was the use of a commercial DAQ system instead of the now discontinued BLASTbus. In order to simplify the whole HK system with the new DAQ system, the BA Backpack was designed to be fully analog. While some of the core analog circuitry designs remained the same as previous experiments, there was a fair amount of design rework in order to change the Backpack to fully analog. Additionally,

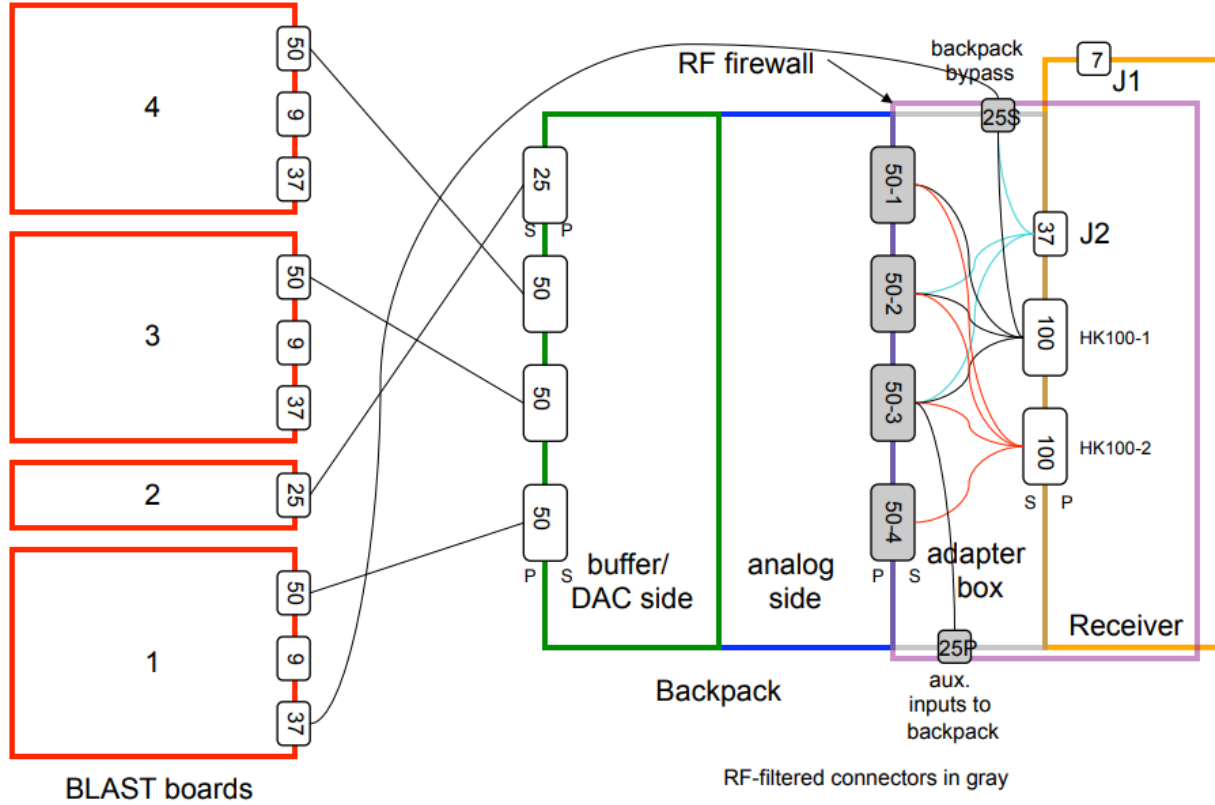


Figure 3.1: BICEP2 Housekeeping block diagram. The Backpack was half analog (blue) and half digital (green) in order to connect to the BLASTbus DAQ system (red). While this design worked, it is no longer viable due to the discontinuation of the BLASTbus. Figure courtesy of the BK Collaboration.

the new BA HK system is able to accommodate more readout channels despite its more compact design.

The new HK system for BA uses a commercial DAQ crate created by United Electronic Industries² (UEI) called the "Racktangle". It contains twelve modular slots for different types of boards. The BA HK system uses analog input boards (AI-207) and analog output boards (AO-332) for the receivers. Because all of the digital-to-analog conversion is within the UEI crate, there is no longer a need for the warm electronics in the Backpack to contain this function so the Backpack is completely analog. Additionally, we are able to use extra modular slots for a quadrature encoder board (QUAD-604) which is very useful for our calibration hardware.

²<https://www.ueidaq.com/>

The AI-207 is a 16-channel, 18-bit differential analog input board with an aggregate sampling rate of 16kHz (1kHz/ch). The AO-332 is a 32-channel, 16-bit analog output board. Each receiver uses five slots (4 AI, 1 AO) which amounts to 64 analog input channels and 32 analog output channels per receiver. Because the UEI crate has 12 slots, two receivers are used per UEI crate with two additional slots for auxiliary I/O. Figure 3.2 shows the new BA HK block diagram of how the warm electronics are configured for a single receiver.

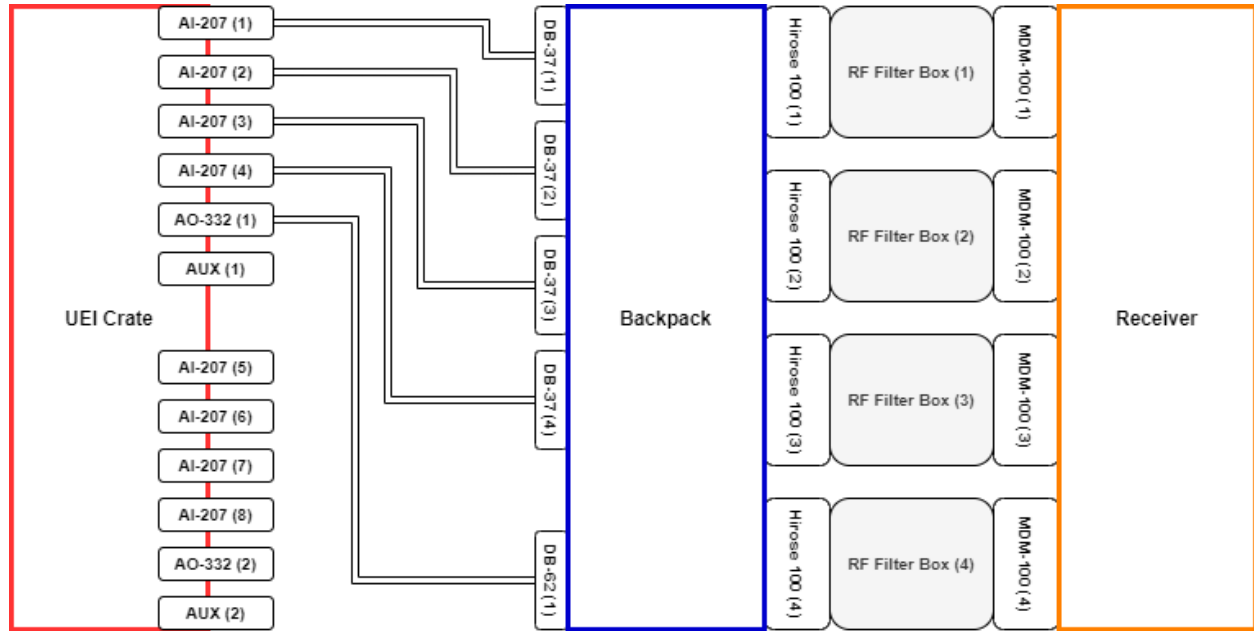


Figure 3.2: Bicep Array Housekeeping block diagram. The Backpack (blue) is completely analog unlike previous experiments. A single UEI crate (red) is able to service two full receivers and have two auxiliary modular slots.

GCP (Generic Control Program) is the software responsible for the control of the telescope and the high level data acquisition. GCP has two register speeds referred to as ‘fast’ and ‘slow’. The fast register samples at 200Hz which is triggered by a 200pps signal. This signal is provided by a Meinberg³ SyncBox N2X which synchronizes to NTP (Network Time Protocol). The slow register samples 20 times slower by throwing out 19 of every 20 samples. Currently, the UEI crate is running off its own clock and also sampling at 200Hz. GCP then requests data from the UEI Crate at every 200pps trigger. There is no strict timing so the

³<https://www.meinbergglobal.com/>

UEI crate just gives the most recent sample.

The sampling rate we use in GCP is set by the sampling rate of the detectors. There is little reason to sample at very fast rates during normal CMB observations because all of our science data is $< 1\text{Hz}$. We also benefit from a reduced data size when transferring our data to North America via satellite. So while GCP is capable of sampling at 200Hz, in practice, the data is down sampled to $\sim 20\text{Hz}$ (fast) and $\sim 1\text{Hz}$ (slow). A notable exception is that we use the full sample rate for calibrations such as beam mapping.

Even though, the AI-207 has the capability to readout all 16 channels at 1KHz, in practice, they are read out at 200Hz and then down sampled. Consequently, to reduce noise, the HK readout is filtered in the analog much below the maximum sampling rate of the AI-207. Much of the HK system uses the slow sampling rate but a few devices require the use of the fast rate. Most notably, all of the NTDs and the heaters associated with the temperature control modules (TCMs) use the fast data rate. Also, the fast sampling rate is used with a few diodes which are in close thermal proximity of the pulse tube cryocooler.

3.2 Backpack

The HK Backpack is mounted directly to the “back” of the receiver, using radio frequency (RF) filter boxes. The RF filters prevent nuisance signals from entering through the HK wiring and interfering with detector readout. There are five MDM-100 connectors on the receiver for HK purposes but one is unused ⁴. The four connections that are used in the warm electronics are labeled by the location of the thermistors and heaters inside of the cryostat:

1. **Cryocooler** – The thermistors and heaters associated with the pulse tube cryocooler (50K and 4K cold stages). Includes diode thermistors and low power heaters.

⁴The unused MDM-100 connector was for the case where Cernox thermistors would be used for focal plane temperature control instead of NTDs

2. **Fridge** – The thermistors and heaters connected to the sorption fridge. Includes Cernox and Allen-Bradley thermistors. Also includes high and low power heaters.
3. **JFET** – The thermistors and heaters connected to and via the JFET module. Includes the NTDs which are connected to focal plane via the JFETs. Also includes the JFET module power and low power heaters for the JFET module.
4. **Sub-K** – The thermistors and heaters connected to the sub-Kelvin cold stages. Includes Cernox and diode thermistors. Also includes low power heaters.

Each Backpack consists of: one Motherboard (MB), one Reroute board, four RF filter boxes, and 36 daughter cards. There are 8 different types of daughter cards which read out the different thermistors and control the different types of heaters. Table 3.1 gives a breakdown of how the different types of channels are distributed to the cryostat. The MB routes

		MDM-100 Connector				Totals
		Cryocooler	Fridge	JFET	Sub-K	
Daughter Card Type	Heater Amp	0	2	0	0	2
	Heater Buffer	16	2	3	8	29
	JFet Power	0	0	1	0	1
	Cernox	0	8	0	14	22
	Diode	16	0	0	6	22
	NTD Bias	0	0	16	0	16
	NTD Lockin	0	0	16	0	16
	NTD Osc.	0	0	0	0	0
Totals		32	12	36	28	108

Table 3.1: Number of channels going to each MDM-100 connector. The NTD Osc. is a board that is used for a local oscillator internal to the MB and, therefore, does not route outside of the Backpack. Note: Most of these channels are two wire and some of them are four wire.

the signals from the cryostat and UEI crate to their appropriate daughter cards for analog signal processing. Between the MB and the cryostat, the Reroute board routes signals to the RF filter boxes which go to the appropriate MDM-100 connection. The Reroute board is an artifact from the Keck Housekeeping system but it was kept in order to add routing

flexibility. Figure 3.3 and shows a top down view of the MB in a layout block diagram and Figure 3.4 shows a similar view for the Reroute board.

While the diagram does not explicitly show it, there is an RF filter box between the reroute board and the cryostat MDM-100 connectors. The RF filter boxes are the same design used for the Keck and B3 HK. This allows for re-purposing old Keck RF filter boxes.

The physical enclosure for the Backpack is an aluminum box with the (rough) dimensions of 14.5in x 5.75in x 10.5in. There is one Backpack per receiver. The MDM-100 mating to the cryostat is blind but needs to be fairly precise to prevent damage to the fragile pins on the connectors. To aid in the mating, there are two guiding pins on the Backpack which slide into mating holes on the cryostat. The ear flanges are then used to secure the enclosure. The blind mating of the four MDM-100 connections is accomplished through ‘captured’ steel rods which slide the RF filter boxes on a set of rails towards or away from the cryostat. Figure 3.5a shows the cryostat mating side of the enclosure and Figure 3.5b shows the opposite side with the DAQ cables and the ends of the steel rods.

3.2.1 Power Supply

The power supply is a small card mounted inside the Backpack. A fixed switching frequency (300KHz) DC/DC converter takes an external power of $+24V$ and $0V$ and converts it to $\pm 15V$. The power supply is also outfitted with a common mode choke and filter module to reduce common mode and differential mode noise. The converter is capable of a $40W$ output with a dual output current up to $\pm 1.667A$. This power supply card is used to power the entire Backpack which includes all of the analog daughter cards.

3.3 Daughter Cards

The 36 daughter cards in the Backpack do all of the analog signal processing. There are 8 different types of cards with some cards having multiple flavors. The Heater Amp, Heater

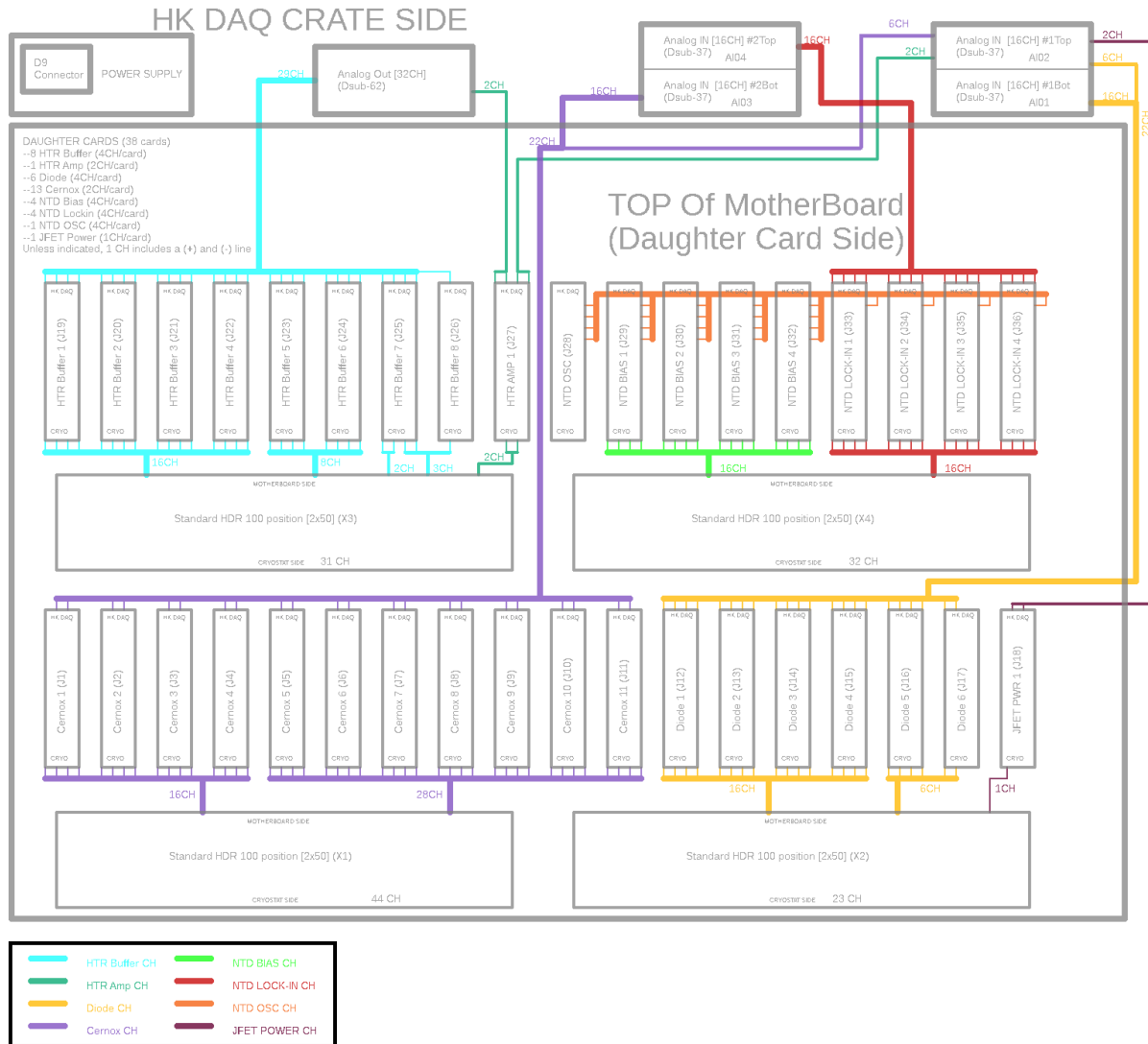


Figure 3.3: BA Motherboard layout block diagram. This view shows the ‘top’ side of the MB which is where the daughter cards slot in via a 50 pin standard header connector.

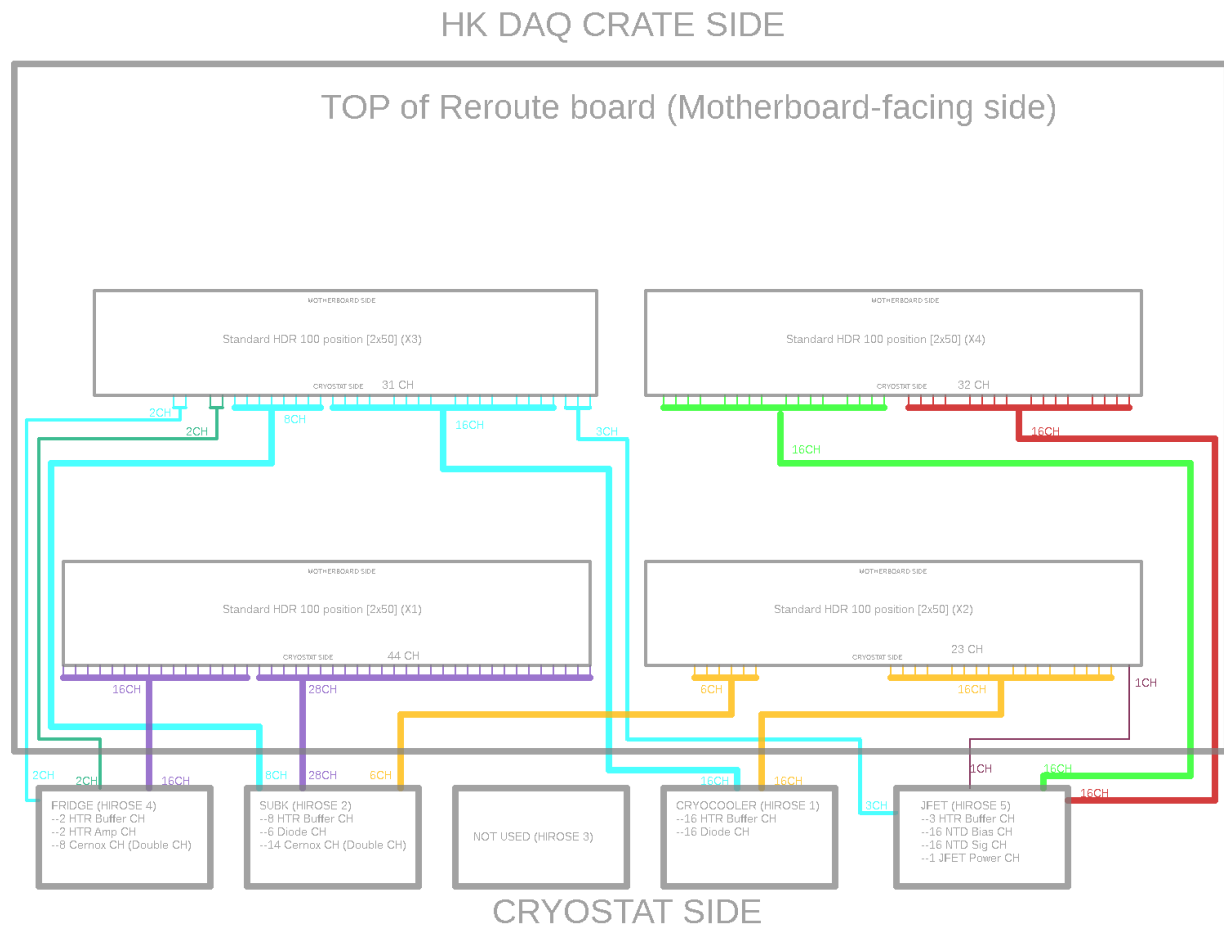
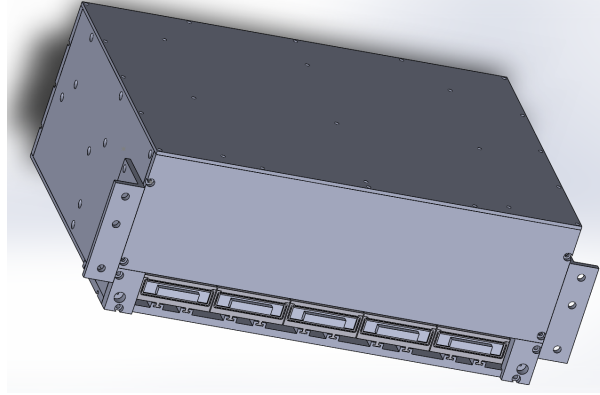
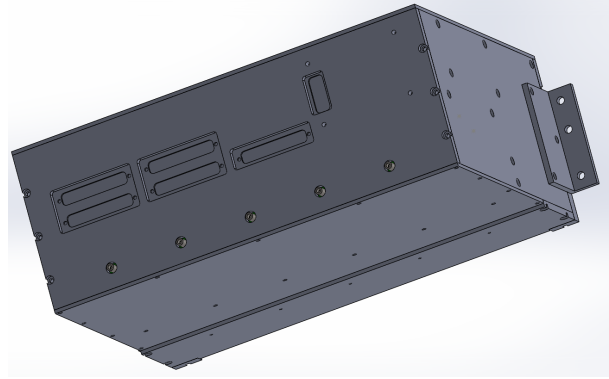


Figure 3.4: BA Reroute layout block diagram. This shows the ‘top’ of the Reroute board which plugs directly into the MB and reroutes the signals from the MB to the RF filter boxes which then connect to the cryostat.



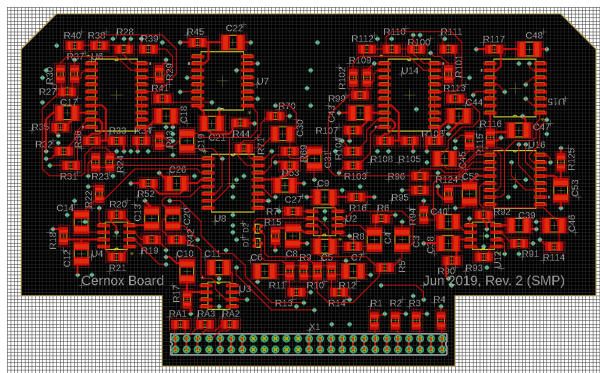
(a) Cryostat side view of the Backpack enclosure. The RF filter boxes can be seen at the bottom.



(b) DAQ side view of the Backpack enclosure. The five circles at the bottom are the ends of the steel rods for blind mating.

Figure 3.5: Two views of the Backpack enclosure model. Note: While there are five RF filter boxes shown here, there are only four used on the actual cryostat.

Buffer, and JFET Power are used to supply power to the various resistance heaters and the JFET module (Section 3.3.3). The Cernox, Diode, NTD Bias, NTD Lock-in, and NTD Oscillator cards are used for biasing and reading out the thermistors contained in the cryostat. Figure 3.6 shows an example of the PCB layout and the finished product of a daughter card (Cernox).



3.3.1 Heater Amp

The Heater Amp card is a two channel analog output which provides power to the pump heaters in the fridge. The heater resistors for both the He4 pump heater and the He3 pump heater are 201Ω . The max voltage output of the AO-332 is 10V which means the Heater Amp card is able to supply a $\pm 14V$, or ($28V$) output to the heater. At 201Ω , there needs to be about a $70mA$ of supply of current. However, the AO-332 is only able to supply $10mA$ and a typical op amp can only supply around $25mA$. In order to provide the needed power, the heater amp card is installed with a power op amp which is spec'd to supply $1.5A$. The power op amp is attached to a heat sink to dissipate any heat that it generates. Figure 3.7 shows a block diagram of the circuit. The transfer function for the voltage output going to the heater resistor is expressed as:

$$V_{out} = G_1 G_{P\pm} V_{in} = \pm 1.4 V_{in} \quad (3.1)$$

Each channel also has a current monitor which is read out by the AI-207. The current monitor converts the current going through the resistance heater to a voltage through a 2Ω sense resistor. This current monitor voltage is:

$$V_{cur} = \frac{I_{htr}}{R_{sense}} = \frac{V_{out}}{R_{htr} R_{sense}} \quad (3.2)$$

There is only need for one Heater Amp card because there are only two heaters which require this much power. The remaining heaters are sourced by the Heater Buffer cards which are lower power but have more channels.

3.3.2 Heater Buffer

The Heater Buffer card is a four channel analog output which provides power to the various low power heaters throughout the cryostat. Similar to the Heater Amp, the Buffer card

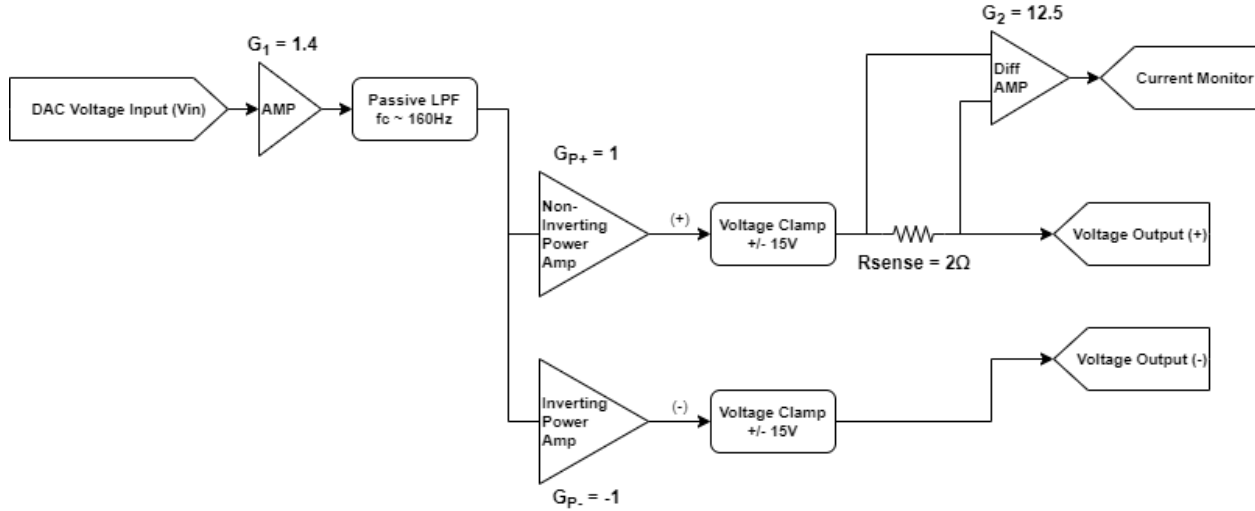


Figure 3.7: A block diagram of the circuit for the Heater Amp daughter card.

uses the AO-332 voltage output, which ranges from 0 to 10V, to control heater power. The buffer card uses a precision differential amp that is able to supply around 25mA (at 10V). Each channel has two operational states (high and low) which is selected by putting on

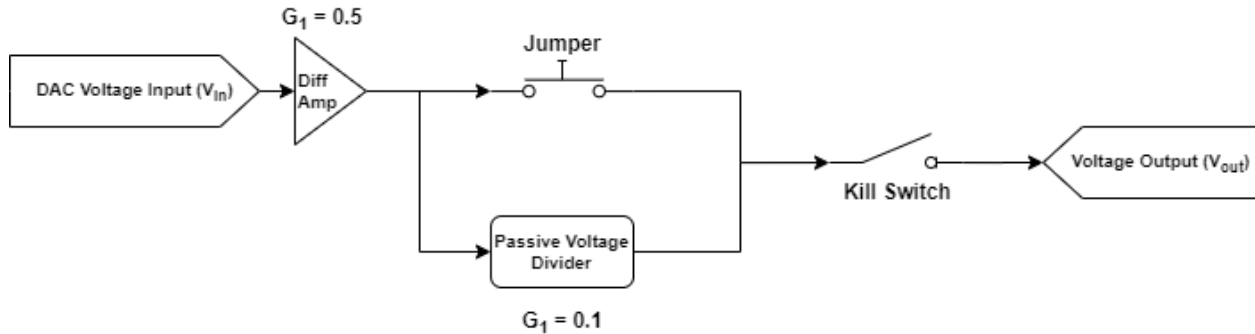


Figure 3.8: A block diagram of the circuit for the Heater Buffer daughter card.

(high) or taking off (low) a jumper. The ‘high’ voltage state is $\times 10$ that of the ‘low’ voltage state. This allows for more control on output range for the various heaters but must be set physically via a standard header shorting jumper. Another feature is a kill switch for each channel. This is a physical redundancy to ensure that there is not accidental heating in the cryostat. Overall the Heater Buffer card is a simple analog output card which supplies low power heaters in the cryostat. There are eight Heater Buffer cards per receiver, each with four channels which means 32 channels per receiver.

3.3.3 JFET

Junction field effective transistors (JFET) are used to create a high impedance follower of the NTD output. So the NTDs are biased directly but the output is via the JFET channels. The JFETs are contained in a JFET module which is housed in the 4K cold stage of the cryostat. The JFET module is re-purposed hardware originally designed for the SPIRE instrument inside the Herschel satellite telescope [66]. Each module contains 24 JFET channels, a resistance heater channel, and two power channels. The JFETs are temperature dependant but due to their location in the cyrostat and self-heating through the JFET power, the module does not require active temperature control. The JFET heaters are used for the event when the JFET module is too cold to self-heat. In this case, the heaters are used for applying heat to the module until it reaches a temperature where it can self-heat.

JFET Power

The JFET Power board is an analog power supply for the JFET module inside of the cryostat. There is no need for DAQ control over the JFET power; however, the power supply is physically tunable to each specific module. Two analog channels are read out by the AI-207 for power monitoring purposes. The JFET module needs a drain (V_{dd}) and a source (V_{ss}) power supply. V_{dd} is held constant at $+3V$. V_{ss} has a tunable output controlled by a trimmer potentiometer in the range of $0V$ to $-5V$. A typical V_{ss} for the JFET module is around $-1.5V$ and draws a current of $\sim 1.45mA$. A multi-output voltage reference is sufficient for supplying the needed power. Instrumentation amplifiers read the current across sense resistors placed on both the V_{ss} and V_{dd} . This provides the voltage output for the current monitors. There is only need for one JFET power card per receiver.

3.3.4 Cernox

The Cernox daughter card is a two channel analog card which reads out a Lakeshore Cernox (and Allen-Bradley) thermistor through the AI-207 UEI cards. The Cernox is used for

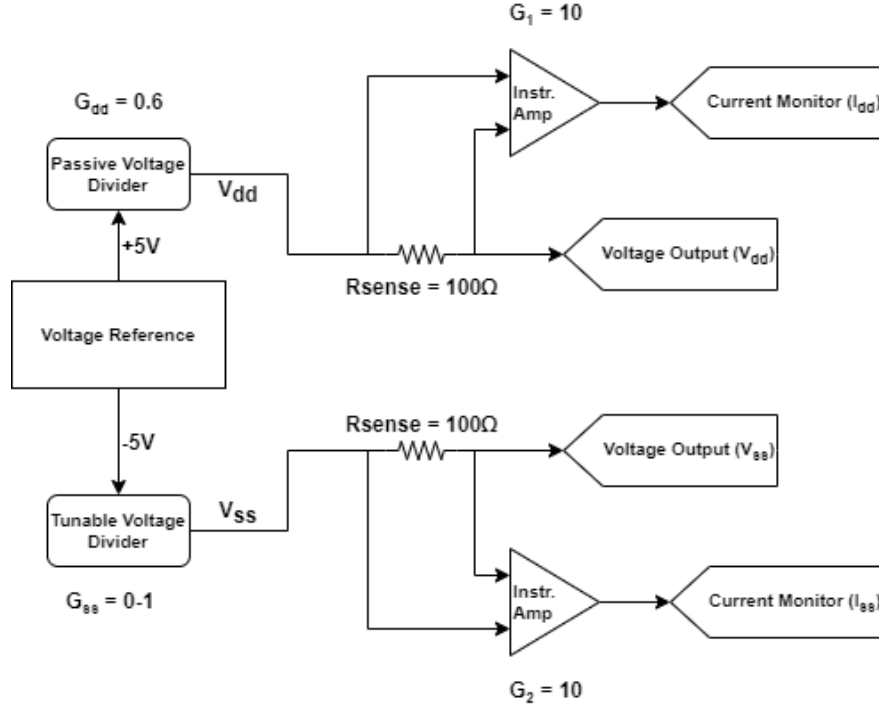


Figure 3.9: A block diagram of the circuit for the JFET Power daughter card.

its large dynamic operating range ($100mK$ to $400K$) while being most sensitive at low temperatures ($\pm 5mK$ at $1.4K$). Several different models of Cernox thermistors were used in the BA1 receiver in order to optimize readout based on the operating temperature of the respective location. In other BA receivers (and for future receivers), only one model of Cernox was used in order to simplify the warm electronics readout. In addition to reading out the Cernox thermistors, the Cernox daughter cards are also responsible for reading out several Allen-Bradley carbon thermistors. Each Backpack is equipped with 11 Cernox daughter cards which means a total of 22 analog readout channels.

The Cernox circuit provides AC current bias that is servo-looped to produce a specified AC voltage ($\sim 50\mu V$) across the thermistor. We read this current across a sense resistor, lock in to convert to DC, then filter and amplify the DC signal before digitizing. Figure 3.10 shows a block diagram of the circuit for the ‘vanilla’ or Flavor 0 version, which is the most basic design. The circuit only works across a certain range of device resistances. When the resistance of the Cernox is too low (higher temperatures), the output voltage is too high

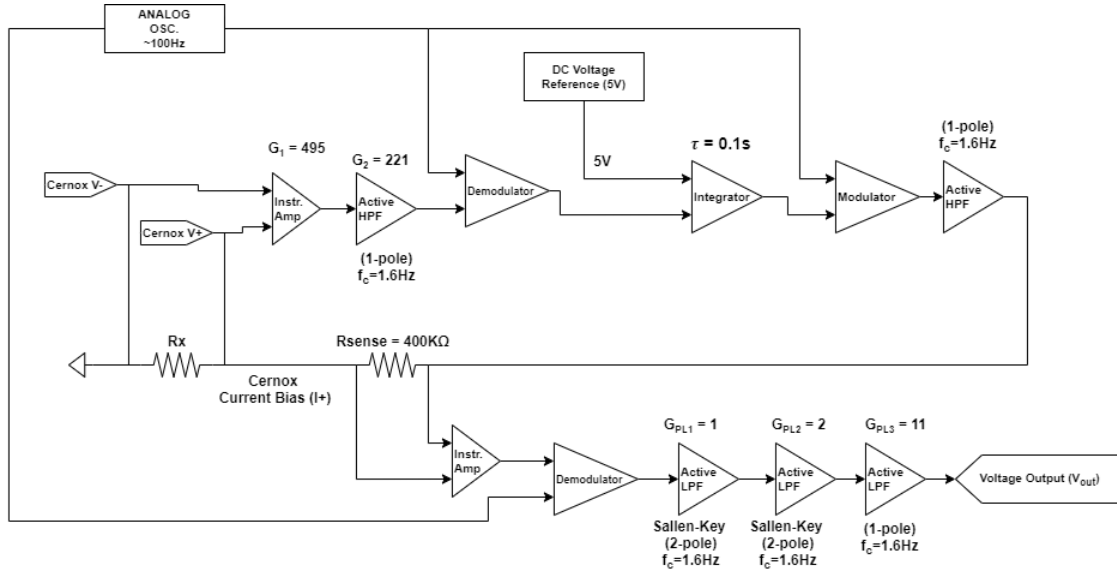


Figure 3.10: A block diagram of the circuit for the Cernox daughter card.

and the analog output of the circuit hits the 10V rail of the ADC. When the resistance is too high (lower temperatures), the time constant of the integrator in the servo-loop is too low. This causes a distortion in the sine bias signal which leads to instability from failure to properly lock on to the modulated signal. For this reason, there are three other 'flavors' to this Cernox design which change a few resistor and capacitor values to better optimize for a larger thermistor impedance. This will be discussed more in Section 3.5.5.

The calibration of the Cernox readout circuit converts device resistance to measured DC voltage from the AI-207 UEI card. The calibration is fit to the following function:

$$R_{dev} = \frac{G}{V - V_{off}} \quad (3.3)$$

with parameters:

G = circuit gain

V_{off} = offset voltage

V = Output Voltage

As stated previously, the operating temperature range is quite large for the Cernox ther-

mistor. However, the thermistor is most sensitive at lower temperatures which is also the range most important to operations. Because of this, the linear regression fit is weighted by thermistor resistance. A higher resistance means the thermistor is at a lower temperature and, thus, should be weighted more heavily.

3.3.5 Diode

The Diode daughter card is a four channel analog card responsible for reading out Lake Shore silicon diode (DT-670) thermistors in the cryostat. These diodes have an operating temperature range from $1.4K$ to $500K$ with $\pm 12mK$ at $1.4K$ and $\pm 32mK$ at $300K$. The large operating range make them a good tool in measuring the cool down of the cryostat and monitoring several of the ‘warmer’ stages which do not require as much precision. Each Backpack is equipped with six Diode daughter cards for a total of 24 diode readout channels per receiver.

A high precision voltage reference supplies $-5V$ to a feedback loop between an op amp and an instrumentation amp. This acts as a constant current bias ($10\mu A$) for the diode. The voltage drop over the diode (V_d) is measured using an instrumentation amp. This signal is then put through a low-pass filter and amplified before being digitized by a AI-207 UEI card. Figure 3.11 shows a block diagram of the circuit.

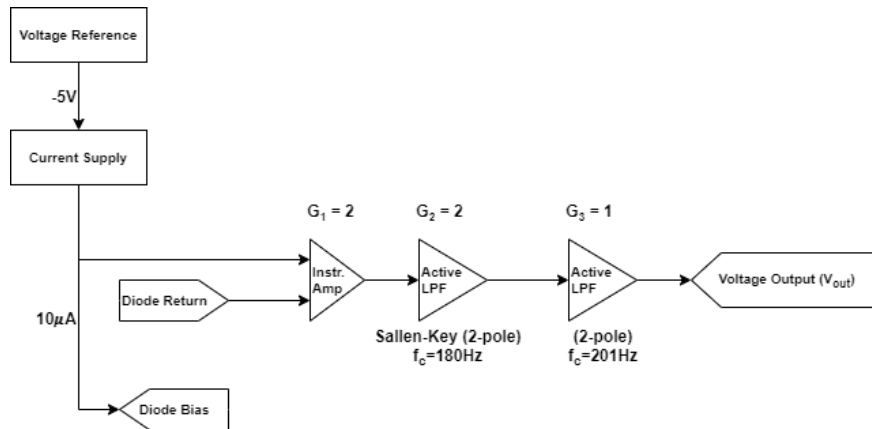


Figure 3.11: A block diagram of the circuit for the Diode daughter card.

In order to calibrate the individual Diode daughter card channels, we use a set of resistors to simulate the resistance of the diode. Our calibration converts measured voltage to device resistance through the equation:

$$R_{dev} = \frac{V - V_{off}}{GI_{bias}} \quad (3.4)$$

with parameters:

G = circuit gain

V_{off} = offset voltage

I_{bias} = current bias applied ($10^{-5}\mu A$)

The expected gain is 4 with an expected offset of 0V. The circuit only works across a certain range of device resistances. If the device resistance is too low, then DC output voltage required to drive the constant current bias is very low. If the device resistance is too high, the voltage required to drive the current hits the rails.

3.3.6 NTD Overview

The neutron transmutation doped germanium thermistors, or NTDs, are biased and read out by a combination of three different daughter card types:

1. NTD Oscillator (1 card/Backpack)
2. NTD Bias (4 cards/Backpack)
3. NTD Lock-in (4 card/Backpack)

Figure 3.12 shows the circuit bridge topology used to bias the NTDs. As shown in the figure, there is an AC bias on the NTD as well as another AC bias on the paired nulling resistor (NR). Also shown, is the JFET module inside the cryostat which is used to buffer the output of the NTD/NR bridge. The biases are created on the NTD Osc card and then routed to the NTD Bias cards to be manually tuned (amplitude and phase) via a set of potentiometers. These tuned biases are then sent to the NTD bridge in order to null the differential output at an appropriate operating resistance (temperature). The phase tuning was added in order to

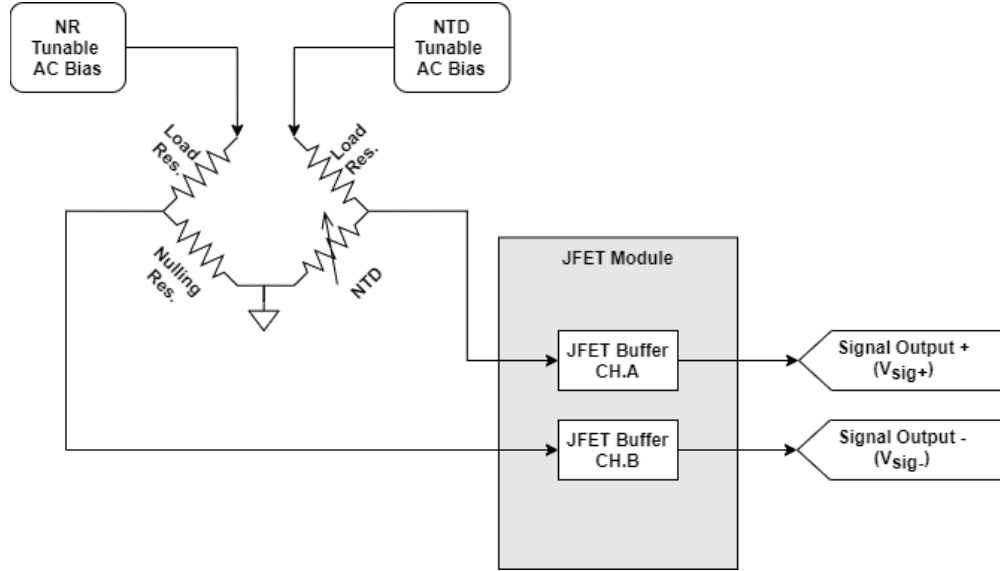
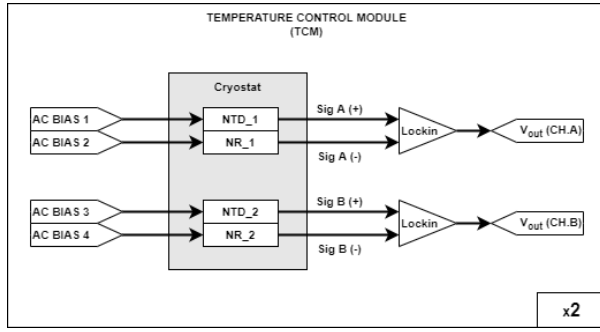


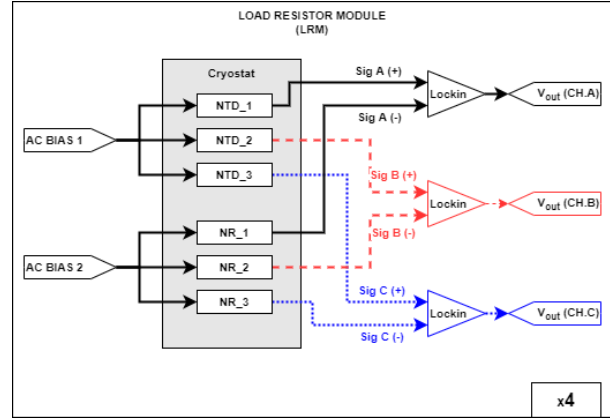
Figure 3.12: The bridge circuit used for the NTDs.

account for any phase delay present inside the different channels of the JFET module. The nulled differential output voltage is routed to the NTD Lock-in card where it is demodulated, filtered, and then amplified before being digitized. More details about the NTD tuning can be found in Section 3.5.3 and a detailed procedure on how to tune the NTDs can be found in Appendix A.1.

There are two modules that use the NTDs: the Temperature Control Module (TCM) and the Load Resistor Module (LRM). The TCMs are used to regulate the temperature of the focal plane via a PID loop. Each TCM contains two NTD/NR pairs, one on the dirty side of the heat strap and one on the clean side. In the case of the TCM, each NTD and NR are individually biased. The LRMs are used to readout focal plane temperatures on the different tiles. In total, there are 12 Tile NTD/NR pairs. However, unlike the TCMs, the LRMs are biased as triplets; one bias pair is used per three NTD/NR pairs. Figure 3.13 shows a flow of how the NTDs are biased in a cryostat.



(a) TCM flow diagram of bias and output.



(b) LRM flow diagram of bias and output.

Figure 3.13: Description of how the bias works for the different types of NTD modules.

NTD Osc.

The NTD Oscillator daughter card is an analog oscillator which requires no external control. It is set at a frequency ($\sim 408\text{Hz}$) and outputs four sine waves separated by a phase of 90° . These signals are routed to bias cards for additional amplitude and phase tuning. The signal is also routed to the NTD Lock-in cards used as the lock-in signal. There is only need for one NTD Oscillator daughter card per Backpack.

NTD Bias

The NTD Bias daughter card combines the four oscillation signals from the NTD Oscillator card to produce a tunable AC bias. Each NTD Bias card has four channels which means there are a possibility of 16 tunable biases per Backpack. The phase of the bias is tuned physically through a set of two jumpers and a potentiometer which allows for a 0° to 360° phase shift. The phase of bias is set completely by the relative position of this potentiometer but it also affects the amplitude of the bias. So if we consider the two input sinusoidal signals

(V_a and V_b) which are 90° out of phase ($\phi_a = \phi_b + \pi/2$) then the signals can be written as:

$$V_a = \sin(\omega_0 t + \phi_a) \quad (3.5)$$

$$V_b = \sin(\omega_0 t + \phi_b) \quad (3.6)$$

Where ω_0 is the frequency of the oscillator. The signals are then added to produce the following output:

$$V_c = \left(1 - \frac{R_a}{R}\right) V_a + \left(\frac{R_a}{R}\right) V_b = |A|V_a + |B|V_b \quad (3.7)$$

Where R is the total resistance of the potentiometer, R_a is the relative potentiometer resistance seen by V_a such that $R_a + R_b = R$, and $|A|$ and $|B|$ are the relative amplitudes given by the potentiometer. The resulting output amplitude and phase shift are then given by:

$$|C| = \sqrt{|A|^2 + |B|^2} \quad (3.8)$$

$$\phi_c = \arctan\left(\frac{|B|}{|A|}\right) \quad (3.9)$$

In this way, the phase tuning process is coupled with tuning the amplitude of the bias. Given that $0 \leq R_a \leq R$, then $\max(|C|) = 1$ when $R_a = 0$ or $R_a = R$ and $\min(|C|) = \sqrt{2}/2$ when $R_a = \frac{1}{2}R$. This also means $\phi_a \leq \phi_c \leq \phi_b$.

After the phase tuning, there is another potentiometer used for tuning only the amplitude of the bias. The amplitude tuning has a maximum of unity gain and a minimum of zero gain. Figure 3.14 shows a block diagram of how the NTD Bias card works. After the NTD

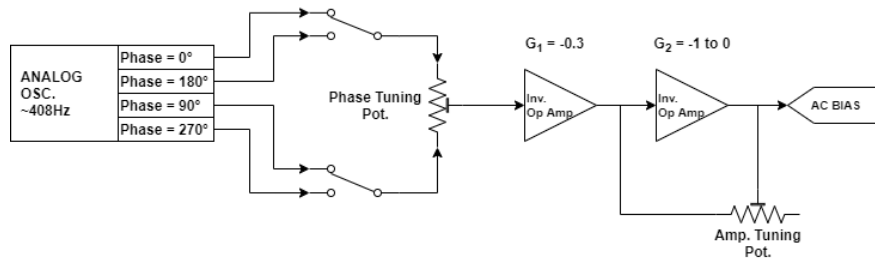


Figure 3.14: A block diagram of the circuit for the NTD Bias daughter card.

Bias cards are properly tuned for the receiver, they should not require any additional tuning unless there are changes to the NTDs. See Section 3.5.3 for more details on the NTD tuning.

NTD Lock-in

The NTD Lock-in daughter card uses the differential output of the NTD and NR bridge. Each signal is DC blocked and fed into a instrumentation amplifier. The deviation from the nulled signal is then demodulated using the output of the NTD Oscillator Card. Finally, the signal is filtered and amplified before being digitized by the AI-207 UEI Card. Each NTD Lock-in card has four channels which amounts to a total of 16 channels for each Backpack. The

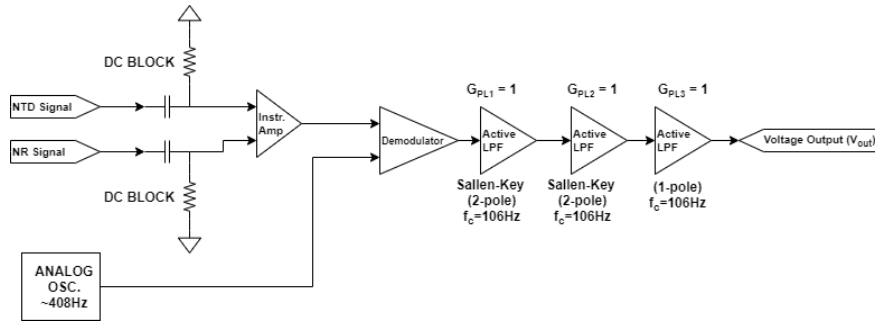


Figure 3.15: A block diagram of the circuit for the NTD Lock-in daughter card.

NTD readout is calibrated from Cernox during a fridge cycle and nominal cold operations. There is one Cernox which is used to calibrate the dirty side NTDs used in one of the TCMs. The NTDs located in the clean side TCM and the LRMs are all calibrated off a clean side Cernox. Because the NTDs are read out at the fast rate and the Cernox at the slow rate, the NTD voltages are averaged down before being associated with the coinciding Cernox temperature.

3.4 Auxiliary Readout

There are two slots per UEI crate (four total) which are not used for the primary HK electronics readout. One of these slots is populated with a AI-207 and is used for the

forebaffle temperature readout. Each of the four BA forebaffles is equipped with four AD590 thermistors (16 total). A 13V bias, supplied by the AI-207 card, is put on each of the AD590s. The AD590 then sources $1\mu A/K$ which is in series with $10K\Omega$ resistor. The voltage drop over the resistor is digitized by the AI-207 card and is given by Equation 3.10.

$$V_{out} = (1\mu A/K) * (Temp[K]) * (10K\Omega) \quad (3.10)$$

Originally, power was routed from an external source to supply the bias; however, it was determined that the AI-207 card power supply was sufficient at 50mA. For example, if we assume the AD590s are at 300K, then each one will draw $\sim 0.3mA$. If all 16 AD590s are being used, this would amount to $\sim 5mA$. This means that the power for the forebaffle AD590s is able to be completely supplied by the UEI crate via the AI-207 card and not from an external power supply.

Additional seasonal calibration equipment such as a beam mapper and rotating polarized source take advantage of the extra UEI slots. Much of the calibration equipment can simply use an AI-207 for a differential analog readout. The QUAD-604 UEI card is a four channel quadrature encoder readout that is also used for calibration equipment.

3.5 Performance and Improvements

3.5.1 Cernox and NTD Comparison

An NTD thermistor is more difficult to read out than a Cernox. This is apparent with the amount of different types of daughter cards; the Cernox requires only one type while the NTD requires three. In addition, to the several types of readout, the NTDs also require a cold JFET module to buffer the NTD signals. Figure 3.16 shows a comparison between a Cernox and NTD located at a similar location in the cryostat. Both in the timestream and in the power spectral density (PSD), it is apparent we get several orders of magnitude better

noise in the NTD.

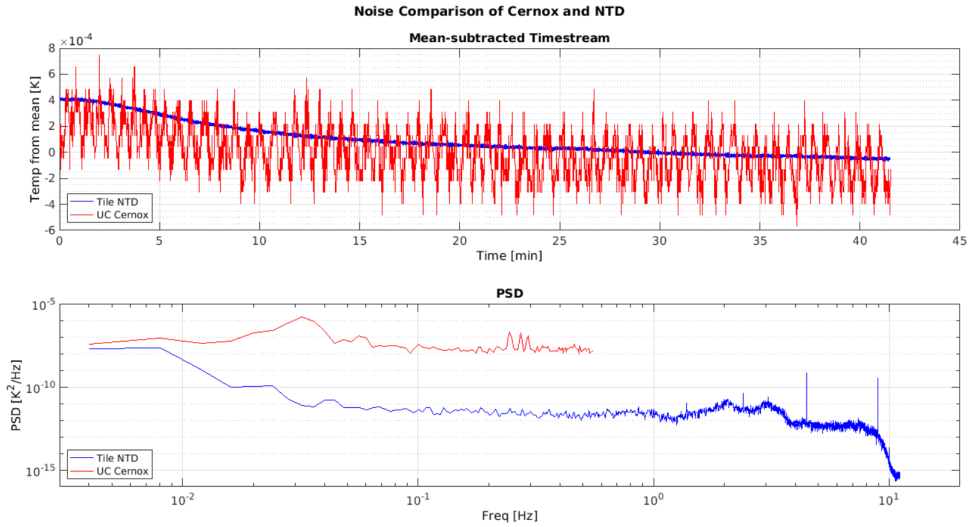


Figure 3.16: A comparison of the noise levels between an NTD (blue) and a Cernox (red) thermistor located on the clean side of the focal plane. The NTD is sampled 20 times more so the PSD extends higher. The ~ 30 s oscillations in the Cernox are from the scanning motion of the telescope. This scan synchronistic signal gets suppressed on the focal plane NTD from active temperature control.

3.5.2 BA and Keck NTD Comparison

The NTD thermistor provides a good point of comparison among the different generations of receivers. Figure 3.17 compares the tile NTD noise of a BA style receiver with the Keck style receivers. Because BA currently has both styles of receivers, it is relatively easy to compare the noise. Overall, the BA tile NTDs seem to perform as good or better than the Keck tile NTDs. The notable worse aspect of the NTD noise performance in the BA receiver comes with the two sharp lines seen in the PSD at ~ 4.5 Hz and ~ 9 Hz. The reason for these lines are explained in Section 3.5.7, but the fact that they are narrow lines above the science frequencies should provide some comfort.

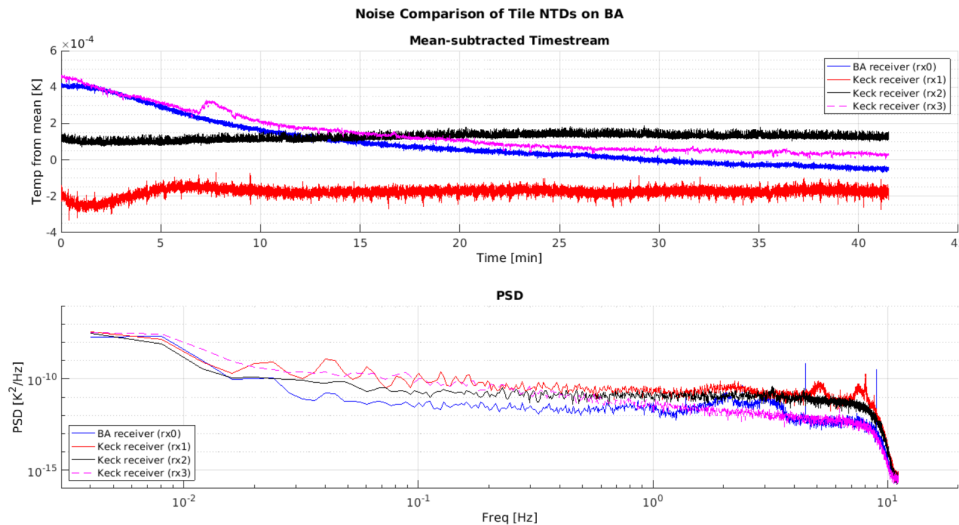


Figure 3.17: A comparison of the noise levels between a tile NTD (blue) on a BA style receiver vs. the Keck style receivers (red, black, magenta).

3.5.3 NTD Tuning

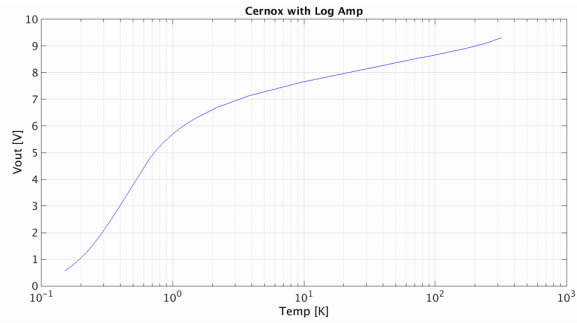
As stated in Section 3.3.6, the NTD Bias cards need to be manually tuned for each channel. The phase is tuned first because it also changes the amplitude. While the phase is tunable in the complete 360° of phase space, the two biases are generally within $\sim 10^\circ$ of each other. When the phase of the NTD and NR are properly aligned, the amplitudes are tuned to completely null each other out ($\sim 150\text{mV}$). For convenience, there are several connection test points on the NTD Lock-in (rev.2) daughter card. These are attachment points for oscilloscope probes which read out the AC-coupled biases individually as well as the differential between the two biases. For a detailed procedure⁵ of how to tune the NTDs, see Appendix A.1.

3.5.4 Cernox Output Gain

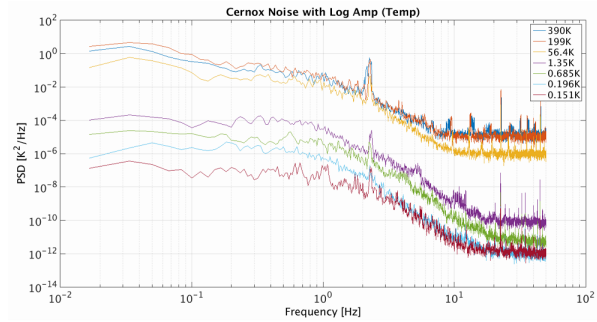
The original design (rev.1) for the Cernox daughter card used a logarithmic output. As shown in Figure 3.18, the log amp offered a relatively large dynamic range. It also shows how the log output was much more sensitive at lower temperatures. This seemed ideal for

⁵This is most useful for members of the BK Collaboration who have access to the HK schematic files.

our setup considering we only need the higher temperatures during cryostat warm-ups.



(a) Log output voltage response to different Cernox temperatures



(b) PSD of the Cernox log output.

Figure 3.18: The log output offered a larger dynamic range and was more sensitive at low temperatures.

Figure 3.19 shows the circuit schematic for the the log amplifier part of the original Cernox design. It consists of two log amplifiers (U1 and U2) and a differential amplifier (U3). Equation 3.11 shows the functional form of a single log amplifier. It has a dependency

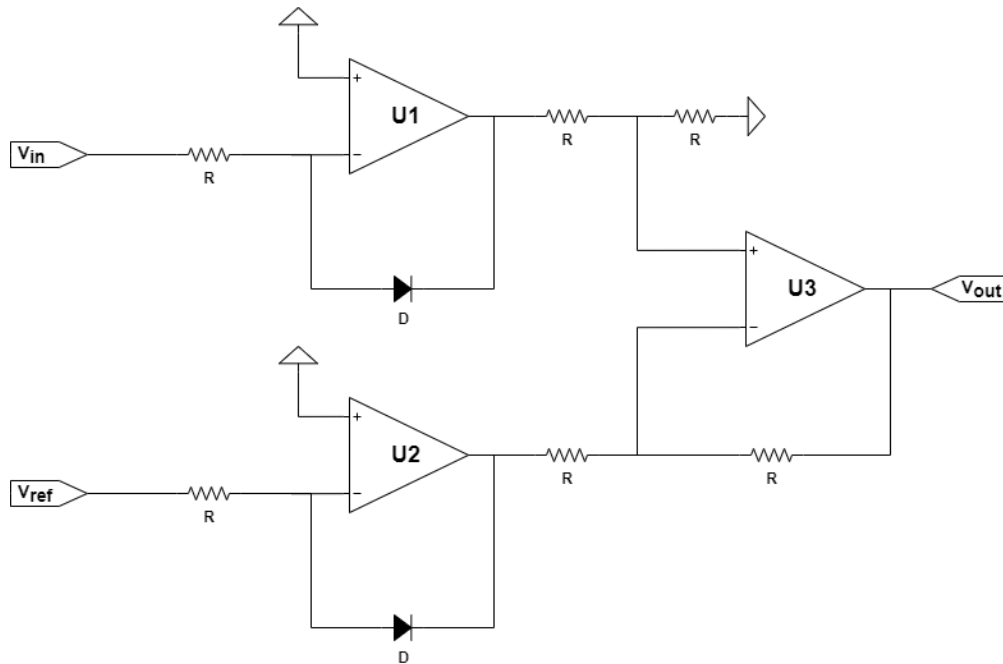


Figure 3.19: Block diagram of the log amp in the original Cernox daughter card design.

on the saturation current (I_s) and the thermal voltage (V_T) of the diode.

$$V_{out} = -V_T \ln \left(\frac{V_{in}}{I_s R} \right) \quad (3.11)$$

When put together with the differential amplifier, it cancels some of the dependency on the properties of the diode and results in Equation 3.12.

$$V_{out} = V_T \ln \left(\frac{V_{ref}}{V_{in}} \right) \quad (3.12)$$

In practice, the log output suffered from too much instability which rendered the Cernox readout unreliable for our purposes. While there was not a full investigation into the instabilities, it is believed they were due to temperature drifts in the diodes. The fix in the later design of the Cernox daughter card was to simply use a linear output and reduce the dynamic range so that we were not sensitive to higher temperatures. It is important to note that while the dynamic range was reduced, it still generously includes all of the nominal operating range of a cold cryostat.

3.5.5 High Impedance Cernox Circuits

As mentioned in Section 3.3.4, there are several different ‘flavors’ of the Cernox daughter cards. This was in response to the Cernox thermistor models and the Allen-Bradley (AB) thermistors which have much higher impedance. Table 3.2 gives a range of the target impedance for each ‘flavor’. For a detailed description⁶ of which components are changed in the circuit schematic, see Appendix A.2.

Initially, to account for the high impedance ABs, the AC bias across the thermistor was increased. While this did help, there was still a problem with the stability of the servo-loop. Figure 3.20 shows The difference between a 200 Ω (orange) Cernox impedance and a 20K Ω (blue) Cernox impedance using the old AB board design. Where ‘Vrx’ shows the voltage

⁶This is most useful for members of the BK Collaboration who have access to the HK schematic files.

Cernox Daughter Card Flavor	Target Impedance Range [Ω]
Flavor 0	0.4K - 4K
Flavor 1	10K - 30K
Flavor AB	20K - 30K
Flavor 2	50K - 110K

Table 3.2: Target Ranges for different flavors of Cernox daughter cars. Note: Flavor AB was an early flavor modification and the Flavor 1 board is now a more appropriate version of the board.

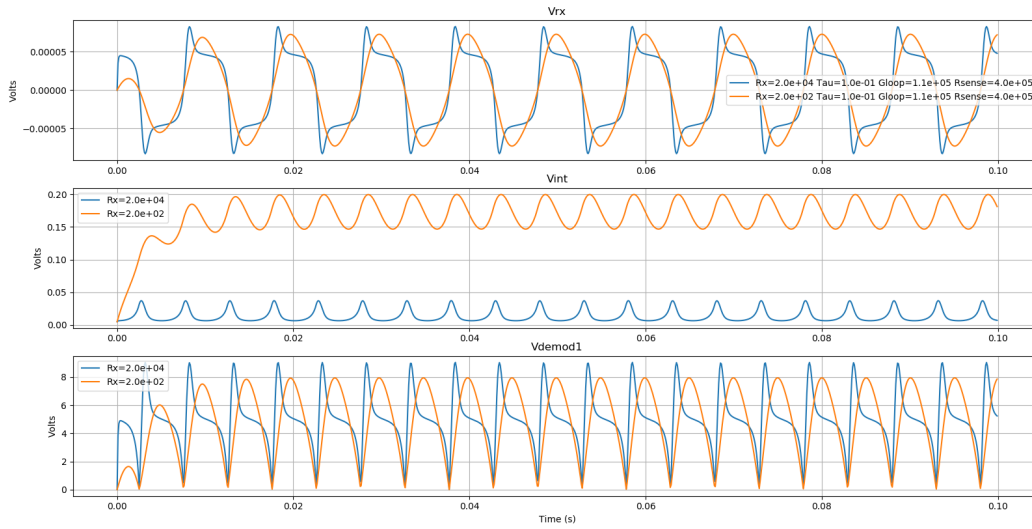


Figure 3.20: Output of Cernox servo-loop simulation.

bias across the thermistor, ‘Vint’ shows the voltage output of the integrator, and ‘Vdemod1’ shows the voltage output of the demodulator in the servo-loop. By looking at all three plots, it is easy to notice the distortion which arises in the process. A simple solution was to increase the time constant of the integrator from the original 0.1s to 10s. While increasing the time constant sacrifices bandwidth for stability, the Cernox thermistors are all read out at the slow sampling rate so this didn’t seem like a big loss. Increasing the time constant also increases the startup time of the whole circuit but since the Cernox readout circuit is always running this was not an issue. Additionally, the value of the sense resistor needed to be increased for the Flavor 2 boards from $400\text{K}\Omega$ to $1.4\text{M}\Omega$ in order to be sufficiently larger than the thermistor impedance. For all of the different flavors, the appropriate post lock-in

gain was used in order to fall within the 0V to 10V range of the AI-207 UEI card.

3.5.6 Dummy Loads

In the case of an unused Cernox daughter card channel, the open circuit acts as an extremely high impedance Cernox thermistor. The result of a high impedance load on the Cernox card causes the servo-loop to behave poorly as described in the previous section (3.5.5). Not only do the servo-loops behave poorly, but the relatively large oscillations on the bias lines cause cross-talk with adjacent (functional) Cernox bias lines. This results in beat frequencies and unwanted noise in the active lines. To remedy the situation, a dummy load is soldered directly on the daughter card. The dummy load is a resistance value within the typical operating range of a cold Cernox, usually $\sim 1K\Omega$.

In a similar fashion, on each diode daughter card channel, there are spots for dummy loads to be soldered. While the channel does not enter a disruptive state, as it does for the Cernox daughter card, the dummy loads reduce power consumption and create a well behaved circuit.

The NTD Bias cards have a tunable amplitude and should be set to a 0V bias for any unused bias channels. The NTD Lock-in cards do not require any alteration for an unused channel.

3.5.7 NTD Aliasing

In the first readout of the NTD Lock-in board through GCP, there was a $\sim 4.5\text{Hz}$ oscillation present (along with harmonics). The signal amplitude varied from channel to channel with a typical RMS of $\sim 10\text{mV}$ ($\sim 2\text{mK}$) and some of the high end RMS around $\sim 30\text{mV}$ ($\sim 25\text{mK}$). However, the signal frequency was the same for all of the channels. Upon investigation, it was determined to be an aliasing effect from the $\sim 408\text{Hz}$ AC bias being rectified and then sampled by GCP at 200Hz . Figure 3.21 shows the time ordered data as well as the PSD (in Kelvin) of one of the NTDs with the 4.5Hz and the 9Hz harmonic aliasing spike.

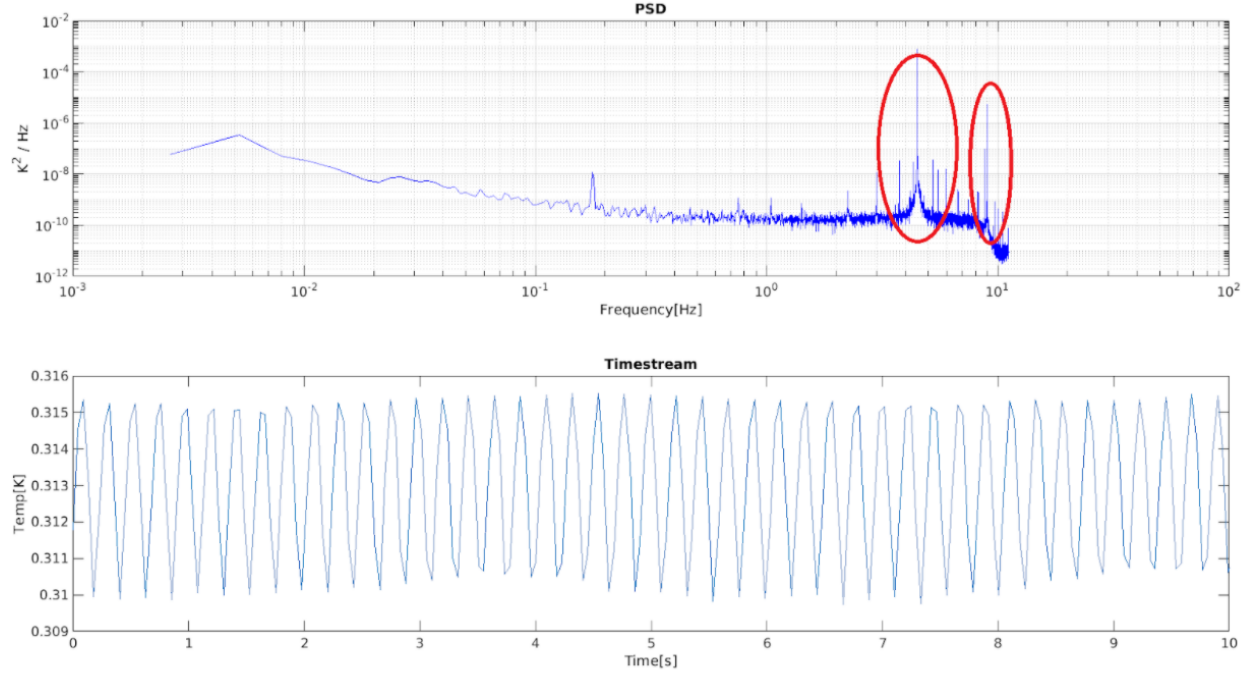


Figure 3.21: An example of the aliasing effect in the first version of the NTD Lock-in board. The 4.5Hz and the harmonic 9Hz spike are circled in the PSD.

If the inputs were properly nulled, this effect would have been minimal. However, the original design of the NTD Lock-in card did not have a DC block at the differential input from the NTD/NR bridge. This meant a slight DC offset ($\sim 1\%$ difference) in the JFET channels was creating the AC signal. There were several ways of remedying the aliasing oscillations:

1. Add a DC block on the differential input of the NTD Lock-in card.
2. Change the frequency of the NTD Oscillator card which would change the frequency of the NTD Bias.
3. Use a more sophisticated technique to down sample. This could be accomplished through GCP or through the UEI Crate.

Adding a DC block to the differential input of the NTD Lock-in card requires a slight redesign of the circuit and the PCB layout. In theory, it should not require any re-tuning of the NTD/NR bridge so the new daughter card can simply be swapped with the old daughter card. Changing the frequency of the NTD Oscillator card would only require changing a few

resistor/capacitor values on the daughter card but would be more likely to cause a need for re-tuning. The software fix would arguably be the least invasive fix but would require the most effort in writing and implementing new changes.

Even though the circuit would benefit from implementing all of these fixes, for simplicity's sake, only the 'DC block' option has been actualized. The fix is reflected in Figure 3.15 when the block diagram of the NTD Lock-in circuit was explained. To test the DC block fix, a lab setup was used where a differential input with a specified DC offset was used to reproduce the DC offset of the JFET channels. An increase in DC offset led to a higher amplitude in the aliasing oscillations. This was compared to the new version of the NTD Lock-in board with the DC block. Figure 3.22 shows a PSD (in volts) of the output of the old NTD Lock-in board (left) and the new board (right).

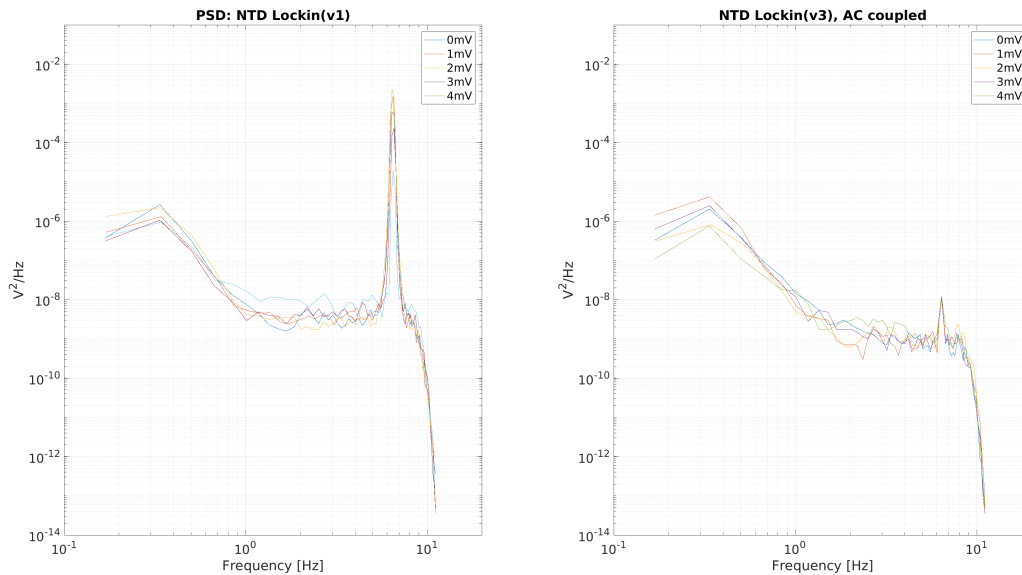


Figure 3.22: A PSD comparison of the old NTD Lock-in board (left) and the new board (right). The aliasing spike decreases by several orders of magnitude with the addition of the DC block.

Figure 3.23 shows a comparison of the old and new NTD Lock-in boards after being installed in BA1. The installation happened between the 2020 observation season and the 2021 observation season. While this fix shows significant improvement, there are still more

to be made; namely, changing the oscillation frequency of the NTD bias.

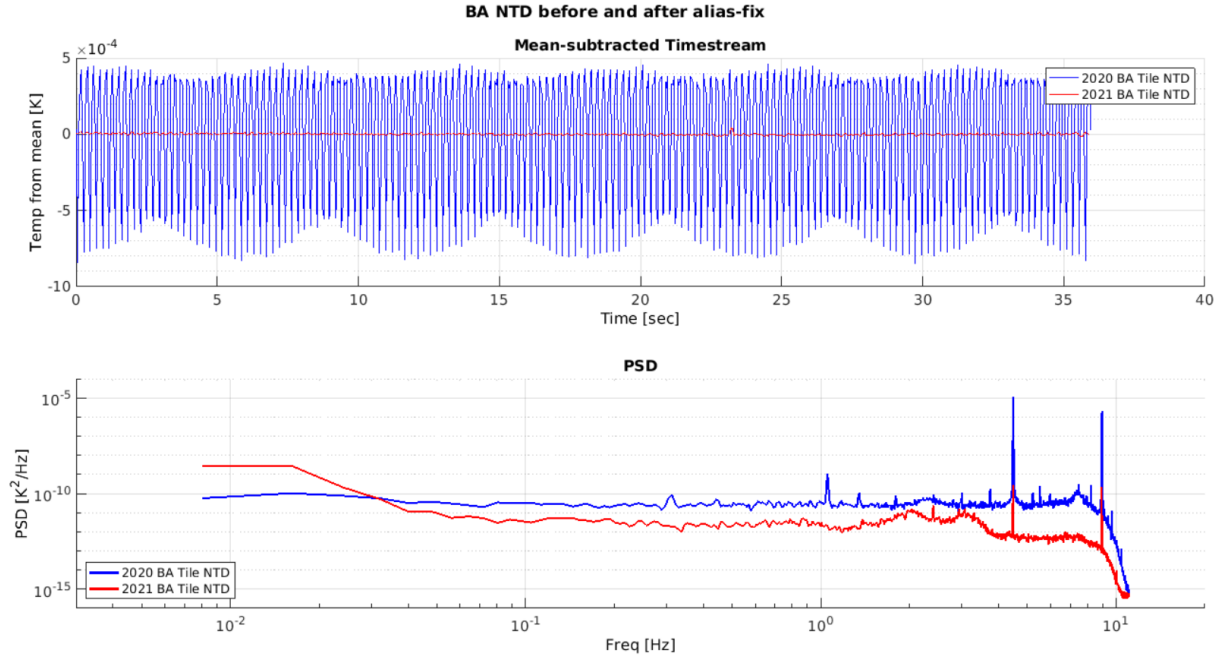


Figure 3.23: A comparison of the old NTD Lock-in board (blue) and the new board (red). The timestream plot shows several halfscans of data. The aliasing oscillations are clearly seen when using the old NTD Lock-in boards but are significantly suppressed with the new boards. In the PSD plot, the 4.5 Hz and 9 Hz spikes are decreased by several orders of magnitude with the addition of the DC block.

3.5.8 BA NTD Scan Sync

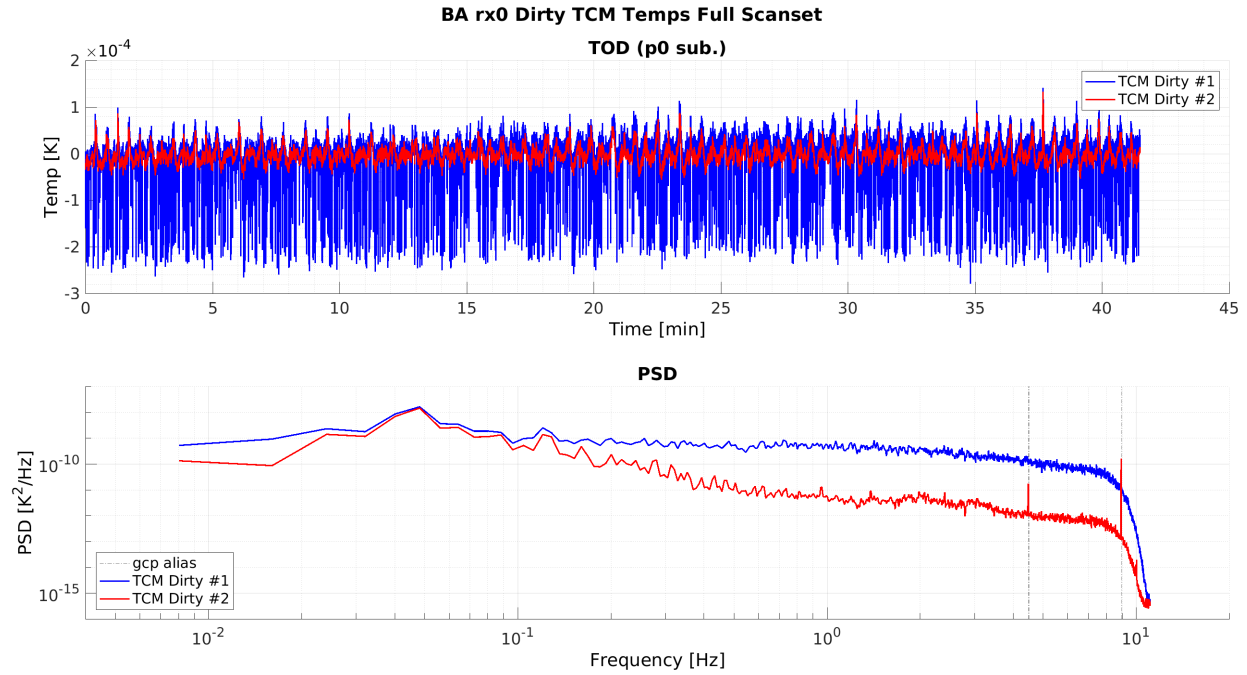
Having a stable focal plane temperature during a CMB observation is crucial. Because the receiver is constantly scanning back and forth in azimuth, we worry about temperature instabilities that are correlated with our telescope motion. By looking at the NTDs located on the temperature control (TCM) and the focal plane tiles (LRM) we are able to identify any possible problems.

Figure 3.24 shows data from a full scanset which has been subtracted by a 0th-order polynomial fit (p0 subtracted) for both the time-ordered data (TOD) and the power spectral density (PSD). The NTDs are separated into the dirty side TCM NTDs (Dirty), clean side TCM NTDs (clean), and the LRM tile NTDs (tile). The dirty side TCMs are on the fridge

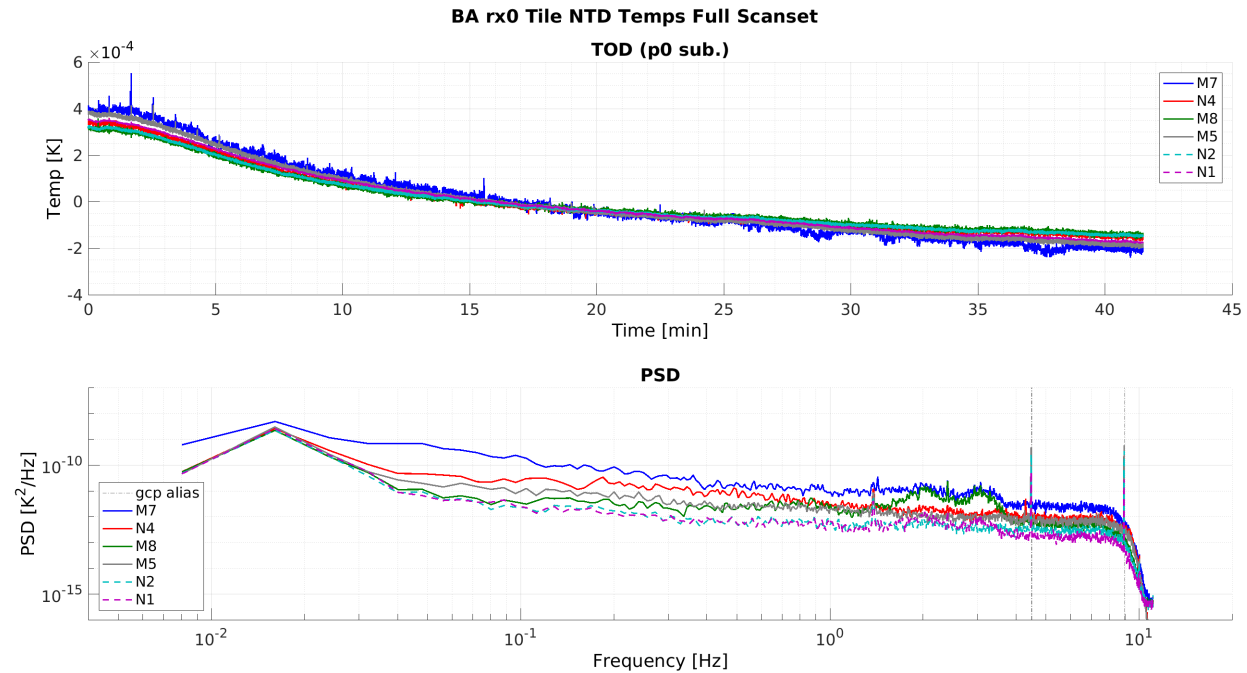
side of the thermal filter and the clean side TCMs are on the focal plane side of the thermal filter. The full scanset data includes the turnarounds between the halfscans. The scansets seem to show a scan sync signal in the dirty TCMs. A halfscan plus the turn around is ~ 26 s which will show up as $\sim 3.9 \times 10^{-2}$ Hz signal in the PSDs. However, this signal is not present in any of the clean TCMs or the tile NTDS. Because it is only on the dirty side TCMs, and we also cut the data during the turnaround, this is not a something of concern.

Figure 3.25 shows the data separated into halfscans (no turnarounds) which are further distinguished by azimuth increasing or decreasing scan directions. There were 96 halfscans (48 in each direction). Each halfscan was fit with a degree zero (p0) and degree three (p3) polynomial function (in az.) which was then subtracted. The motivation for the p3 subtraction comes from a similar p3 subtraction filter used in the detector data. For the TOD plots, all of poly-subtracted halfscans were averaged together. The PSDs show two different types of averaging. The first type, which I call ‘PSD avg./#HS’, is calculated by taking the PSD of all the individual halfscans, averaging them together, and then dividing by the number of halfscans. The second, called the ‘scanset avg.’ is calculated by averaging all of the halfscans of the same az. direction together and then taking the PSD. The ‘PSD avg./#HS’ should show signals which might be lost due to averaging together incoherent signals across halfscans. For example, there are two vertical dashed-dotted gray lines in the PSDs which are located at ~ 4.5 Hz and ~ 9 Hz. These are from readout aliasing coming from GCP and are not real signals. In the ‘scanset avg.’ PSDs these signals tend to average to zero and are not seen to the same extent.

Because of the large amount information and number of plot variations, I have only shown one tile NTD (M8) as an example. By looking at the TODs and PSDs, we can see that the focal plane temperature does not show any signs of scan sync behavior in either direction of the halfscans. Also reassuring is the flat shape of the PSD at frequencies below the cut-off frequency of the low-pass filter.

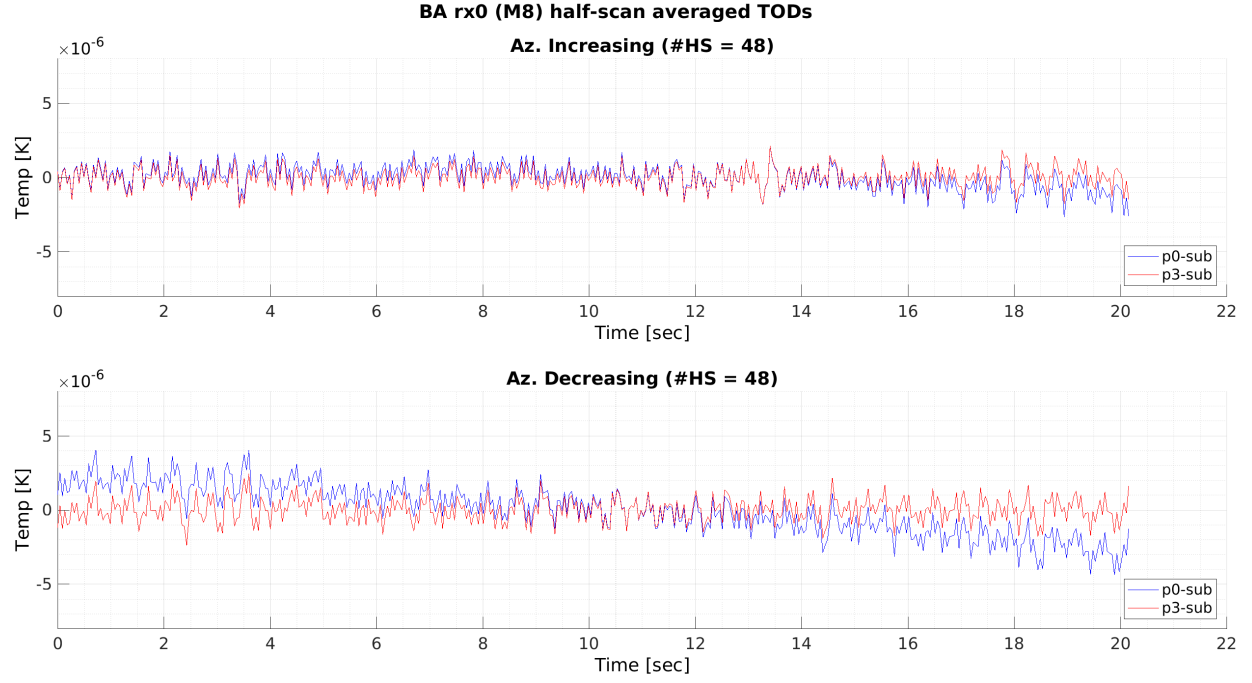


(a) Dirty side TCM NTD temperatures during a full scanset. TCM #1 is much noisier and therefore, TCM #2 is used for temperature control.

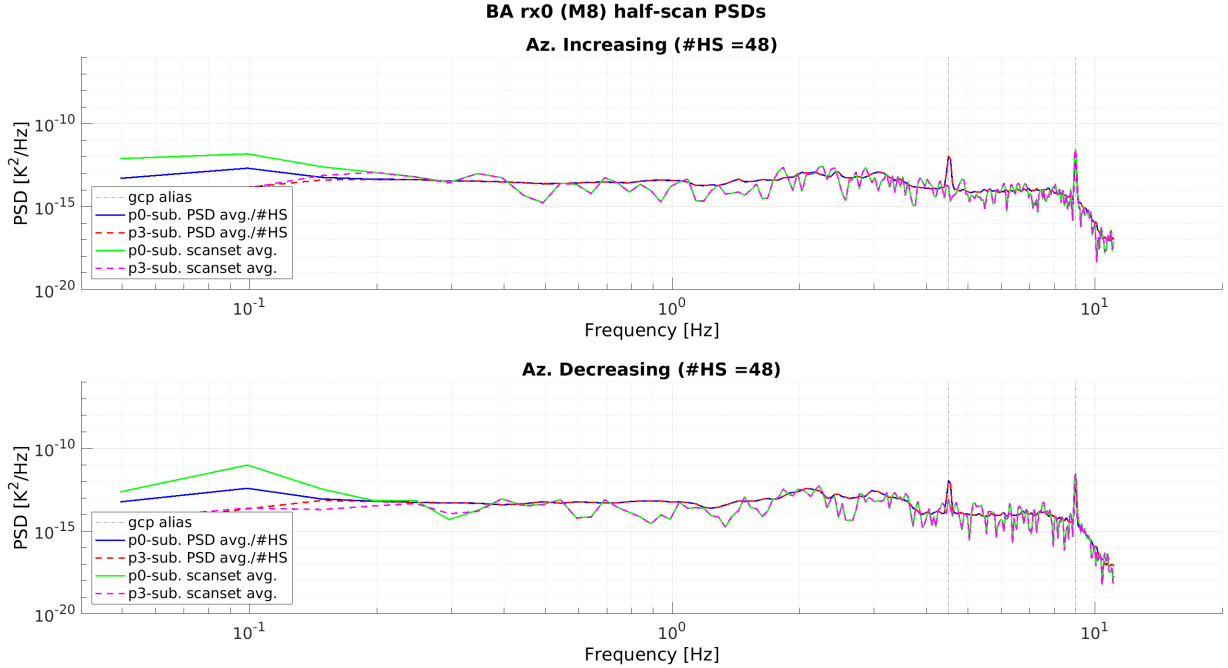


(b) Tile NTD temperatures during a full scanset. The various colors are the different tiles.

Figure 3.24: BA NTD full scanset temperature TODs and PSDs. Notice the bump in the dirty side TCM PSDs around $\sim 4 \times 10^{-2}$ Hz which is the scan sync signal. This is not present in the tile NTDs. The two vertical gray lines in the PSDs are an aliasing signal from the GCP readout.



(a) Average of 48 halfscans in the TOD.



(b) Two types of halfscan averages in the PSD.

Figure 3.25: NTD focal plane temperature of tile M8. These plots look at averages of halfscans over a full scanset (~ 50 min). They are also separated into the two azimuth scan directions, increasing and decreasing. The ‘p0’ subtracts off a 0th order poly fit and the ‘p3’ subtracts off a 3rd order poly fit.

Chapter 4

Multi-component Data Analysis

This chapter is a look at high level data analysis using the BICEP/Keck Collaboration data. We start with the data in the form of bandpowers which was its form at the end of Chapter 2 (Section 2.4.2). Because the noise and the signals of the CMB are described by Gaussian random variables, all of the relevant information of the maps can be expressed in the form of bandpowers [67]. In other words, instead of using the pixelized data directly, we use the data in the form of the bandpowers in order to significantly compress the data while losing none of the relevant information. This intermediate step of putting the data in the form of bandpowers also makes cross-collaboration data sharing easier as well as maximum likelihood searches for cosmological parameters. A detailed description of how Gaussian random variables relate to the bandpowers can be found in Appendix A of Victor Buza's PhD thesis [68].

Our collaboration uses a multi-component model to calculate the contributions of CMB and foreground signals to the bandpowers. The uncertainty of our bandpowers is expressed in the form of a covariance matrix which we refer to as a bandpower covariance matrix (BPCM). Using the bandpowers, the multi-component model, and the BPCM, we perform maximum likelihood (ML) searches to estimate the cosmological parameter r as well as the nuisance foreground parameters. Section 4.1 gives a description of the parameters and multi-

component model used in our pipeline. Section 4.2 looks at the BPCM and a method for improving the scaling. Section 4.3 looks at variations in the construction of the BPCM and whether they cause a bias on r from the ML search. Section 4.4 looks at a novel minimum variance quadratic estimator which is an alternative to the ML search. And lastly, Section 4.5 uses the method of the quadratic estimator to look at systematic biases on r for the future CMB-S4 experiment.

Because of the annual cycle and cumulative nature of our data, our collaboration has naming conventions of datasets based on the years they were accumulated. The default dataset used throughout this chapter is referred to as BK15. Here, the ‘BK’ stands for BICEP/Keck and the ‘15’ stands for the data years up to and including 2015. Additionally, the BK18lf¹ dataset will be used although the real data will be omitted due to the fact that it is not yet published.

Our datasets include data in the form of maps from five different instruments: BICEP2, Keck Array, BICEP3, WMAP, and Planck². We denote the maps by both the instrument used and the observing frequency. So, for some examples, the BICEP/Keck map up to and including 2015 data observed with a 220 GHz receiver is referred to as BK15_220, the Planck map observed at 100 GHz is referred to as P100 and the WMAP map observed at 33 GHz is referred to as W033. Because a bandpower is the combination of two maps, our bandpowers are then distinguished by their two constituent maps (i.e., $BK15_220 \times W033$). If the map is multiplied by itself, it is referred to as an auto-spectrum; if the map is multiplied by a different map, it is referred to as a cross-spectrum. The operation of multiplying maps together is commutative.

¹The ‘lf’ denotes the large field dataset. This means we use the larger BICEP3 field coverage when possible and use the smaller Keck Array field coverage in other cases.

²WMAP [42] and Planck [11] were satellite experiments which measured a full sky map of the CMB.

4.1 Multi-component Model

The content of this chapter relies heavily on the use of bandpower expectation values (exp-vals) which are theoretical values of the bandpowers created from a multi-component model. Our multi-component parameterized model contains the tensor-to-scalar ratio, r , as well as many nuisance parameters from foregrounds. The following is a list of the parameters used in our model³:

- r : The cosmological parameter of the tensor-to-scalar ratio.
- A_d : The amplitude of polarized galactic dust [μK^2].
- A_s : The amplitude of synchrotron radiation that comes from our galaxy [μK^2].
- β_d : The spectral index scaling parameter used to describe how the polarized galactic dust scales with frequency. Dust scales as a graybody (Section 1.4.1).
- β_s : The spectral index scaling parameter used to describe how the synchrotron radiation scales with frequency. Sync has a power law scaling (Section 1.4.2).
- α_d : The power law scaling parameter used to describe how the polarized galactic dust scales with multipole ℓ .
- α_s : The power law scaling parameter used to describe how the synchrotron radiation scales with multipole ℓ .
- ϵ : The parameter used to describe the level of correlation between polarized dust and synchrotron radiation, $-1 \leq \epsilon \leq 1$.
- A_L : The lensing amplitude of Λ CDM ($A_L = 1$ is standard lensing).
- T_d : Temperature of the dust blackbody. $T_d = 19.6K$ is used for most of our applications.
- EB_d : EE -to- BB ratio for dust. $EB_d = 2$ is used for most of our applications.
- EB_s : EE -to- BB ratio for sync. $EB_s = 2$ is used for most of our applications.
- Δ'_d : Dust decorrelation parameter. This parameter suppresses dust power in the cross-spectra due to spatial variations of dust with respect to frequency (does not affect the

³We define the power spectra in our model using the following scaled version $D_\ell = \ell(\ell + 1)C_\ell/2\pi$.

auto-spectra). A dust decorrelation of $\Delta'_d = 1$ means the dust is perfectly correlated across frequencies and is used for most of our applications.

- Δ'_s : Sync decorrelation parameter. This parameter suppresses sync power in the cross-spectra due to spatial variations of sync with respect to frequency (does not affect the auto-spectra). A sync decorrelation of $\Delta'_s = 1$ means the sync is perfectly correlated across frequencies and is used for most of our applications.

In practice, some of these parameters are held fixed in our analysis. We hold the decorrelation fixed at $\Delta'_d = \Delta'_s = 1$ because we find no evidence of decorrelation in our data given the current noise levels [37]. The EE -to- BB ratios for both sync and dust are both at two, $EB_d = EB_s = 2$ [11] [69]. Because we do not currently apply an sort of delensing, we can hold the lensing amplitude fixed at $A_L = 1$ for standard Λ CDM lensing. As described previously in Section 1.4.1, the spectral energy distribution (SED) model used for dust is a modified blackbody (graybody). This is a blackbody with fixed temperature $T_d = 19.6K$ multiplied by a power law and spectral index β_d [70]. The SED model of sync (described in Section 1.4.2) is a power law with a spectral index of β_s .

The multi-component model can be used to quickly calculate theoretical bandpowers with various levels of r and foreground components. The multi-component parameters will be used throughout the chapter but especially in relation to the maximum likelihood search (Section 4.3) and the quadratic estimator (Section 4.4). The multi-component model for the foreground component of BB is expressed as [37]:

$$D_{\ell}^{\nu_1 \times \nu_2} = A_d \Delta'_d f_d^{\nu_1} f_d^{\nu_2} \left(\frac{\ell}{80} \right)^{\alpha_d} + A_s \Delta'_s f_s^{\nu_1} f_s^{\nu_2} \left(\frac{\ell}{80} \right)^{\alpha_s} + \epsilon \sqrt{A_d A_s} (f_d^{\nu_1} f_s^{\nu_2} + f_s^{\nu_1} f_d^{\nu_2}) \left(\frac{\ell}{80} \right)^{(\alpha_d + \alpha_s)/2} \quad (4.1)$$

Where ν_1 and ν_2 are the observing frequencies of the two maps and $\ell = 80$ is used as the pivot for ℓ . Here f_d^{ν} and f_s^{ν} are the scaling functions of dust and sync, respectively, given the observing frequency. They are scaled in relation to a pivot frequency which we typically use

as f_d^{353GHz} and f_s^{23GHz} .

We can add the foreground model to the model for the CMB contribution. Our model for CMB comes from both the r and the lensed E -modes:

$$D_\ell^{\nu_1 \times \nu_2} = \frac{r}{0.1} D_\ell^{tensor} + A_L D_\ell^{lensing} \quad (4.2)$$

Where D_ℓ^{tensor} is the tensor signal produced with an $r = 0.1$ and $D_\ell^{lensing}$ is the signal produced by the lensed E -modes.

4.2 Bandpower Covariance Matrix

The bandpowers, described in Section 2.4.2, are a culmination of all of the data put into our analysis pipeline. While it is possible to use any combination of two CMB fields (TT , EE , BB , TE , TB , and EB), this chapter will focus on the BB bandpowers unless otherwise stated. The bandpower covariance matrix (BPCM) describes the uncertainties in our measurements by using simulations of bandpowers. This section describes how the BPCM is conditioned and also a method for improving the BPCM scaling in our analysis pipeline.

4.2.1 Bandpower Covariance Matrix Conditioning

The most straight forward way to calculate the BPCM is to simply compute the sample covariance of our CMB+foregrounds+noise sim realizations. In our BK15 analysis, we use $m = 12$ maps from different experiments which in turn means $m(m+1)/2 = 78$ BB spectra. This is then multiplied by the number of ℓ -bins (9) which gives a 702×702 BPCM⁴. Because the BPCM is made from only 499 sim realizations, the matrix is singular and un-invertible (which is a problem in our likelihood calculation). This problem can be remedied by conditioning the matrix from our knowledge of the experiments.

⁴a similar amount is used for BK18lf

One of the ways we condition the BPCM is to set the covariance between bandpowers which are more than one ℓ -bin apart to zero. Given our ℓ -bin width ($\Delta\ell \sim 35$), we know there will be some correlation between adjacent ℓ -bins ($\sim 10\%$). However, we don't expect any spatial correlation of bandpowers past one ℓ -bin. So in the limit of infinite sims, the covariance between bandpowers more than one ℓ -bin apart should be zero. In reality, these covariance are non-zero because of simulation error so we set them to zero. Our BPCM is organized into 'blocks' of bandpowers which share the same ℓ -bin. A simple mask is applied to the BPCM where entries which are more than one ℓ -bin 'block' apart are set to zero. In block matrix form, the BPCM (\mathbb{C}) and the mask (\mathbb{M}) look like:

$$\mathbb{C} = \begin{bmatrix} C_{1 \times 1} & C_{1 \times 2} & C_{1 \times 3} & \cdots & C_{1 \times y} \\ C_{2 \times 1} & C_{2 \times 2} & C_{2 \times 3} & \cdots & C_{2 \times y} \\ C_{3 \times 1} & C_{3 \times 2} & C_{3 \times 3} & \cdots & C_{3 \times y} \\ \vdots & \vdots & \vdots & \ddots & \vdots \\ C_{x \times 1} & C_{x \times 2} & C_{x \times 3} & \cdots & C_{9 \times 9} \end{bmatrix} \quad (4.3)$$

$$\mathbb{M} = \begin{bmatrix} \mathbb{J} & \mathbb{J} & \emptyset & \cdots & \emptyset \\ \mathbb{J} & \mathbb{J} & \mathbb{J} & \cdots & \emptyset \\ \emptyset & \mathbb{J} & \mathbb{J} & \cdots & \emptyset \\ \vdots & \vdots & \vdots & \ddots & \vdots \\ \emptyset & \emptyset & \emptyset & \cdots & \mathbb{J} \end{bmatrix} \quad (4.4)$$

Where $C_{x \times y}$ indicates the covariance between the bandpowers of ℓ -bin x with the bandpowers of ℓ -bin y , \mathbb{M} is the mask, \mathbb{J} is a matrix of ones, and \emptyset is a matrix of zeros. We can then apply the conditioning by taking the element-by-element product; $\mathbb{M} \circ \mathbb{C}$.

Another way we condition the BPCM is to assume that the signals in the maps are independent of the noise. If we look at one entry in the BPCM, we can write the most general case in terms of four maps (m_a , m_b , m_c and m_d) where each map is comprised of

signal and noise, e.g., $m_a = s_a + n_a$. The covariance of two bandpowers can be written as $Cov\{m_a \times m_b, m_c \times m_d\}$ where \times indicates taking the angular power spectrum between the two maps. If we expand the terms we get an expression with 16 covariance terms:

$$Cov\{(s_a + n_a) \times (s_b + n_b), (s_c + n_c) \times (s_d + n_d)\} = Cov\{s_a \times s_b, s_c \times s_d\} + \\ Cov\{s_a \times s_b, s_c \times n_d\} + Cov\{s_a \times s_b, n_c \times s_d\} + \dots \quad (4.5)$$

After the expansion, any covariance term which takes a signal-only map cross a noise-only map as at least one of spectra (e.g. $Cov\{s_a \times s_b, s_c \times n_d\}$) or takes the covariance between a signal-only spectra with a noise-only spectra (e.g. $Cov\{s_a \times s_b, n_c \times n_d\}$) can be assumed to be zero. This removes 10 terms total: 4 terms which contain three signal-only maps and one noise-only map (e.g., $Cov\{s_a \times s_b, s_c \times n_d\}$), 4 terms which contain one signal-only map and three noise-only maps (e.g., $Cov\{s_a \times n_b, n_c \times n_d\}$), and 2 terms which are the covariance between signal-only spectra and noise-only spectra ($Cov\{s_a \times s_b, n_c \times n_d\}$ and $Cov\{n_a \times n_b, s_c \times s_d\}$). The 6 remaining terms are described as:

- **signal-only (sig):** $Cov\{s_a \times s_b, s_c \times s_d\} = \mathbb{C}_{sig}$
- **noise-only (noi):** $Cov\{n_a \times n_b, n_c \times n_d\} = \mathbb{C}_{noi}$
- **signal×noise term 1 (sn1):** $Cov\{s_a \times n_b, s_c \times n_d\} = \mathbb{C}_{sn1}$
- **signal×noise term 2 (sn2):** $Cov\{s_a \times n_b, n_c \times s_d\} = \mathbb{C}_{sn2}$
- **signal×noise term 3 (sn3):** $Cov\{n_a \times s_b, s_c \times n_d\} = \mathbb{C}_{sn3}$
- **signal×noise term 4 (sn4):** $Cov\{n_a \times s_b, n_c \times s_d\} = \mathbb{C}_{sn4}$

These terms can be added together to give the BPCM:

$$\mathbb{C} = \mathbb{C}_{sig} + \mathbb{C}_{noi} + \mathbb{C}_{sn1} + \mathbb{C}_{sn2} + \mathbb{C}_{sn3} + \mathbb{C}_{sn4} \quad (4.6)$$

This conditioning becomes more complicated when we consider multiple types of signals (CMB, dust, synchrotron) and that they are uncorrelated with each other, e.g., dust and CMB signal are independent of each other. The more complicated conditioning and scaling

is discussed more in the next section (4.2.2).

The last type of conditioning we apply is with the noise correlation between different ‘experiments’. The noise correlation between bandpowers made of two different experiments is set to zero to reflect the fact that the noise is uncorrelated among the different experiments. To implement this conditioning, we apply six different masks to the six different covariance terms above which zeros out the noise correlation terms. The masks are matrices consisting of entries of ones (no conditioning) and zeros. For \mathbb{C}_{sig} the mask is simply a matrix of ones (i.e., no mask) because there are no noise terms. For \mathbb{C}_{noi} , the mask is zero for all of the entries except for the diagonals of each ℓ block (i.e., everything except the auto-spectra are zeroed). For the four signal-noise terms (\mathbb{C}_{sn1} , \mathbb{C}_{sn2} , \mathbb{C}_{sn3} , and \mathbb{C}_{sn4}), the masks are a more complicated structure and are all different from each other. The masks of a single ℓ block (78×78) for the BK15 signal-noise terms can be seen in Figure 4.1. The effects of this conditioning on our maximum likelihood search is demonstrated in Section 4.3.4.

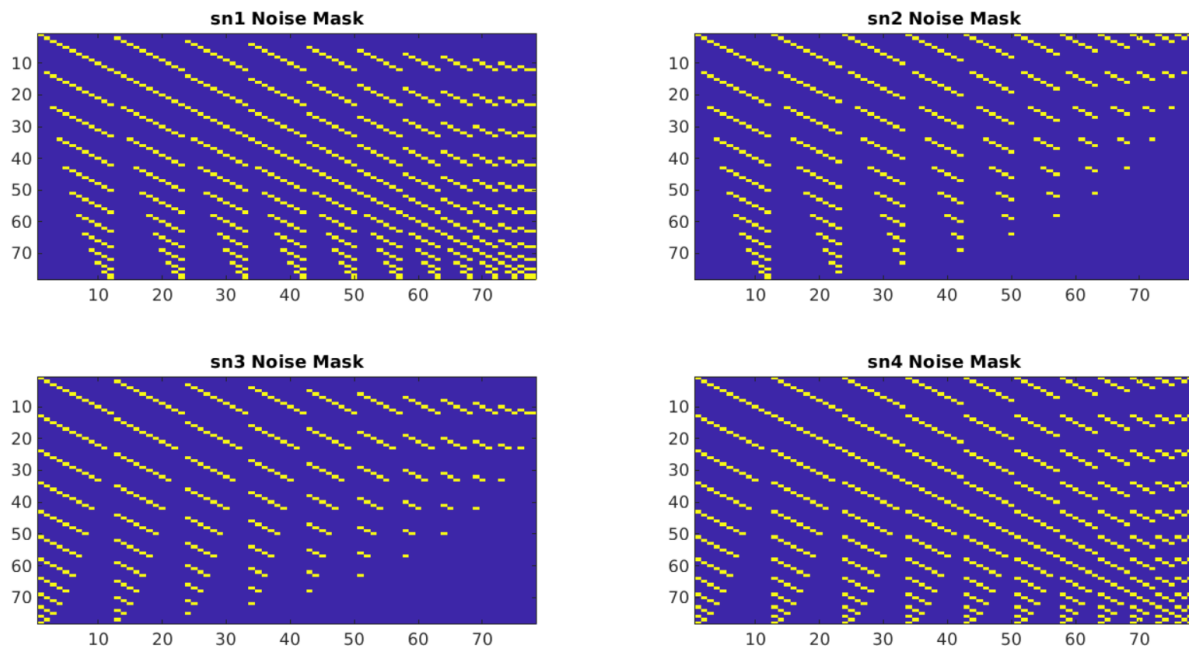


Figure 4.1: BPCM noise correlation masks for signal-noise terms. The blue matrix entries are zeroes and the yellow entries are ones.

4.2.2 BPCM Scaling

Often in the collaboration we want to test different types of models which have different levels of CMB and foreground signals. Because the BPCM is made from the 499 sim realizations, we would need to generate new sims for every time we want a model with different parameter values. This is time consuming and a large use of computing resources. Instead, we use a method for scaling the BPCM using our multi-component model. In our current analysis pipeline, the BPCM scaling uses a sub-function referred to as `model_rms()`. This sub-function scales the uncorrelated signal fields of the maps separately using the square root of the bandpower expectation values, thus ‘RMS’. While this method works, it is cumbersome and, more importantly, it creates a divergence in our analysis pipeline. Presented in this subsection is the formalism of the `model_rms()` construction as well as a new method which scales the BPCM with just the bandpower expectation values (`expvals`). This new method presents a more elegant solution and offers a more coherent, consistent, and flexible extension of our pipeline.

Model RMS

As stated in Section 4.2.1, part of the conditioning of the BPCM is to separate the signal and the noise. While our multi-component model already has a specific scaling of the fields in terms of bandpowers, the `model_rms()` uses a different set of fields in terms of the maps. This is a somewhat convoluted way of applying scaling which is why there will be a suggested improvement in the next subsection (4.2.2). With `model_rms()` we use a set of five independent signal fields plus noise in the maps. These fields are as follows:

1. lensed Λ CDM CMB component
2. uncorrelated synchrotron component
3. uncorrelated dust component
4. correlated synchrotron+dust component
5. tensor CMB component

So with these independent fields, we express a map as:

$$m_a = \sum_i a_i + n_a \quad (4.7)$$

Where m_a is the map, n_a is the noise of the map, a_i are the independent signals, and the subscript indicates the type of signal field listed above. This will be demonstrated for the most general case which contains four different maps (m_a , m_b , m_c , and m_d). It will also be useful to include some more notation and identities. A bandpower expectation value will be represented with $\langle \rangle$ which means an auto-spectra bandpower expval will look like:

$$\langle m_a \times m_a \rangle = \langle m_a^2 \rangle = \sum_i \langle a_i^2 \rangle + \langle n_a^2 \rangle \quad (4.8)$$

A cross-spectra bandpower expval will look like:

$$\langle m_a \times m_b \rangle = \langle m_b \times m_a \rangle = \sum_i \langle a_i b_i \rangle = \sum_i (\langle a_i^2 \rangle \langle b_i^2 \rangle)^{\frac{1}{2}} \quad (4.9)$$

Where the right hand side of the equation invokes the following identity:

$$\langle a_i b_i \rangle = (\langle a_i^2 \rangle \langle b_i^2 \rangle)^{\frac{1}{2}} \quad (4.10)$$

This identity expresses that the signal from two maps are fully correlated, which is true by design for signals with the same index. For the uncorrelated signal types, the following is true: $\langle a_i a_j \rangle = \langle a_i b_j \rangle = 0$. In the case of the auto-spectra, the noise between the maps is obviously correlated which is why the noise term ($\langle n_a^2 \rangle$) is still present. In the case of the cross-spectra, the noise between the maps is uncorrelated so the expval of the noise term will be zero, $\langle n_a n_b \rangle = 0$. It is common then to express the expval of the auto-spectra as a noise-debiased bandpower expval ($\langle m_a \times m_a \rangle \rightarrow \langle m_a \times m_a \rangle - \langle n_a^2 \rangle$). So for the remaining of the chapter this will be the case. Lastly, the simulations used to create the fiducial BPCM

will be denoted with a naught subscript; e.g., the simulation for m_a will be expressed as a_0 .

In the RMS scaling, the different terms of the BPCM in Equation 4.6 are scaled separately. The scaling of the BPCM for the most generic matrix element with four different maps is:

$$\begin{aligned} Cov\{m_a \times m_b, m_c \times m_d\} = & (\gamma_{sig1} + \gamma_{sig2} + \gamma_{sig3})\mathbb{C}_{sig} + \\ & \gamma_{sn1}\mathbb{C}_{sn1} + \gamma_{sn2}\mathbb{C}_{sn2} + \gamma_{sn3}\mathbb{C}_{sn3} + \gamma_{sn4}\mathbb{C}_{sn4} + \mathbb{C}_{noi} \end{aligned} \quad (4.11)$$

Where the γ terms are the scaling coefficients when we want to use bandpower expectation values with signals which deviate from our fiducial model. Two things worth noting; (1) the signal scaling coefficient is separated into three terms and (2) the noise term doesn't scale ($\gamma_{noi} = 1$). The scaling terms are:

$$\gamma_{sig1} = \sum_i \left[\frac{\langle a_i^2 \rangle \langle b_i^2 \rangle \langle c_i^2 \rangle \langle d_i^2 \rangle}{\langle a_0^2 \rangle \langle b_0^2 \rangle \langle c_0^2 \rangle \langle d_0^2 \rangle} \right]^{\frac{1}{2}} \quad (4.12)$$

$$\gamma_{sig2} = \frac{1}{2} \sum_i \sum_{j \neq i} \left[\frac{\langle a_i^2 \rangle \langle b_j^2 \rangle \langle c_i^2 \rangle \langle d_j^2 \rangle}{\langle a_0^2 \rangle \langle b_0^2 \rangle \langle c_0^2 \rangle \langle d_0^2 \rangle} \right]^{\frac{1}{2}} \quad (4.13)$$

$$\gamma_{sig3} = \frac{1}{2} \sum_i \sum_{j \neq i} \left[\frac{\langle a_i^2 \rangle \langle b_j^2 \rangle \langle c_j^2 \rangle \langle d_i^2 \rangle}{\langle a_0^2 \rangle \langle b_0^2 \rangle \langle c_0^2 \rangle \langle d_0^2 \rangle} \right]^{\frac{1}{2}} \quad (4.14)$$

$$\gamma_{sn1} = \sum_i \left[\frac{\langle a_i^2 \rangle \langle c_i^2 \rangle}{\langle a_0^2 \rangle \langle c_0^2 \rangle} \right]^{\frac{1}{2}} \quad (4.15)$$

$$\gamma_{sn2} = \sum_i \left[\frac{\langle a_i^2 \rangle \langle d_i^2 \rangle}{\langle a_0^2 \rangle \langle d_0^2 \rangle} \right]^{\frac{1}{2}} \quad (4.16)$$

$$\gamma_{sn3} = \sum_i \left[\frac{\langle b_i^2 \rangle \langle c_i^2 \rangle}{\langle b_0^2 \rangle \langle c_0^2 \rangle} \right]^{\frac{1}{2}} \quad (4.17)$$

$$\gamma_{sn4} = \sum_i \left[\frac{\langle b_i^2 \rangle \langle d_i^2 \rangle}{\langle b_0^2 \rangle \langle d_0^2 \rangle} \right]^{\frac{1}{2}} \quad (4.18)$$

Where the indices i and j express the independent signal fields listed earlier. In this way, we are able to scale the 6 components of the BPCM discussed in Equation 4.6 separately. The advantage of using a scaling method is that we are able to use models with various

parameter values without having to regenerate costly simulations every time. These scaling terms, made with the `model_rms()` sub-function, are the current standard in our pipeline for scaling the BPCM.

Bandpower Expectation Value Scaling

Instead of using the sum of the separate signal types, it is possible to use the bandpower expvals for the scaling coefficients. Looking first at the *sig* scaling terms, we can combine them into one term: $\gamma_{sig} = \gamma_{sig1} + \gamma_{sig2} + \gamma_{sig3}$. Next, we can rearrange the terms and combine the sums so it becomes:

$$\gamma_{sig} = \frac{1}{2} \left[\sum_i \sum_j \left(\frac{\langle a_i^2 \rangle \langle b_j^2 \rangle \langle c_i^2 \rangle \langle d_j^2 \rangle}{\langle a_0^2 \rangle \langle b_0^2 \rangle \langle c_0^2 \rangle \langle d_0^2 \rangle} \right)^{\frac{1}{2}} + \sum_i \sum_j \left(\frac{\langle a_i^2 \rangle \langle b_j^2 \rangle \langle c_j^2 \rangle \langle d_i^2 \rangle}{\langle a_0^2 \rangle \langle b_0^2 \rangle \langle c_0^2 \rangle \langle d_0^2 \rangle} \right)^{\frac{1}{2}} \right] \quad (4.19)$$

Lastly, we invoke the identity in Equation 4.10 and express it in terms of bandpower expvals:

$$\gamma_{sig} = \frac{1}{2} \left[\frac{\langle m_a \times m_c \rangle \langle m_b \times m_d \rangle}{\langle a_0 \times c_0 \rangle \langle b_0 \times d_0 \rangle} + \frac{\langle m_a \times m_d \rangle \langle m_b \times m_c \rangle}{\langle a_0 \times d_0 \rangle \langle b_0 \times c_0 \rangle} \right] \quad (4.20)$$

In a similar manner, we can express the signal-noise scaling terms with bandpower expvals:

$$\gamma_{sn1} = \frac{\langle m_a \times m_c \rangle}{\langle a_0 \times c_0 \rangle} \quad (4.21)$$

$$\gamma_{sn2} = \frac{\langle m_a \times m_d \rangle}{\langle a_0 \times d_0 \rangle} \quad (4.22)$$

$$\gamma_{sn3} = \frac{\langle m_b \times m_c \rangle}{\langle b_0 \times c_0 \rangle} \quad (4.23)$$

$$\gamma_{sn4} = \frac{\langle m_b \times m_d \rangle}{\langle b_0 \times d_0 \rangle} \quad (4.24)$$

In this way, we have now expressed the BPCM scaling in terms of the bandpower expvals instead of using the `model_rms()` sub-function.

The two ways we tested this new method of BPCM scaling were: (1) Is it self consistent? and (2) How does it compare to the original scaling? In testing the self consistency of the

the scaling, we looked at two different models used to scale the BPCM. The first model was simple and contained only CMB signal + noise. The second model was the same except the amount of CMB signal was doubled, $2 \times \text{CMB signal} + \text{noise}$. Because we are dealing with power spectra, we would expect the doubling of the CMB signal to cause a factor of 4 increase in the scaling matrix. The final step was to take an element-by-element ratio of the signal-only scaling matrix of the two different models, $\gamma_{sig}^{(2)}/\gamma_{sig}^{(1)}$. The result was a ratio matrix with every element equal to 4 which is what we would expect from a self consistent scaling model.

The next test was to do a comparison between the old RMS scaling method with the new bandpower expval scaling. In this test, we simply took the fractional difference between the new scaling term and old scaling term for each BPCM component. Figure 4.2 shows a few representative plots of this process. On the top row is the signal-only scaling term (where we expect the largest deviation). On the bottom row is the *sn1* scaling term which should be similar to all of the other signal-noise terms. Because the noise-only term doesn't scale, we expect it to be the same. As can be seen in the figure, there is slight deviation from the original scaling but the fractional difference is similar. Most of the fractional differences are binned at 0% with the large majority binned at $<2\%$. There are a few outliers which extend up to $\sim 4\%$.

In order to implement this type of scaling into our pipeline, there is a complication in dealing with the off-diagonal ℓ -bin blocks. Our analysis framework of bandpower expvals does not allow for the calculation of bandpowers expvals from maps at different ℓ -bins, e.g., $\langle m_a^{\ell=2} \times m_b^{\ell=3} \rangle$. There is currently an untested fix for this but still needs to be investigated.

4.3 Maximum Likelihood Search

With our data in the form of bandpowers, our uncertainty in the form of the BPCM (Section 4.2), and our parameters from the multi-component model (Section 4.1), we are now able to

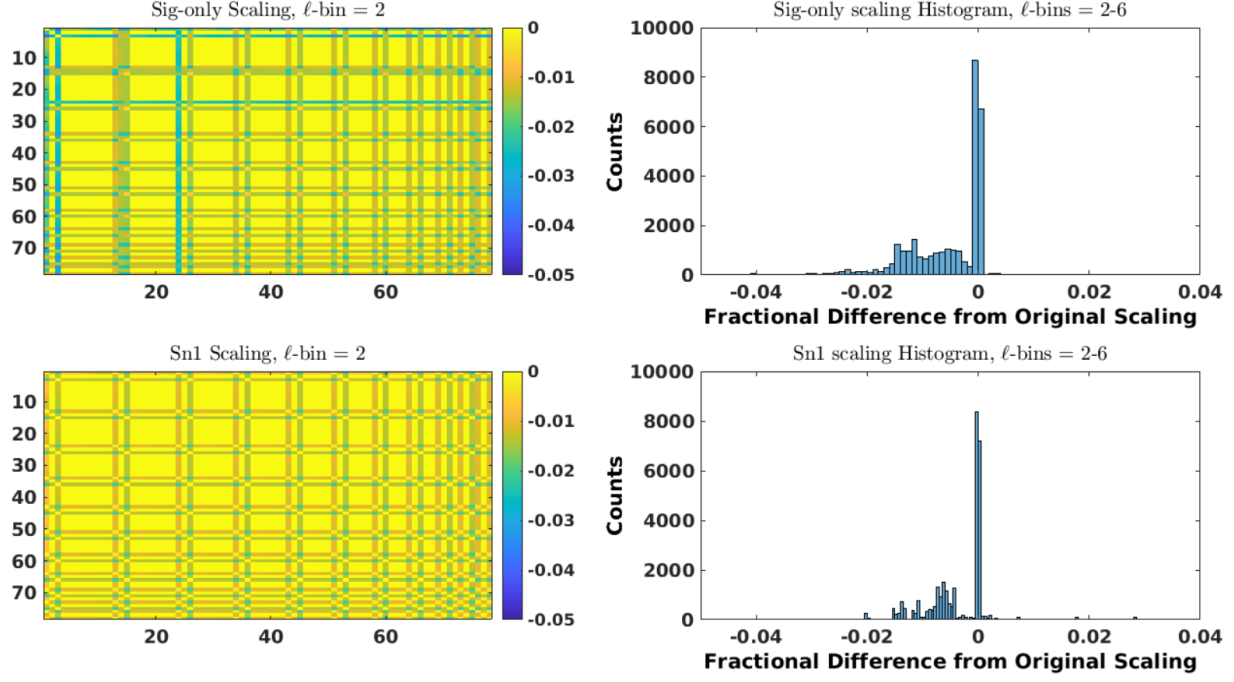


Figure 4.2: Fractional difference of the scaling terms between different methods. The old method used RMS and the new method uses bandpower expvals. The top row shows the signal-only scaling term and the bottom row shows the $sn1$ term. On the left is one ℓ -bin represented in matrix form where the color scale is in fractional difference. On the right is a histogram of the fractional difference from all the matrix elements from the first 5 ℓ -bins. The histogram does not include any off-diagonal ℓ -bin blocks.

make a maximum likelihood (ML) estimation of r as well as the other nuisance foreground parameters. Essentially, the ML estimate calculates the values of the parameters for which the data (bandpowers) have the largest probability. Because we are using partial sky data and we are using the lower ℓ -bins (i.e., less degrees of freedom), we are not able to use a Gaussian likelihood approximation. Instead, we use a Hamimeche-Lewis (H-L) likelihood approximation [71]. This approximation allows us to reliably calculate our parameters from bandpowers while using partial sky data at lower ℓ . The H-L log likelihood approximation looks like:

$$-2\mathcal{L}(\{\mathcal{C}_\ell\}|\{\hat{\mathcal{C}}_\ell\}) \approx \sum_{\ell\ell'} [\mathbf{X}_g]_\ell^T [\mathbf{M}_f^{-1}]_{\ell\ell'} [\mathbf{X}_g]_{\ell'} \quad (4.25)$$

Where here \mathcal{C}_ℓ are the bandpowers of the model being tested, $\hat{\mathcal{C}}_\ell$ are the data bandpowers, \mathbf{M}_f is the BPCM for some fiducial model, and \mathbf{X} is an expression of the bandpowers as:

$$[\mathbf{X}_g]_\ell = \text{vecp} \left(\mathcal{C}_{f\ell}^{1/2} \mathbf{g} \left[\mathcal{C}_\ell^{-1/2} \hat{\mathcal{C}}_\ell \mathcal{C}_\ell^{-1/2} \right] \mathcal{C}_{f\ell}^{1/2} \right) \quad (4.26)$$

$$\mathbf{g} = \text{sign}(x - 1) \sqrt{2(x - \ln x - 1)} \quad (4.27)$$

Where $\mathcal{C}_{f\ell}$ are the fiducial model bandpowers, ‘vecp()’ is a vectorization operation, and \mathbf{g} is a non-linear function defined above. With a likelihood calculation, we are now able to run an ML search on either the real data bandpowers or the 499 sim bandpowers. This will return an estimation of the parameters which we defined in our multi-component model.

Because the BPCM is a crucial aspect of our ML search, we would like to know how making adjustments to the construction will affect the bias on r . In the rest of this section, we explore the bias on r caused by the following alterations to the construction of the BPCM: (1) constructing a BPCM from fewer than 499 sims, (2) excluding sims (realization-by-realization) in the construction of the BPCM when calculating the ML search, and (3) constructing a BPCM leaving in experiment noise correlations between BK experiments.

As a reminder, the eight parameters of the multi-component model (Section 4.1) most often used in the ML search (i.e., free parameters) are: r , A_d , A_s , β_d , β_s , α_d , α_s , and ϵ . The remaining parameters are held fixed.

4.3.1 ML Search with Reduced Number of Sims

Making simulations is computationally expensive but we also do not want to introduce unnecessary simulation errors from too few simulations. Choosing the right number of sims is a balance. Historically, our analysis uses 499 sim realizations to make the BPCM. As the number of bandpowers we use in our analysis grows so does the size of the BPCM. This means that we should understand if 499 sims is enough given the current size of our BPCM. Also, we would like to know how using a BPCM constructed with fewer sim realizations

will affect the ML search (i.e., will it cause a bias on r). This subsection gives a brief look whether 499 sims is enough or if it is causing problems.

Within the BPCM, much of the information is contained within the diagonal. So when looking at a BPCM that is 702×702 , it is helpful to look at the diagonal to see how it changes when the number of sims used in the construction are decreased. Figure 4.3 shows a comparison of the diagonals of the different BPCMs. It is clear that with less sims, the variance increases. The baseline case, which was a BPCM constructed with the full 499 sims, is used as the point of comparison. Table 4.1 shows the values of the standard deviations for each of the cases.

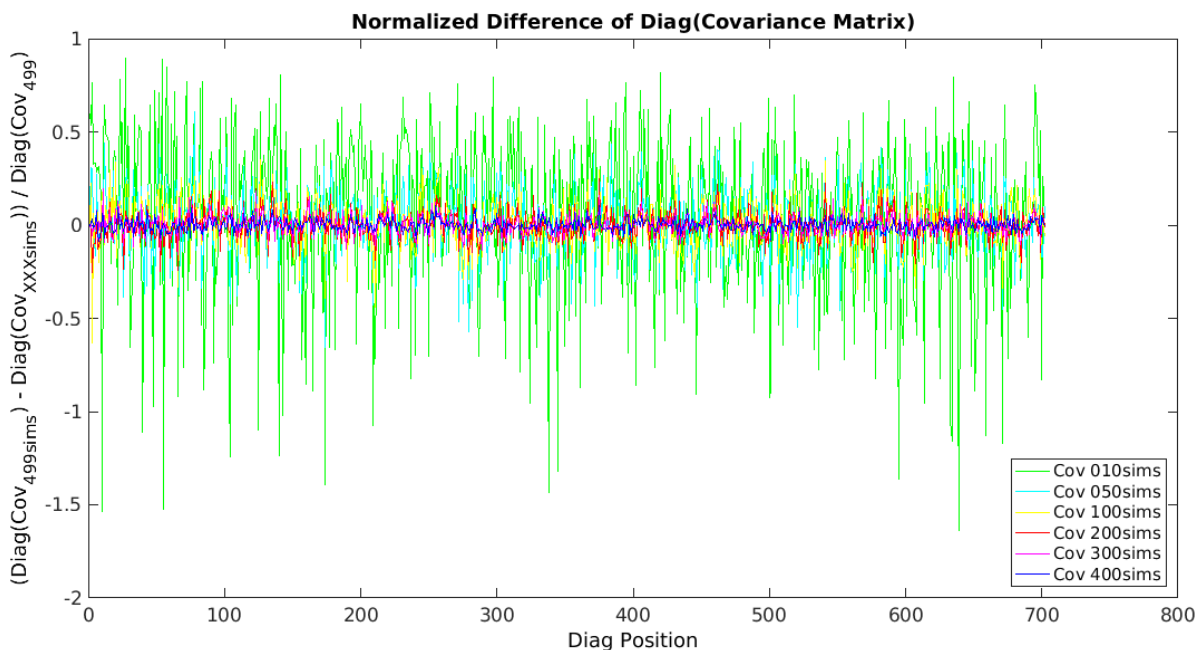


Figure 4.3: A comparison of the BPCMs constructed from different numbers of sims. The y-axis is plotting a fractional difference between the diagonal of the baseline case of 499 sims and the case in question $((diag(Cov_{499}) - diag(Cov_{XX})) / diag(Cov_{499}))$. The values of the standard deviations are shown in Table 4.1.

From the table, we can see that not only do the normalized standard deviations decrease as we get closer to 499 sims, they are starting to converge. We can use these values as an approximation for the case of comparing the 499 sims against the ideal infinite sim case. When we extrapolate to 499 sims, we get a $\sigma \approx 0.015$. We consider this within the acceptable

Number of sims	Standard Deviation
10	0.4369
50	0.1882
100	0.1267
200	0.0775
300	0.0519
400	0.0316

Table 4.1: The standard deviations from Figure 4.3.

bounds of error and, furthermore, it shows we will get diminishing returns by increasing the number of sims.

The next step is to see how decreasing the number of sims in the construction of the BPCM will affect the ML search of r . Realistically, we will never use a BPCM constructed with fewer than ~ 300 sims. So with this in mind, we did an ML search of the baseline case (r_{499}) and used it as a reference to two other cases; r_{300} and r_{400} . While the BPCM was constructed with fewer sim realizations, the actual ML search was done with all 499 sim realizations. Figure 4.4 shows the difference between the baseline case and the two different test cases. In the $r_{499} - r_{300}$ case: $\mu_{300} = -6.1 \times 10^{-4}$ and $\sigma_{300} = 1.0 \times 10^{-3}$. In the $r_{499} - r_{400}$ case: $\mu_{400} = -4.7 \times 10^{-4}$ and $\sigma_{400} = 7.6 \times 10^{-4}$. Again, we can use these values to try to approximate the bias caused from using 499 sims compared to infinite. We can use the values from Table 4.1 and the extrapolated point to approximate a $\sigma_{499} \approx 3 \times 10^{-4}$. Now using $\mu_{300}/\sigma_{300} = 0.61$ and $\mu_{400}/\sigma_{400} = 0.62$, we can approximate the magnitude of bias as $|\mu_{499}| = 0.6\sigma_{499} = 2 \times 10^{-4}$. This bias is relatively small compared to the $\sigma(r) = 0.02$ of our standard ML search with 499 sims. Therefore, we conclude that 499 sims is an acceptable amount for the construction of our BPCM.

4.3.2 Bias from Subsets of Sims

In the previous subsection, 99 sims and 199 sims were excluded in the construction of the BPCM before running an ML search. However, the 99 sims excluded in the first dataset were a subset of the 199 sims excluded in the second dataset. Ideally, the sims excluded would

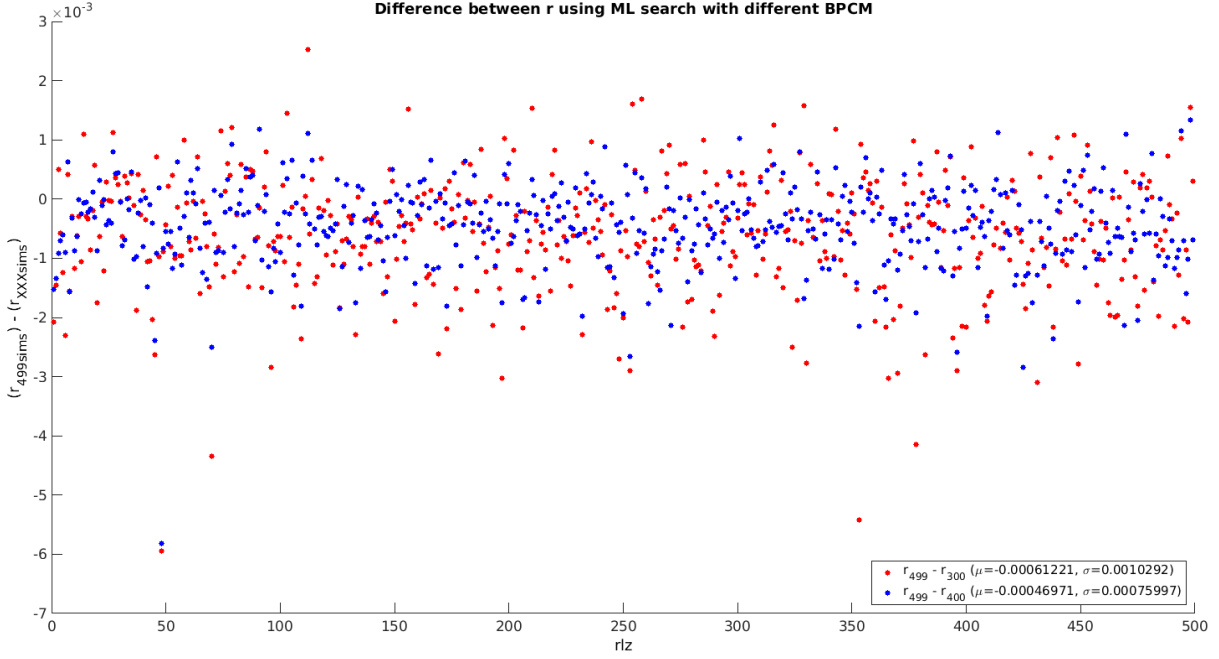


Figure 4.4: The scatter plot shows the difference rlz-by-rlz of the two test cases r_{300} and r_{400} with the baseline case r_{499} . In both cases, there is a slight (but small) negative bias on r .

have been chosen at random. So, as an additional check, we did a similar analysis but split the sims used in the construction of the BPCM into two halves. The purpose of this was to make sure there was not a small subset of sims driving the results.

The 499 sims were split into two halves. In the two cases, the two halves were excluded in the construction of the BPCM. Similar to the procedure of the previous subsection, an ML search was run with all 499 sims but using the modified BPCMs. The resulting r realizations were then subtracted from the baseline case. Figure 4.5 shows the difference between the two test cases and the baseline case. For the $r_{baseline} - r_{1st, half}$ case: $\mu_1 = -3.3 \times 10^{-4}$ and $\sigma_1 = 1.3 \times 10^{-3}$. For the $r_{baseline} - r_{2nd, half}$ case: $\mu_2 = 2.4 \times 10^{-4}$ and $\sigma_2 = 1.2 \times 10^{-3}$. It is not surprising, but perhaps reassuring, that the small bias on r is in opposite directions for the two halves. In both cases, the biases are $\sim 0.2\sigma$ away from zero. Because the magnitude are small and spread of the biases are similar for both halves, we do not believe that a small subset of sims was driving the bias in the previous subsection.

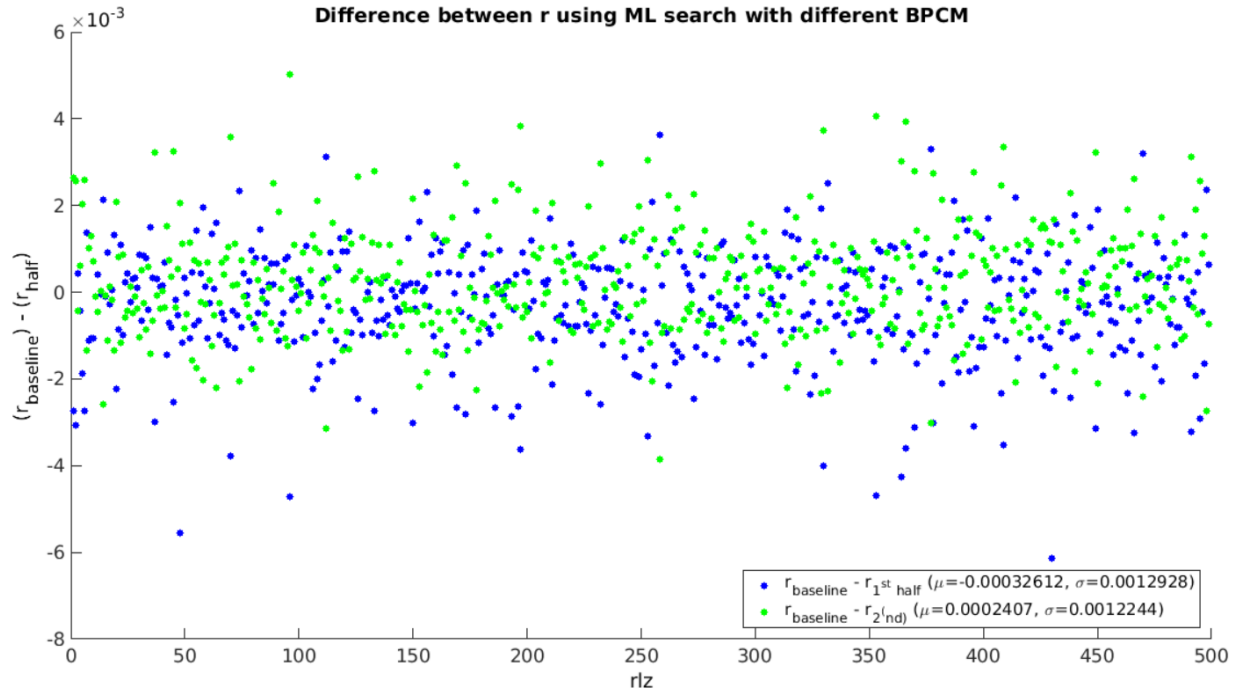


Figure 4.5: The scatter plot shows the difference rlz-by-rlz of the two test cases $r_{1st, half}$ and $r_{2nd, half}$ with the baseline case $r_{baseline}$. In both cases, there is a slight (but small) bias on r .

4.3.3 Exclude Sim Realization

Another variation of the ML search and BPCM construction calculated was a sim exclusion. In this variation, one sim was excluded from the construction of the BPCM. This BPCM was then used in the ML search for the sim which was excluded. This process was repeated for all 499 sims. We wanted to see if decoupling the BPCM construction from the ML search (via sim exclusion), would make a significant impact. Figure 4.6 shows the difference between the r realizations of the normal ML search $r_{baseline}$ and the exclusion ML search $r_{exclude}$. There was a very small difference between the default method and the exclude method (6.8×10^{-5}) so we concluded it was not necessary to change the pipeline.

4.3.4 BK Noise Correlations in BPCM

This subsection shows the effects of adding noise correlation between BK15 experiments. By default, the noise correlation between the bandpowers of the different experiments is set

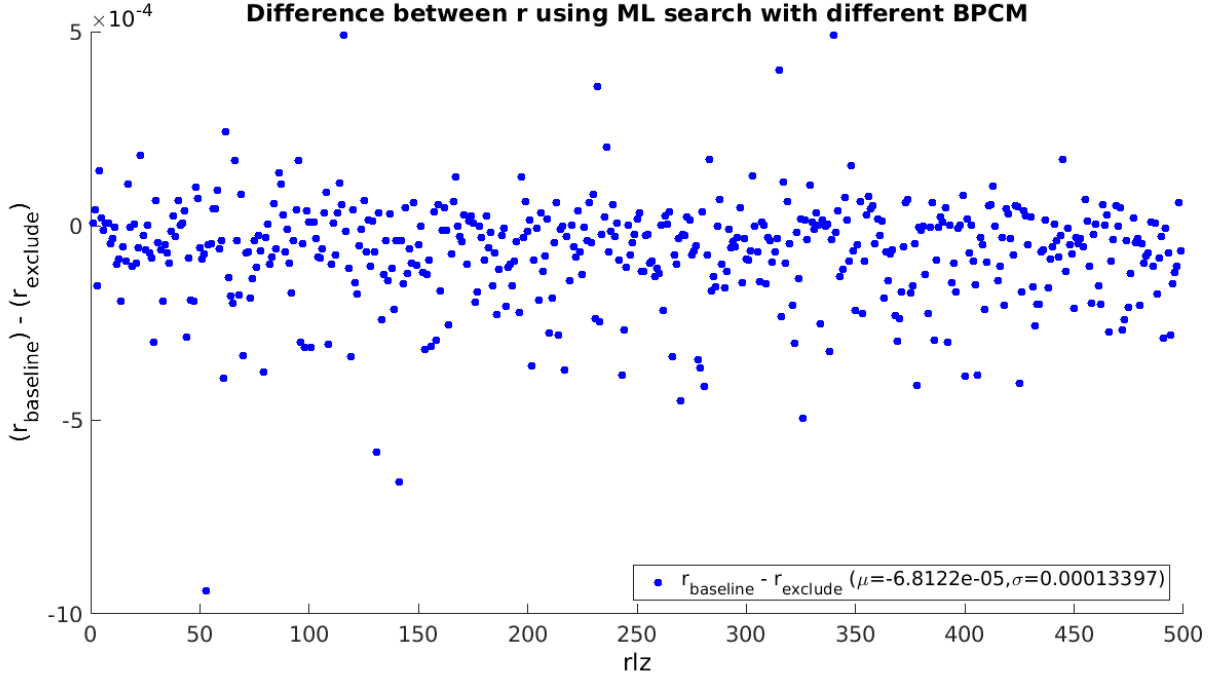


Figure 4.6: The scatter plot shows the difference rlz-by-rlz of the test cases r_{exclude} with the baseline case r_{baseline} . In both cases, there is a slight (but small) bias on r .

to zero during the conditioning of the BPCM. This is because we don't expect noise to be correlated among the different experiments we use in our bandpowers. This is true for both the noise correlation between BK, WMAP, and Planck bandpowers and for the different receivers frequencies within the BK experiment ('BK15-220', 'BK15-150', and 'BK15-95'). However, we might worry that there actually *is* noise correlation among the different BK experiments. So, in order to test this, we left the noise correlation turned on among the BK experiments. Again, we ran a default ML search r_{baseline} and compared it to the case where the noise correlation is left on among the three BK15 experiments. Figure 4.7 shows the difference on r between the two ML searches. Keeping the noise correlation among the BK15 experiments turned on has minimal effect on the $\mu(r)$ and $\sigma(r)$ of the r distribution. This is to be expected and further justifies our reasoning of turning the noise correlation off during the conditioning process.

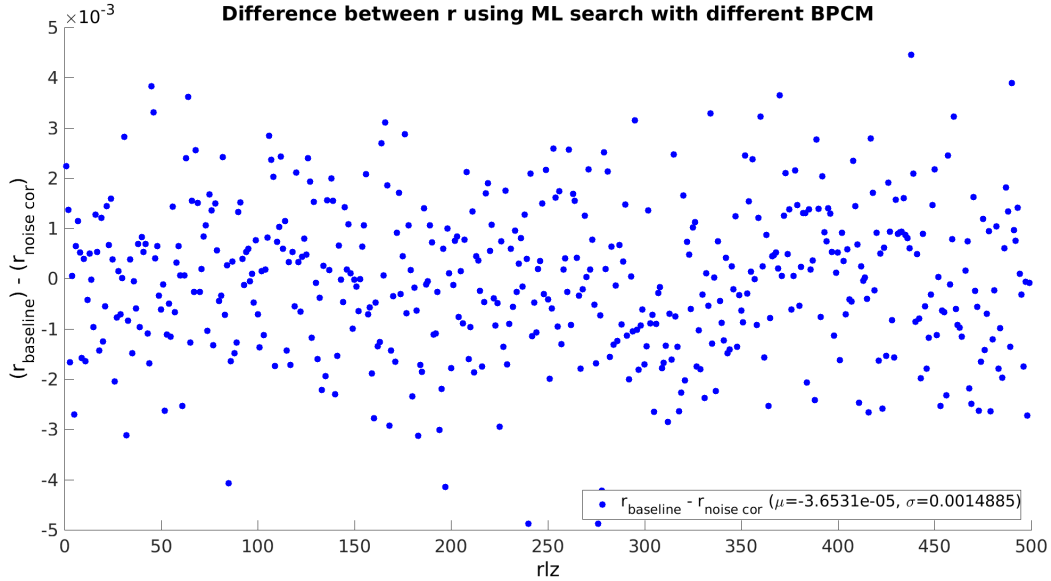


Figure 4.7: The scatter plot shows the difference rlz-by-rlz of the test cases $r_{noise\,cor}$ with the baseline case $r_{baseline}$. The resulting r bias between the two distributions is $\mu(r) = -3.65 \times 10^{-5}$

4.4 Quadratic Estimator

In our standard analysis we use a multi-parameter H-L ML search to estimate the value of r and the various other nuisance parameters. The ML search is often comprised of eight parameters and takes several hours to compute. In this section, I will describe how we can use the weighted sum of the bandpower expectation values to form a minimum variance estimator which, instead of taking hours, only takes seconds to compute. It gives comparable results and is an independent check of our parameter estimation as it doesn't rely on a bandpower likelihood approximation. Furthermore, because the construction is using bandpowers, it provides an opportunity to estimate systematic biases which would otherwise be tedious to calculate.

4.4.1 Formalism

In our analysis, we use a multi-component model to input various parameters to calculate the BB bandpower expectation values (expvals) as described in Section 4.1 in Equations 4.1

and 4.2. This model can be generally described as the sum of three signal terms (CMB, dust, and sync). Furthermore, the CMB term can be described by the lensed E -modes and the r amplitude. In this section, we will use a simplified notation of the multi-component model by absorbing terms which are held fixed and using a single scaling function for each term in the bandpower. Each signal term has an amplitude and scaling function which varies with both bandpower frequency, ν , and ℓ -bin. Equation 4.28 shows the model we use for the BB bandpower expvals.

$$\langle \xi \rangle = A_{CMB} f_{CMB}(\nu, \ell) + A_d f_d(\nu, \ell) + A_s f_s(\nu, \ell) \quad (4.28)$$

Where $\langle \xi \rangle$ is the bandpower expectation value, A_μ are the amplitudes for component μ , and $f_\mu(\nu, \ell)$ is the scaling term which is a function of both frequency, ν , and ℓ -bin. The CMB term can be further broken down into the lensed E -modes and r as:

$$A_{CMB} f_{CMB}(\nu, \ell) = [A_L f_L(\ell) + r f_r(\ell)] f_{CMB}(\nu) \quad (4.29)$$

Where $A_L = 1$ for the expected Λ CDM lensing of E -modes. Also notice how the frequency scaling is the same for the two CMB terms but they differ in ℓ scaling. It is more convenient to write this more compactly using Einstein summation convention as:

$$\langle \xi \rangle = A_\mu f^\mu(\nu, \ell) \quad (4.30)$$

In this notation, A_μ includes A_d , A_s , and r but not A_L . The lensing amplitude will be treated at the end through a lensing debias.

Now we can create an estimator, e , by taking the weighted (w_i) sums of the bandpowers

(ξ^i) :

$$e = w_i \xi^i \quad (4.31)$$

$$\langle e \rangle = w_i \langle \xi^i \rangle \quad (4.32)$$

Using the bandpower covariance matrix, \mathbb{C}^{ij} , and the bandpower weights, w_i , the variance of the estimator can be constructed as:

$$Var(e) = w_i \mathbb{C}^{ij} w_j \quad (4.33)$$

It will also be useful to construct a derivative matrix using the amplitudes of the component and the bandpower expectation values:

$$D^{k\mu} = \frac{\partial \langle \xi^k \rangle}{\partial A^\mu} \quad (4.34)$$

Where k is the bandpower expval index which includes all of bandpowers for every ℓ -bin and μ is the component index.

4.4.2 Creating an Estimator

In order to create the estimator, we start by minimizing the variance. However, we also want to add some constraints on the equation in order to isolate the various components. This can be accomplished by adding the constraint equations in the form of Lagrangian multipliers (λ). So we can write a Lagrangian equation to be minimized as:

$$\mathcal{L} = Var(e) - \lambda_\mu \left(\frac{\partial \langle e \rangle}{\partial A^\mu} - c^\mu \right) \quad (4.35)$$

Where c^μ is the constant used to either estimate the component ($c = 1$) or ‘suppress’ the component ($c = 0$). In other words, we ‘suppress’ a component by placing a constraint on

the estimator which makes it insensitive to that component. So for example, if we want an estimator which is insensitive to dust, then we use the constraint of $\partial e / \partial A_d = c^d = 0$. When the weighted bandpowers are summed, $w_i \langle \xi^i \rangle$, the dust component of the various weighted bandpowers (which can be negative) will cancel out.

Taking the derivatives with respect to the weights and Lagrangian multipliers:

$$\frac{\partial \mathcal{L}}{\partial w^i} = 2\mathbb{C}^{ij}w_j - D^{i\mu}\lambda_\mu \quad (4.36)$$

$$\frac{\partial \mathcal{L}}{\partial \lambda^\mu} = -w_k D^{k\mu} + c^\mu \quad (4.37)$$

We can solve for the estimator by solving for the weights. To do this, we construct a block matrix using \mathbb{C} , D , and the vectors of the both the weights and constraints

$$B = \left[\begin{array}{c|c} 2\mathbb{C} & -D \\ \hline -D^T & \emptyset \end{array} \right] \quad (4.38)$$

$$\vec{q} = \left[\begin{array}{c} \vec{w} \\ \vec{\lambda} \end{array} \right] \quad (4.39)$$

$$\vec{Z} = \left[\begin{array}{c} \vec{\emptyset} \\ -\vec{c} \end{array} \right] \quad (4.40)$$

and then solve for \vec{q}

$$B\vec{q} = \vec{Z} \quad (4.41)$$

$$\vec{q} = B^{-1}\vec{Z} \quad (4.42)$$

The estimator can now be constructed with the bandpowers ($\vec{\xi}$) and the weights (\vec{w}). The Lagrangian multipliers ($\vec{\lambda}$) are of no particular interest. While this method works well for the three amplitude parameters, it does not work (as is) for the dust and sync scaling

parameters. This is because the derivatives of the bandpower expectation values with respect to the scaling parameters are still dependant on the scaling parameters. In other words, the constraint equations are not well behaved for non-linear parameters. A modified method of the estimator for the scaling parameters will be discussed in Section 4.4.4.

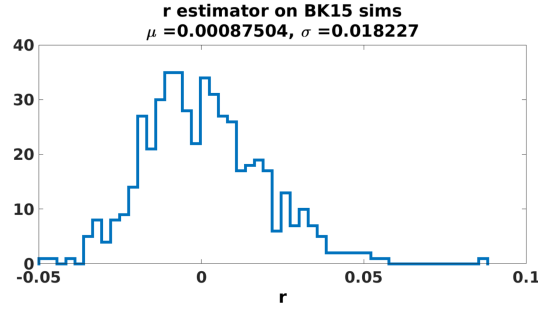
In order to complete the estimator, an additional step of lensing debias is applied. Recall that the CMB signal was comprised of both the r component and lensed Λ CDM (Equation 4.29). So in order to remove this remaining lensing signal, we create another set of bandpower expvals except we change the input parameters of the model. Specifically, all of the amplitude parameters are zeroed while the amplitude of the lensing signal remains unchanged (i.e., $r = 0$, $A_d = 0$, $A_s = 0$, and $A_L = 1$). This creates a set of bandpower expvals with only a lensed Λ CDM signal. The estimator that was created before, $e()$, will be applied to these lensing-only bandpower expvals, $\langle \xi_0^i \rangle$, and result in a lensing bias which can be subtracted from the original estimator.

$$\begin{aligned}
 e_{de} &= e(\xi^i) - e(\langle \xi_0^i \rangle) \\
 &= w_i \xi^i - w_i \langle \xi_0^i \rangle \\
 &= w_i (\xi^i - \langle \xi_0^i \rangle)
 \end{aligned} \tag{4.43}$$

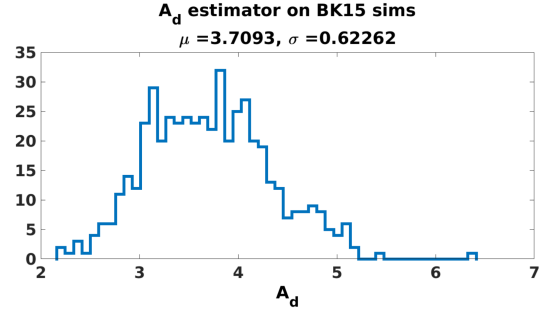
The lensing debias cancels out any of the CMB signal which came from the lensed E -modes.

4.4.3 Estimator on BK15 sims

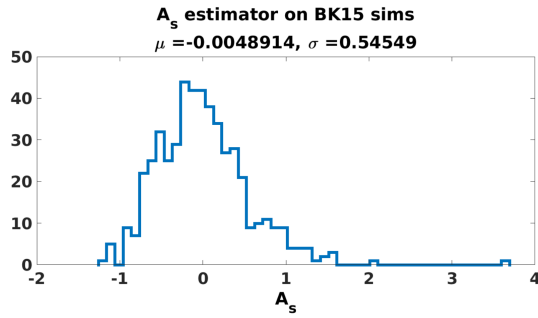
The quadratic estimator method was applied to the 499 sims used in our BK15 dataset. The BK15 dataset has 9 science ℓ -bins (ℓ -bins 2 through 10) and 78 BB bandpowers. So all combined there were a total of 702 bandpowers used in a weighted linear combination to create three different estimators; one for each of the amplitude parameters (r , A_d , and A_s). The scaling parameters were held fixed at their default values. The default parameter values were used in the input model and these match the model which was used to create the sims:



(a) r estimator on BK15 sims. The dust and sync components have been suppressed. The histogram has a mean of 8.75×10^{-4} and a std. of 0.018.



(b) A_d estimator on BK15 sims. The CMB and sync components have been suppressed. The histogram has a mean of 3.709 and a std. of 0.62.



(c) A_s estimator on BK15 sims. The CMB and dust components have been suppressed. The histogram has a mean of 4.89×10^{-3} and a std. of 0.55.

Figure 4.8: The histograms of the minimum variance quadratic estimators on the BK15 sims. These show the three amplitude parameters.

- $r = 0$
- $A_d = 3.75$
- $A_s = 0$
- $\beta_d = 1.6$
- $\beta_s = -3$
- $\alpha_d = -0.4$
- $\alpha_s = -0.6$

Figure 4.8a shows the histogram of the estimator applied to the sims pulling out the r component and suppressing the A_d and A_s . The histogram for A_d is shown in Figure 4.8b

where r and A_s are suppressed. And finally, the histogram for A_s is shown in Figure 4.8c where r and A_d are suppressed. In each of these cases, the estimator gives a very similar result to our conventional ML search. The means and standard deviations of the realizations of both the quadratic estimator and the standard ML search as can be seen in Table 4.2.

	Quadratic Estimator	ML Search
$\mu(r)$	8.75×10^{-4}	-2×10^{-3}
$\sigma(r)$	0.018	0.018
$\mu(A_d)$	3.709	3.8
$\sigma(A_d)$	0.62	0.7
$\mu(A_s)$	0.005	0.09
$\sigma(A_s)$	0.55	0.68

Table 4.2: BK15 comparison between the the quadratic estimator and standard ML search (amplitude parameters).

4.4.4 Estimating Scaling Parameters

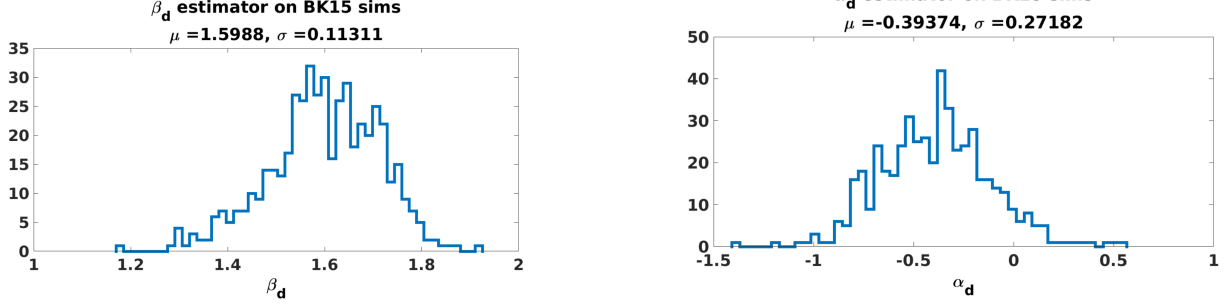
Polarized dust is modeled as a modified blackbody spectrum and the scaling function used in the multi-component model goes as:

$$f_{dust} \propto \left(\frac{\nu}{\nu_0} \right)^{\beta_d+3} \quad (4.44)$$

Where f_{dust} is the same scaling function as in Equation 4.28, ν_0 is the pivot frequency, and β_d is the scaling parameter. If the constraint was taken in the same way as the amplitude parameter (i.e., $\frac{\partial \langle e \rangle}{\partial \beta_d}$) it would yield the following:

$$\frac{\partial \langle e \rangle}{\partial \beta_d} \propto \ln \left[\frac{\nu}{\nu_0} \right] \left(\frac{\nu}{\nu_0} \right)^{\beta_d+3} \quad (4.45)$$

Because this constraint is still a function of β_d , the estimator will not be well constrained and give an incorrect result. However, if we take the scaling parameter to be approximately linear about the input model, then we can form a method for the estimator by using the



(a) β_d estimator on BK15 sims. The histogram has a mean of 1.60 and a std. of 0.11.

(b) α_d estimator on BK15 sims. The histogram has a mean of -0.39 and a std. of 0.27.

Figure 4.9: The histograms of the modified minimum variance quadratic estimators on the BK15 sims. These show the two dust scaling parameters.

following:

$$\beta_d = \tilde{\beta}_d - e(\langle \xi^i \rangle) + e(d^i) \quad (4.46)$$

Where $\tilde{\beta}_d$ is the input model parameter, $e(\langle \xi^i \rangle)$ is the estimator applied to the bandpower expvals, $e(d^i)$ is the estimator applied to the bandpower sims or real data, and β_d is the resulting modified estimator for the scaling parameter. It should be noted that this type of estimator assumes a value of $\beta_d = \tilde{\beta}_d$ when calculating the weights for $e(\langle \xi^i \rangle)$ and $e(d^i)$. In a similar fashion, we can create an estimator for the rest of the scaling parameters: β_s , α_s , and α_d . Figure 4.9 shows when the β_d estimator and α_d estimators are applied to the BK15 sims.

The β_d and α_d estimators can be compared to the ML search results in Table 4.3. So again, the estimator returns results which are comparable with our conventional ML search. While it is possible to use the estimator on the sync scaling parameters (β_s and α_s), the baseline BK15 sims don't contain any level of sync. Because of this, the scaling parameters are not well defined for our standard BK15 sims and the estimator gives fairly extremely results. However, estimators of these sync scaling parameters will be shown in the next section.

	Quadratic Estimator	ML Search
$\mu(\beta_d)$	1.60	1.62
$\sigma(\beta_d)$	0.11	0.22
$\mu(\alpha_d)$	-0.39	-0.46
$\sigma(\alpha_d)$	0.27	0.36

Table 4.3: BK15 comparison between the the quadratic estimator and standard ML search (dust scaling parameters). Note: it is typical for the BK Collaboration to use a prior on β_d in the ML search, however, the prior was not included in these calculations. This gives a better comparison of the ML search to the QE.

4.4.5 Iterative Method

A natural extension of the quadratic estimator framework is to create iterations of the estimators and see how they converge on parameters. The method is simple enough; we start with a set of starting parameters and use the output of the estimators as the new input parameters. These iterations are continued until there is a sufficient convergence in both mean and standard deviation. We can write the set of starting parameters P as: $P = [r^{(0)}, A_s^{(0)}, A_d^{(0)}, \beta_s^{(0)}, \beta_d^{(0)}, \alpha_s^{(0)}, \alpha_d^{(0)}]$ or more compactly as $P = [p_1^{(0)}, p_2^{(0)}, \dots, p_n^{(0)}]$ where the subscript indicates the model parameter and the superscript indicates the iteration number. One iteration will look like the following:

$$\begin{aligned}
e_1(P) &= p_1^{(1)} \\
P(p_1^{(0)}) &\rightarrow P(p_1^{(1)}) \\
e_2(P) &= p_2^{(1)} \\
P(p_2^{(0)}) &\rightarrow P(p_2^{(1)}) \\
&\vdots \\
e_n(P) &= p_n^{(1)} \\
P(p_n^{(0)}) &\rightarrow P(p_n^{(1)})
\end{aligned}$$

This iterative method usually converges on a parameter value after 15 or 20 iterations. The time scale is of an order of a few seconds to compute which is orders of magnitude faster

than our conventional ML search.

The iterative QE was applied to a variety of different types of sims. This first sim type shown is the standard BK15 sim which we refer to as our ‘gdust’ sim (Gaussian dust). In gdust BK15 sims, there is no r or synchrotron and the dust parameters are: $A_d = 3.75\mu K^2$, $\beta_d = 1.6$, and $\alpha_d = -0.42$. Because there is no level of synchrotron, generous limits of $\beta_s = [-7, 1]$ and $\alpha_s = [-3, 3]$ were put on the synchrotron scaling parameters to have a well-behaved A_s . Additionally, limits of $\beta_d = [0.8, 2.4]$ and $\alpha_d = [-2, 2]$ were put on the dust scaling parameters in order to mirror previous analysis on the alternative foreground models. The limits put on the dust scaling parameters were never reached by any of the realization so they had no effect. Figure 4.10 shows the histogram of the parameter estimators after 20 iterations. Figure 4.11 shows the mean and standard deviations of the realizations for all 20 iterations.

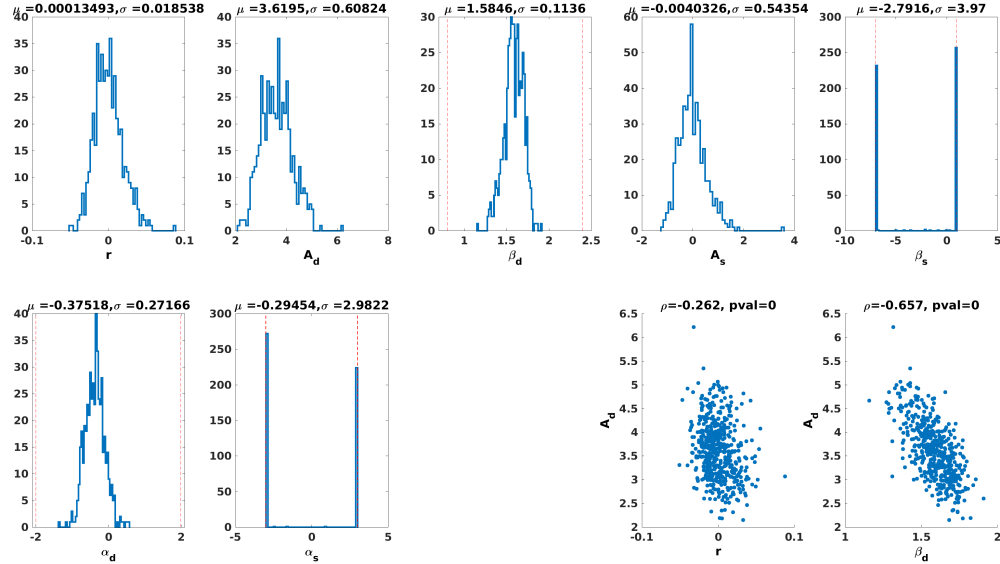
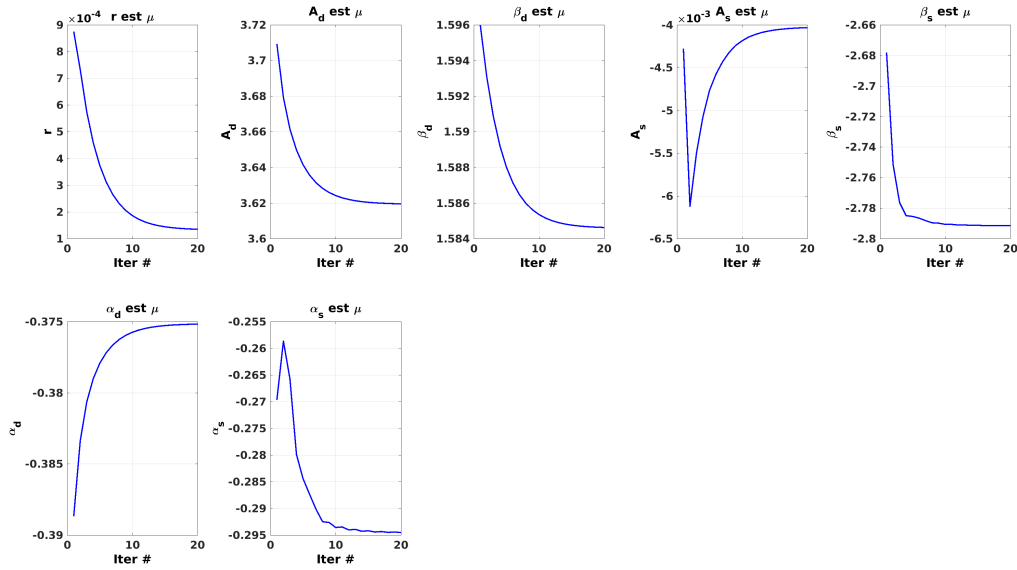
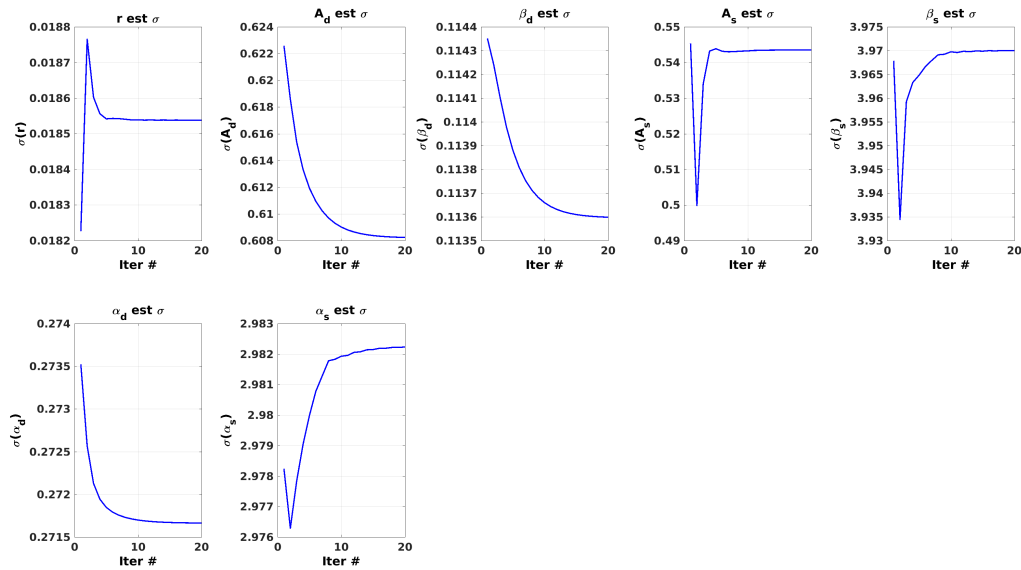


Figure 4.10: The histogram of the parameters after 20 iterations of the quadratic estimator. Also included are two correlation plots in the bottom right. Figure 4.11 shows how the different iterations converge in both the mean and the standard deviation of the realizations.



(a) The realization means as a function of iteration number.



(b) The realization standard deviations as a function of iteration number.

Figure 4.11: The iteration details after 20 iterations of the QE applied on the ‘gdust’ sims. Figure 4.10 shows the histogram after the last iteration.

4.4.6 Alternative Foreground Sims

In the last section, the iterative method of the quadratic estimator was applied to our ‘gdust’ BK15 sims. In this section, the iterative estimator method is applied to a few alternative foreground sims. This provides a good test for this method as these sims were made from different theoretical models than our multi-component model. These alternative foreground models are some of the models being considered for CMB-S4⁵.

The following are the naming conventions used by the BK Collaboration as well as a brief description of the alternative models. These alternative foreground model simulations can be found in the CMB-S4 report to the Astronomy and Astrophysics Advisory Committee which is part of the National Science Foundation [72]. These alternative foreground models are generated using an open-source python code (PySM) for generating galactic polarization relevant to CMB experiments⁶.

- **1682x1683:** PySM model a2d4f1s3 for CMB-S4. Two-component dust. Curvature in synchrotron spectral index. Polarized Anomalous Microwave Emission (AME) [73].
- **1688x1689:** Flauger–Hensley magneto-fluid dynamic sims that are meant to provide a consistent simulation of dust and synchrotron [74].
- **1691x1692:** PySM model a1d1f1s1 for CMB-S4. Most basic PySM model including dust, synchrotron, AME, and free-free emission. Free-free emission refers emission caused by scattering of electrons off ions in the interstellar medium [73].
- **1693x1694:** PySM model a2d7f1s3 for CMB-S4. Hensley–Draine dust with more complicated spectral energy distribution. Curvature in synchrotron spectral index. Polarized AME [75].

While these alternative foreground models contained various levels of dust and sync, none of them contained any level of r . Applying the iterative estimator method to all of these alternative foreground sims yielded a reassuring result; in all cases, r was consistent with

⁵A next stage CMB experiment which will provide powerful constraints on r .

⁶<https://github.com/bthorne93/PySM>

zero. The nuisance foreground parameters did change quite a bit in relation to the baseline ‘gdust’ foreground model but this was to be expected.

4.4.7 Direct Likelihood

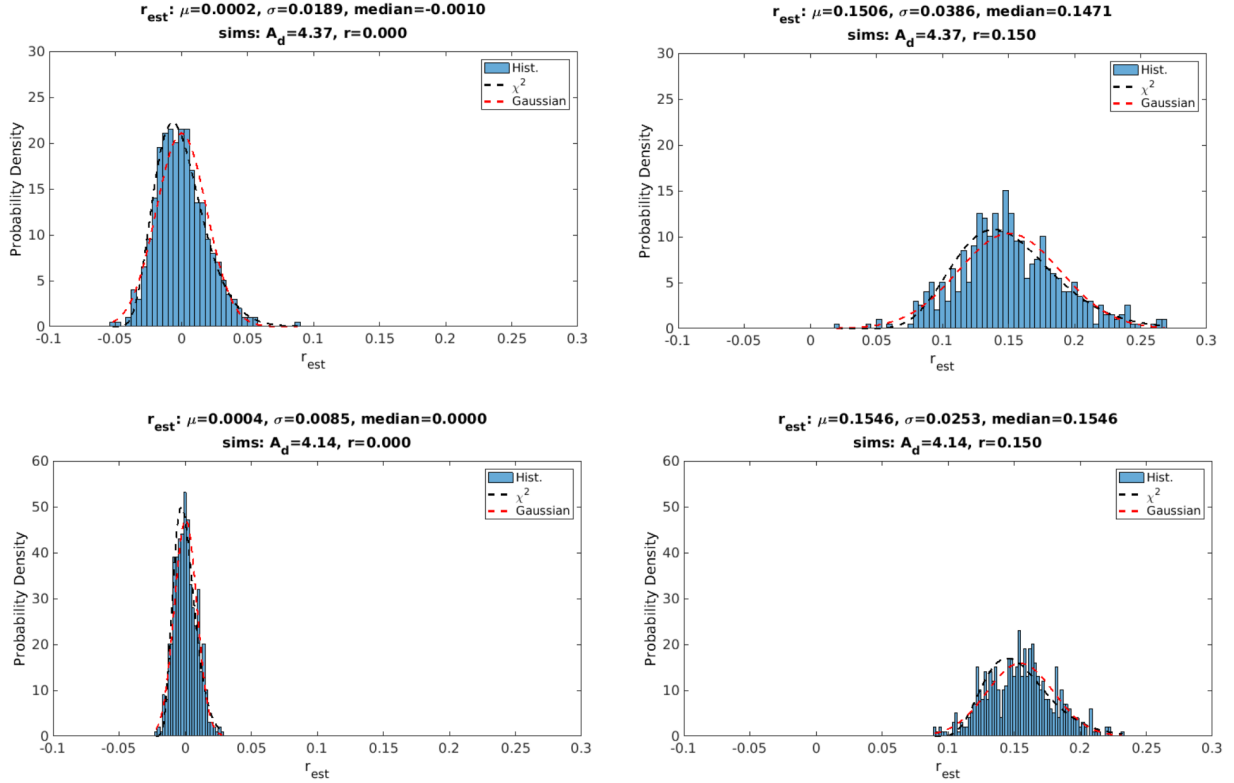


Figure 4.12: Quadratic estimator likelihood histograms. Shown are two of the 76 histograms made for the different values of r_{sim} . The top left panel shows the $r_{sim} = 0$ for BK15, top right shows $r_{sim} = 0.15$ for BK15, bottom left shows $r_{sim} = 0$ for BK18lf, and bottom right shows $r_{sim} = 0.15$ for BK18lf. This is all for $A_d = A_{d_{est}}$. The x-axis shows the value of r_{est} which spans the same range for all four panels. The y-axis is the probability density but the scale is double the range for the BK18lf plots (bottoms) because of the narrower distributions.

As stated earlier, the advantages of the quadratic estimator method is that (1) it doesn’t rely on a bandpower likelihood approximation and (2) it is much faster to calculate. These advantages provide the opportunity to make a direct likelihood calculation. The first step is to make modified ‘gdust’ sims that have various levels of r . The default sims have $r = 0$ and

$r < 0$ is unphysical so we made 76 modified sims with r values ranging from $r = 0$ to $r = 0.15$ with steps of $\Delta r = 0.002$. Ideally, the r estimator would have little to no dependence on the levels of A_d . However, in order to test this, we made several sets of the 76 modified r value sims with various levels of A_d . In all of these modified sims, $A_s = 0$. This was done for both BK15 sims and BK18lf sims. Table 4.4 shows a break-down of all of the values used for modified sims.

Parameter	Sim Value
r	0 – 0.15 ($\Delta r = 0.002$)
A_d	1.5, 3.5, 4, Ad_{est} , 7

Table 4.4: Modified sims values for direct likelihood calculation. Here, Ad_{est} is the A_d value returned by the estimator applied on the real data. For BK15, $Ad_{est} = 4.37$ and for BK18lf, $Ad_{est} = 4.14$.

After making all of the sim variations, the iterative quadratic estimator was applied to the sims with 30 iterations. r , A_d , A_s , β_d , β_s , α_d , and α_s were all free parameters while the following parameters were held fixed: $\epsilon = 0$, $A_L = 1$, $T_d = 19.6$, $EB_d = 2$, $EB_s = 2$. The resulting r histograms were fit with both a Gaussian pdf and a χ^2 pdf. Figure 4.12 shows a few of the histograms with their fits. It is worth noting that varying the values of A_d in the sims does not cause a bias on r but it does cause a slight widening of the distributions. The effect is small enough that it is not a concern which will be shown later in the likelihood.

By eye, it would appear that the χ^2 pdf is a good fit but in order to test this we performed a Kolmogorov-Smirnov (KS) test which tests whether two probability distributions differ. Figure 4.13 shows this for all the r values (Ad_{est}) of BK15 on the left and for BK18lf on the right. It is clear from the KS statistic that the χ^2 is a good fit and better than the Gaussian fit for BK15. In terms of BK18lf, χ^2 seems to be a better fit overall but it is not as clear for higher values of r .

We can now take all of the values of the sims and the corresponding estimates for r to make a likelihood parameter space for r . We can use the binned values, but since we believe the χ^2 fit describes the distribution well, we can instead use the continuous χ^2 pdf to increase

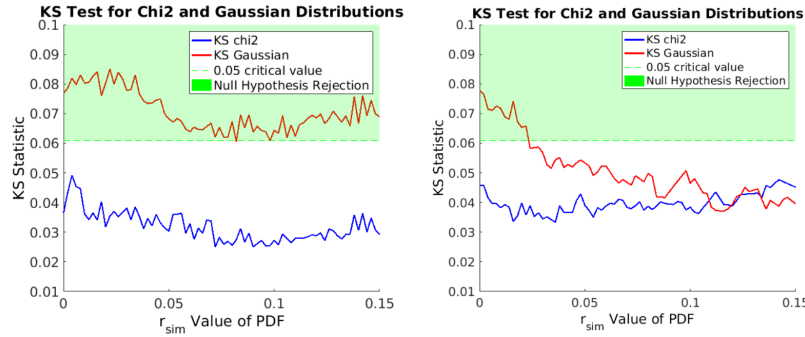


Figure 4.13: KS statistic for likelihood pdf fits. On the left is the KS test for BK15 Ad_{est} . On the right is the KS test for BK18lf Ad_{est} . The blue line is the KS statistic for the χ^2 fit and the red line is the KS statistic for the Gaussian fit. The green area is the null hypothesis rejection region where the null hypothesis is that the histogram is drawn from the reference distribution. In this case, the rejection level was calculated at the 5% level.

the resolution of the space. Figure 4.14 shows a view of both BK15 and BK18lf for both the χ^2 fit and the normalized binned values. It is clear from the plots that BK18lf puts a tighter constraint on r than BK15. In the plots, A horizontal slice describes a normalized pdf of r for a particular theory of r . A vertical slice describes the likelihood function for that value of r .

Taking the likelihood parameter space plots, we can now calculate some confidence intervals and some Bayesian credible intervals. For the confidence interval we calculate the Feldman-Cousins (FC) [76] 95% confidence interval. For the Bayesian credible interval, we calculate the highest probability density (HPD) 95% credible interval. Figure 4.15 shows the parameter space with the FC confidence interval (dashed black) and the HPD credible interval (dashed red). In both cases, the intervals seem to agree fairly well. In addition to the intervals, we have also applied the estimator on the real data with a result of $r = 0.0102$ for BK15. This result is shown in Figure 4.15a as the solid vertical black line. The same is possible for BK18, but the data is unpublished as of now so it was left off the of plot.

After looking at the whole parameter space, we now focus on the likelihood curves (which are vertical slices in the parameter space plots). We can compare the likelihood curve of the real data to the likelihood curves of the baseline sims normalized by the peak. In other

words, we use all of the r values returned by the estimator on the baseline sim data ($r = 0$ and $A_d = 3.75$) and look at the likelihood curves (vertical slices) of those values. Figure 4.16a shows a plot of all of these likelihood plots in gray in no particular order⁷. Additionally, the value of the real data is plotted as a bold black line. In this case, the x-axis does not extend in the negative as those are unphysical values. For BK15, 38% of sims peak at zero.

In addition to the likelihood curves of the baseline sims, Figure 4.16b also shows the likelihood curves of the real data but using the various models of A_d . As stated before, there was no bias caused by changing the value of A_d in the model. However, one might worry that we are not fully probing all of the parameter space and that we would need to marginalize over A_d for our likelihood. In the figure, the more realistic levels of dust are shown in black ($A_d = 3.5$), blue ($A_d = 3.75$), green ($A_d = 4.0$), and magenta ($A_d = A_{d_{est}} = 4.37$). Also shown are two more extreme values in the dashed cyan ($A_d = 1.5$) and dashed yellow ($A_d = 7.0$). This figure demonstrates that the r estimator is largely insensitive to the amplitude of dust. Even with these more extreme models, we do not see a bias, only a slight widening of the curve.

Lastly, we can compare the likelihood of the quadratic estimator to the standard ML search likelihood which was published with the BK15 results [37]. Figure 4.17 shows the likelihood curves for the estimator at the value of the real data, i.e., the solid vertical line in the confidence interval plot. It is especially interesting to compare the black curve to the dashed red curve. While they are fairly similar, the quadratic estimator prefers a lower value of r and seems to be slightly tighter.

4.5 Systematic Errors with CMB-S4

CMB-S4 is the next stage of CMB experiments which will provide powerful constraints on r . Before the construction of these experiments, we want to know the levels of systematic biases we will be measuring. The quadratic estimator can now be adapted to measure systematic

⁷This type of plot is often called a ‘Welter of lines’ plot internal to the BK Collaboration.

uncertainties instead of controlling for nuisance parameters.

The projected sensitivity on r for CMB-S4 is $\sigma(r) \sim 5 \times 10^{-4}$ [77]. The benchmark value for the systematic biases in CMB-S4 is set to approximately five times less than the projected sensitivity, $r \sim 1 \times 10^{-4}$. With the quadratic estimator, we have measured the systematic biases that come from bandcenter uncertainties (both correlated and uncorrelated) and various additive systematics that scale with frequency, angular scale, and different foregrounds [78]. All of these were calculated using nine different observing bands (20GHz, 30GHz, 40GHz, 85GHz, 95GHz, 145GHz, 155GHz, 220GHz, 270GHz) proposed for CMB-S4.

4.5.1 Uncorrelated Bandcenter Error

In measuring the bias that comes from bandcenter uncertainties, we analyze sets of simulated CMB-S4 data with different bandcenter values. The baseline model assumes true bandcenter values and we compare this baseline to sets of simulations that assume a slight deviation from the true bandcenters. In the end, we would like to know the bandcenter uncertainty tolerance within the benchmark value defined in Section 4.5. In order to get the systematic bias on r caused by bandcenter uncertainty, two different estimators of r are calculated; one using the correct bandcenters and the other, using bandcenters that have a slight deviation from the true bandcenter. Equation 4.47 shows how these estimators, along with the data, are used to get the bias:

$$bias = \langle e_{un}(d) - e_0(d) \rangle \quad (4.47)$$

Where d is the set of CMB-S4 simulated data, $e_{un}()$ is the estimator calculated from the model with incorrect uncorrelated bandcenters, and $e_0()$ is the estimator calculated from the model with the correct bandcenters.

To calculate the uncertainties used in the incorrect bandcenters, we used an uncorrelated nine-dimensional Gaussian distribution centered about 0% bandcenter error with a standard deviation, σ . A set of bandpower expvals were made from the mean of 10,000 simulated

bandpower realizations. Sets of bandpower expvals were made for various levels of bandcenter uncertainties and for various levels of delensing. The resulting bias caused by these various models of bandcenter uncertainties and delensing are shown in Figure 4.18. Also seen is the benchmark tolerance value and a quadratic fit. As can be seen in Figure 4.18, The benchmark value is crossed at an uncorrelated bandcenter uncertainty level between 0.5% and 1% which is true for all levels of delensing.

4.5.2 Correlated Bandcenter Error

The correlated bandcenter error case, had the same procedure to that of the uncorrelated case but in this case, perfectly correlated bandcenter errors were used for the nine observing frequencies:

$$bias = \langle e_{corr}(d) - e_0(d) \rangle \quad (4.48)$$

The bandpower expvals were calculated from bandcenter uncertainties that were varied simultaneously and by the same amount for each frequency. Because this method of calculating bandpower expvals did not involve a distribution of band centers like the uncorrelated case, it was possible to look at both positive and negative deviations from the true bandcenter errors. Figure 4.19 shows the resulting bias of the correlated bandcenter uncertainties for the various delensing levels. It is worth noting that the perfectly correlated bandcenter uncertainties are actually more forgiving than the uncorrelated case. It is possible to have a range of bandcenter uncertainties between -2.7% and 1.9% while still being under the benchmark value.

4.5.3 Additive Systematic Errors

Similar to the bandcenter uncertainties, we would like to account for various additive systematic inherent to the CMB-S4 experiment. An example of such a systematic is with a temperature-to-polarization leakage due to beam difference between detector pairs (discussed

in Section 2.4.2). Two sets of similar bandpower simulations were made for the additive systematics. The first, called 02.00, is the baseline simulation and contains 1000 realizations. The second set, called 03.00, is the same as 02.00 except that it includes various additive systematics. While 03.00 also includes 1000 realizations, it is separated into eight sections of 125 realizations with each section containing a different type of additive systematic. In a similar procedure as the bandcenter uncertainties, the bias on r is calculated via:

$$bias = \langle e_r(d_{03.00}) - e_r(d_{02.00}) \rangle \quad (4.49)$$

The same estimator, e_r , was applied to the two different simulated data sets; 02.00 and 03.00. Figure 4.20 shows eight different realization sections separated by the dashed vertical lines. Again, there were several levels of lensing debias but a value of $A_L = 0.1$ was chosen as example. There were also two different levels of r modeled ($r = 0$ and $r = 0.003$). The first 125 realizations are a control group and contain no additive systematics which shows in the fact that all of the biases of the realizations are zero. The bias from the various types of additive systematics are either close to or within the benchmark value with the highest bias at 1.37×10^{-4} . Also note that all of the biases are positive which would be expected given that they are all adding signal in various ways.

The use of bandpowers is widely used in the CMB scientific community (and CMB-S4) given its ability to express all of the relevant statistics of the CMB (discussed in the first paragraph of this Chapter 4). With the method outlined in this section, we can convert modifications of multi-frequency bandpowers into a bias on r . This means that we can easily extend this method to calculating other CMB-S4 systematics on r given the input of the modified bandpowers.

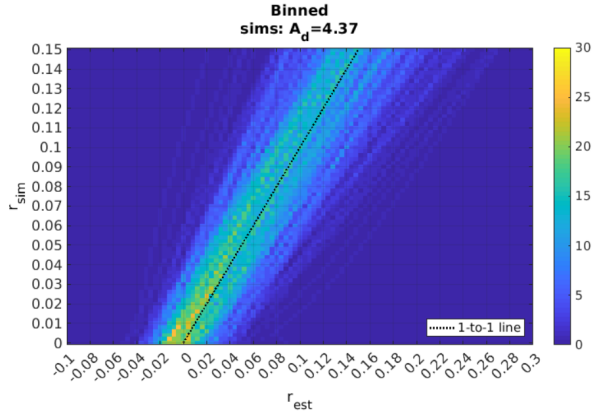
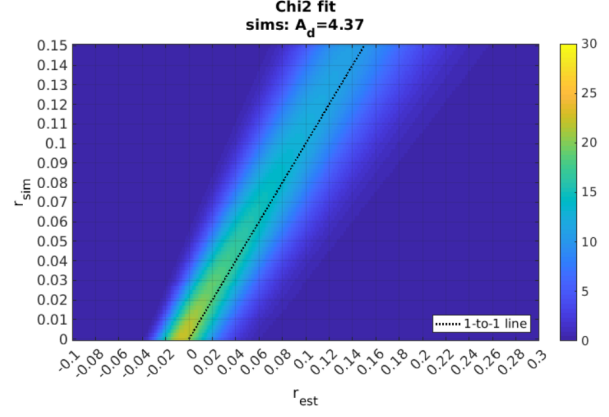
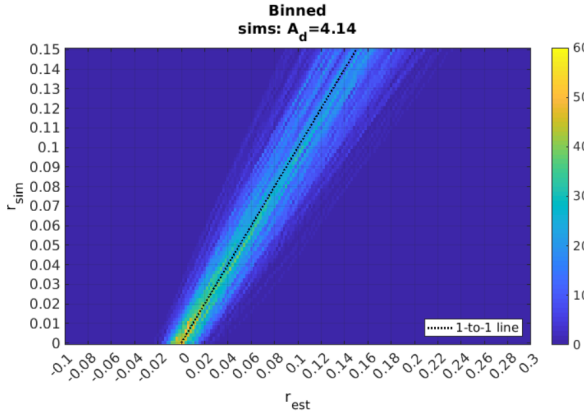
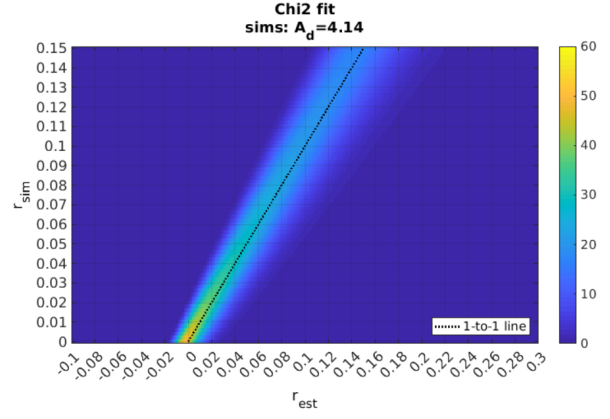
(a) BK15 $A_d = A_{d_{est}}$ binned.(b) BK15 $A_d = A_{d_{est}}$ χ^2 fit.(c) BK18lf $A_d = A_{d_{est}}$ binned.(d) BK18lf $A_d = A_{d_{est}}$ χ^2 fit.

Figure 4.14: The likelihood space of the iterative quadratic estimator. The y-axis is the value of r_{sim} and the x-axis is the value of r_{est} applied to the sims. A horizontal slice describes a normalized pdf of r for a particular theory of r . A vertical slice describes the likelihood function for r . It is clear that BK18lf offers a tighter constraint on r than BK15. The color scale for the BK18lf spans twice the range compared to that of BK15. The dotted black line shows the 1-to-1 between r_{sim} and r_{est} .

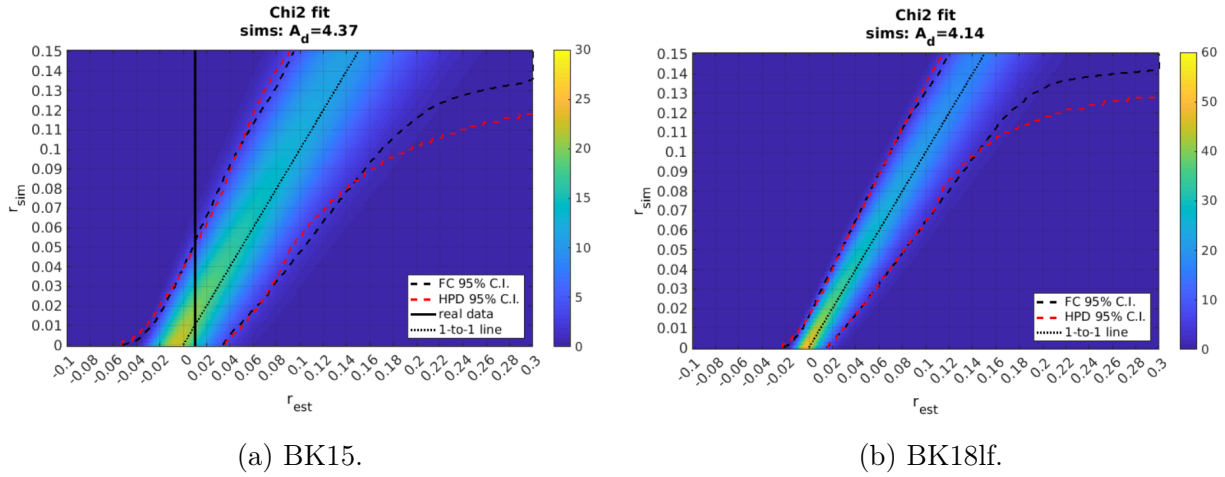


Figure 4.15: Quadratic estimator confidence interval for BK15 and BK18lf. The dashed red black line shows the Feldman-Cousins 95% confidence interval and the dashed black line shows the Bayesian HPD 95% credible interval. The vertical solid black line shows the estimator applied to the real data. The dotted black line shows the 1-to-1 between r_{sim} and r_{est} .

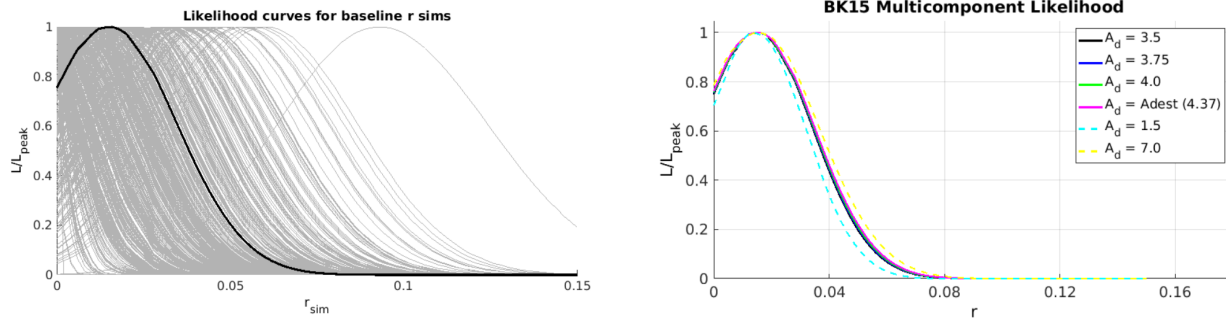


Figure 4.16: BK15 quadratic estimator likelihood curves

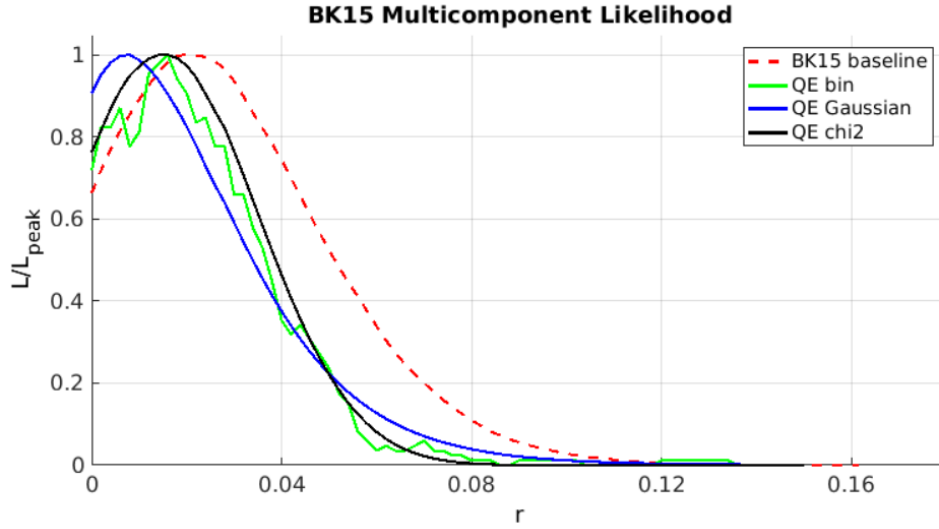


Figure 4.17: BK15 quadratic estimator real data likelihood curve. Shown are the χ^2 fit (black), the binned (green), the Gaussian fit (blue), and the BK15 baseline published by the BK Collaboration (dashed red). While we expect the χ^2 best represents the data, we have also shown the Gaussian fit as a comparison.

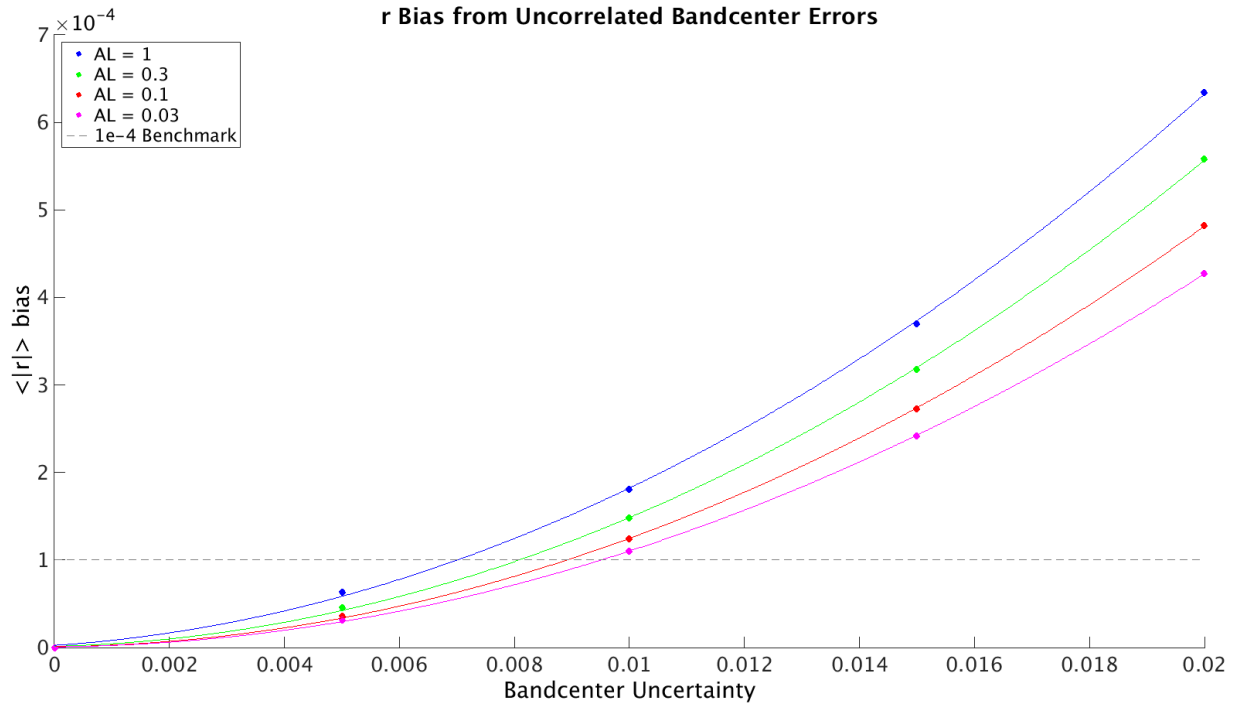


Figure 4.18: Bias on r caused by uncorrelated bandcenter uncertainties. The points show the calculated values and the lines show a quadratic fit. The various levels of delensing are shown in the different colors with no delensing in blue. The horizontal dashed line shows the benchmark value.

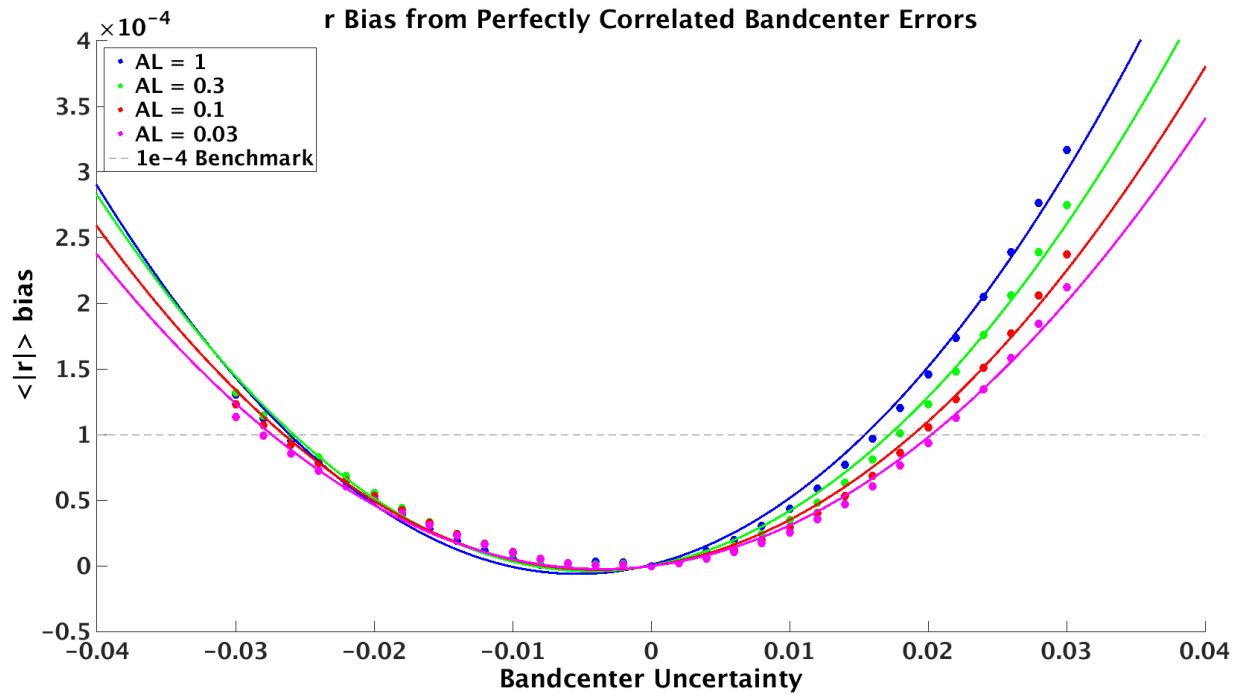


Figure 4.19: Bias on r caused by perfectly correlated bandcenter uncertainties. The points show the calculated values and the lines show a quadratic fit. The various levels of delensing are shown in the different colors with no delensing in blue. The horizontal dashed line shows the benchmark value.

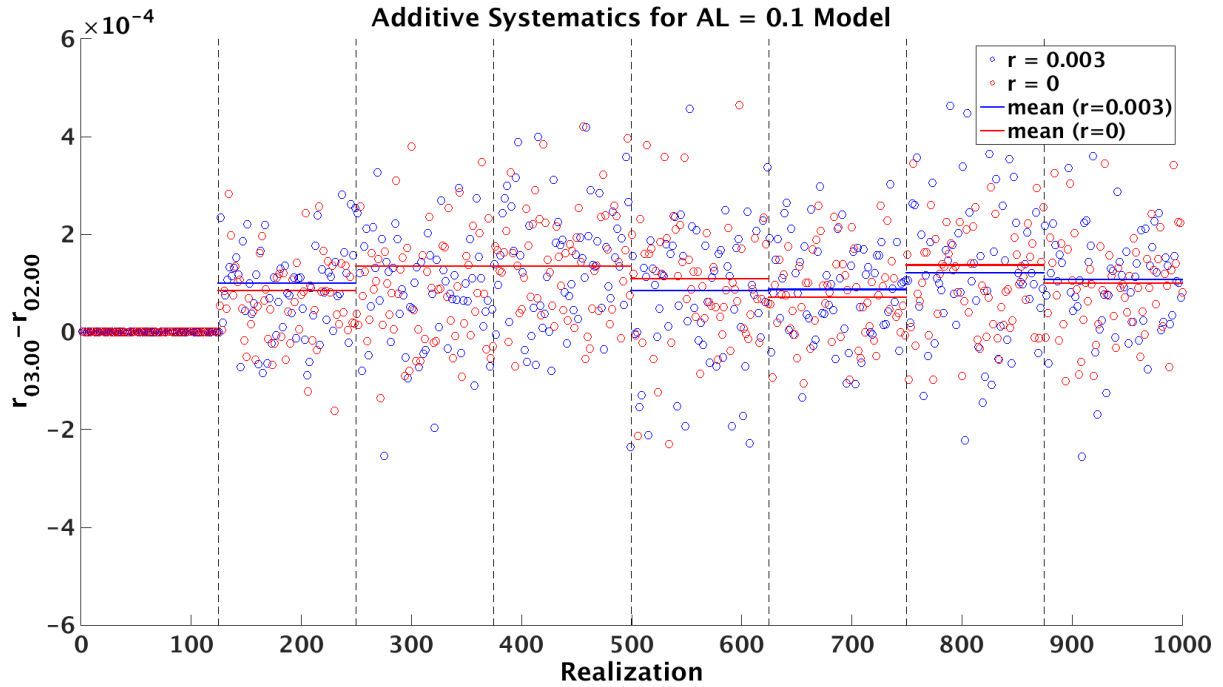


Figure 4.20: Bias on r caused by various types of additive systematics for a lensing debias model of $A_L = 0.1$. The points in red(blue) represent the individual realizations for the $r = 0$ ($r = 0.003$) model. The solid horizontal lines are the mean of the 125 realization section. The dashed vertical lines separate the sections of the different types of systematics.

Chapter 5

Conclusion

Currently, the BICEP/Keck Collaboration offers the best constraints on r in the world at $r < 0.07$ at 95%. The constraint comes from the Bayesian credible interval of BK15 likelihood plot shown in the dashed red line of Figure 4.17. This likelihood was obtained using a maximum likelihood (ML) search described in Section 4.3. Also shown on the same plot is an alternative novel method known as the quadratic estimator (QE) described in Section 4.4. With this new method, we were able to obtain a similar likelihood which didn't rely on a bandpower approximation and which was significantly faster to compute. The quadratic estimator likelihood constrains r to $r < 0.05$ at 95%. Both the ML search and QE methods have a sensitivity of $\sigma(r) = 0.02$ which can be seen in Table 4.2. Looking forward, this new method of using a quadratic estimator will be integrated into the analysis pipeline of the BK Collaboration and be used as an alternative likelihood analysis. Soon to be released, the BK18 data product will have an estimated sensitivity of $\sigma(r) \approx 0.01$. Figure 5.1 shows a projection of the BK Collaboration data as it relates to r .

What is obvious from the figure is that continual integration at a specific frequency increases sensitivity but has diminishing returns. In order to reach the projected sensitivity on r , a multi-frequency observation will be required to disentangle foregrounds. Furthermore, receivers which offer more detectors will increase the sensitivity at the various observing

frequencies. The introduction of BICEP Array (BA) in 2020 allows for the BK Collaboration to reach the projected sensitivity displayed in the figure. The first BA receiver at 30/40GHz is currently operational at the Amundsen-Scott South Pole Station with plans to deploy three more receivers. An essential part of the BA instrument is the Housekeeping system which is used to read out all of the thermistors and provide temperature control. The design of the system is described in Chapter 3. This system has been duplicated several times for the various BA receivers and will be operational for the duration of the BA experiment. By the end of the BA experiment, the BK Collaboration has projected a sensitivity of $\sigma(r) \sim 0.003$.

CMB-S4 is the next stage of CMB experiments. Some of the instrumental systematics were estimated using the QE in Section 4.5. As the future of CMB experiments progress, they will build upon the previous analysis techniques and instrument designs some of which have been discussed in this thesis. With an estimated sensitivity of $\sigma(r) \sim 5 \times 10^{-4}$, CMB-S4 offers a path forward into uncovering the physics of Inflation and the early Universe.

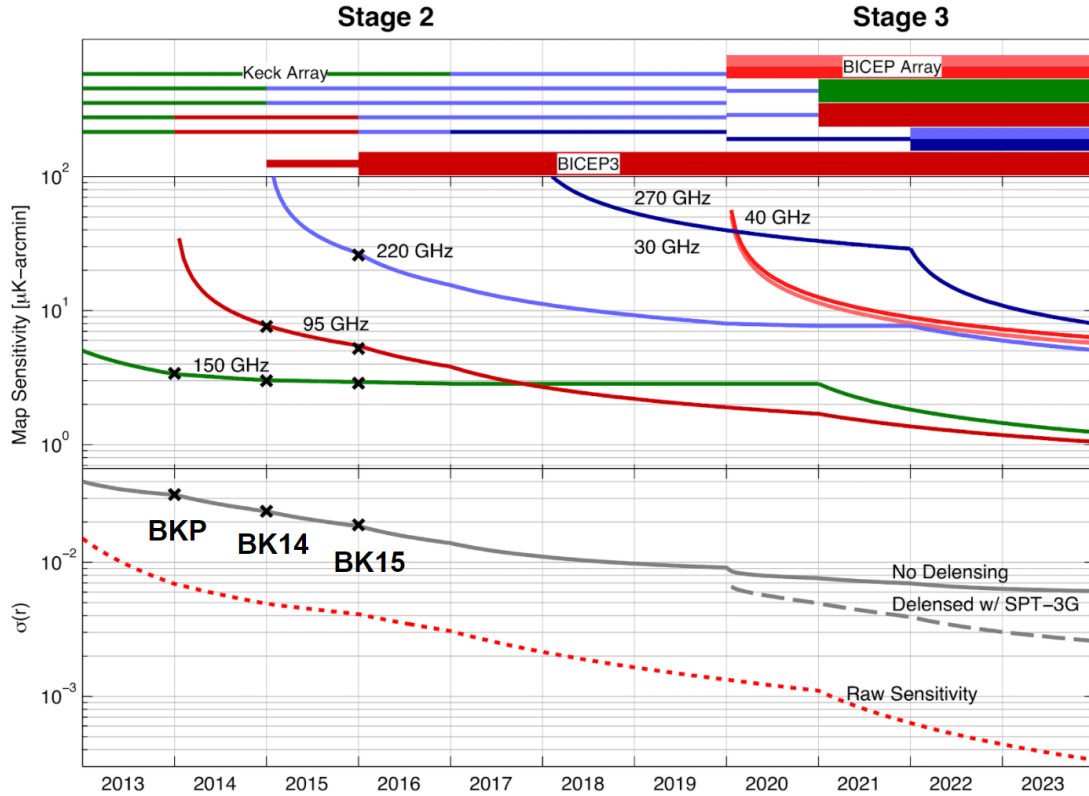


Figure 5.1: BICEP/Keck Collaboration projected sensitivity of r . The x-axis is time in years. The top panel shows a representation of the different observing frequencies and receivers used in the cumulative data. The middle panel shows the map sensitivity at a given frequency as we integrate over time. The bottom panel shows our sensitivity to r in terms of $\sigma(r)$. The solid gray line is a representation of our actual sensitivity and the dashed gray line is how sensitive we will be assuming delensing with South Pole Telescope (SPT-3G). The dashed red line represents our “raw” sensitivity to r in the case of ‘no foregrounds’. The ‘x’s represent the real data products released by the collaboration and the data has matched the prediction very well. It is worth noting that the deployment of additional BICEP Array receivers has been delayed from what is shown above due to the COVID-19 pandemic. Figure courtesy of the BK Collaboration [49].

Bibliography

- [1] Barbara Sue Ryden. *Introduction to Cosmology*. San Francisco: Addison-Wesley, 2003.
- [2] Albert Einstein. “Die Feldgleichungen der Gravitation”. In: *Sitzungsberichte der Königlich Preußischen Akademie der Wissenschaften (Berlin)* (Jan. 1915), pp. 844–847.
- [3] A. Friedmann. “On the Curvature of Space”. In: *General Relativity and Gravitation* 31 (Dec. 1999), p. 1991. DOI: 10.1023/A:1026751225741.
- [4] Edwin Hubble. “A Relation between Distance and Radial Velocity among Extra-Galactic Nebulae”. In: *Proceedings of the National Academy of Science* 15.3 (Mar. 1929), pp. 168–173. DOI: 10.1073/pnas.15.3.168.
- [5] Scott Dodelson. *Modern Cosmology*. 2003.
- [6] R. A. Alpher, H. Bethe, and G. Gamow. “The Origin of Chemical Elements”. In: *Physical Review* 73.7 (Apr. 1948), pp. 803–804. DOI: 10.1103/PhysRev.73.803.
- [7] Ralph A. Alpher and Robert C. Herman. “Remarks on the Evolution of the Expanding Universe”. In: *Physical Review* 75.7 (Apr. 1949), pp. 1089–1095. DOI: 10.1103/PhysRev.75.1089.
- [8] A. A. Penzias and R. W. Wilson. “A Measurement of Excess Antenna Temperature at 4080 Mc/s.” In: *ApJ* 142 (July 1965), pp. 419–421. DOI: 10.1086/148307.
- [9] D. J. Fixsen. “THE TEMPERATURE OF THE COSMIC MICROWAVE BACKGROUND”. In: *The Astrophysical Journal* 707.2 (Nov. 2009), pp. 916–920. ISSN: 1538-

4357. DOI: 10.1088/0004-637x/707/2/916. URL: <http://dx.doi.org/10.1088/0004-637x/707/2/916>.
- [10] D. J. Fixsen et al. “The Cosmic Microwave Background Spectrum from the Full COBE FIRAS Data Set”. In: *ApJ* 473 (Dec. 1996), p. 576. DOI: 10.1086/178173. arXiv: [astro-ph/9605054](https://arxiv.org/abs/astro-ph/9605054) [astro-ph].
- [11] N. Aghanim et al. “Planck2018 results”. In: *Astronomy & Astrophysics* 641 (Sept. 2020), A1. ISSN: 1432-0746. DOI: 10.1051/0004-6361/201833880. URL: <http://dx.doi.org/10.1051/0004-6361/201833880>.
- [12] P. de Bernardis et al. “A flat Universe from high-resolution maps of the cosmic microwave background radiation”. In: *Nature* 404.6781 (Apr. 2000), pp. 955–959. DOI: 10.1038/35010035. arXiv: [astro-ph/0004404](https://arxiv.org/abs/astro-ph/0004404) [astro-ph].
- [13] Wayne Hu and Martin White. “Acoustic Signatures in the Cosmic Microwave Background”. In: *The Astrophysical Journal* 471.1 (Nov. 1996), pp. 30–51. ISSN: 1538-4357. DOI: 10.1086/177951. URL: <http://dx.doi.org/10.1086/177951>.
- [14] Wayne Hu and Martin White. “The Damping Tail of Cosmic Microwave Background Anisotropies”. In: *The Astrophysical Journal* 479.2 (Apr. 1997), pp. 568–579. DOI: 10.1086/303928. URL: <https://doi.org/10.1086/303928>.
- [15] Wayne Hu and Martin White. “A CMB polarization primer”. In: *New Astronomy* 2.4 (Oct. 1997), pp. 323–344. ISSN: 1384-1076. DOI: 10.1016/s1384-1076(97)00022-5. URL: [http://dx.doi.org/10.1016/S1384-1076\(97\)00022-5](http://dx.doi.org/10.1016/S1384-1076(97)00022-5).
- [16] J. M. Kovac et al. “Detection of polarization in the cosmic microwave background using DASI”. In: *Nature* 420.6917 (Dec. 2002), pp. 772–787. ISSN: 1476-4687. DOI: 10.1038/nature01269. URL: <http://dx.doi.org/10.1038/nature01269>.
- [17] Matias Zaldarriaga and Uroš Seljak. “All-sky analysis of polarization in the microwave background”. In: *Physical Review D* 55.4 (Feb. 1997), pp. 1830–1840. ISSN: 1089-4918.

- DOI: 10.1103/physrevd.55.1830. URL: <http://dx.doi.org/10.1103/PhysRevD.55.1830>.
- [18] C. L. Bennett et al. “Nine-year Wilkinson Microwave Anisotropy Probe (WMAP) Observations: Final Maps and Results”. In: *The Astrophysical Journal Supplement* 208.2, 20 (Oct. 2013), p. 20. DOI: 10.1088/0067-0049/208/2/20. arXiv: 1212.5225 [astro-ph.CO].
- [19] Sudeep Das et al. “The Atacama Cosmology Telescope: temperature and gravitational lensing power spectrum measurements from three seasons of data”. In: *Journal of Cosmology and Astroparticle Physics* 2014.4, 014 (Apr. 2014), p. 014. DOI: 10.1088/1475-7516/2014/04/014. arXiv: 1301.1037 [astro-ph.CO].
- [20] Antony Lewis and Anthony Challinor. “Weak gravitational lensing of the CMB”. In: *Physics Reports* 429.1 (June 2006), pp. 1–65. DOI: 10.1016/j.physrep.2006.03.002. arXiv: astro-ph/0601594 [astro-ph].
- [21] Blake D. Sherwin et al. “Two-season Atacama Cosmology Telescope polarimeter lensing power spectrum”. In: *Physical Review D* 95.12, 123529 (June 2017), p. 123529. DOI: 10.1103/PhysRevD.95.123529. arXiv: 1611.09753 [astro-ph.CO].
- [22] E. M. George et al. “A Measurement of Secondary Cosmic Microwave Background Anisotropies from the 2500 Square-degree SPT-SZ Survey”. In: *The Astrophysical Journal* 799.2, 177 (Feb. 2015), p. 177. DOI: 10.1088/0004-637X/799/2/177. arXiv: 1408.3161 [astro-ph.CO].
- [23] R. Keisler et al. “Measurements of Sub-degree B-mode Polarization in the Cosmic Microwave Background from 100 Square Degrees of SPTpol Data”. In: *The Astrophysical Journal* 807.2, 151 (July 2015), p. 151. DOI: 10.1088/0004-637X/807/2/151. arXiv: 1503.02315 [astro-ph.CO].
- [24] K. T. Story et al. “A Measurement of the Cosmic Microwave Background Gravitational Lensing Potential from 100 Square Degrees of SPTpol Data”. In: *The Astrophysical*

- Journal* 810.1, 50 (Sept. 2015), p. 50. DOI: 10.1088/0004-637X/810/1/50. arXiv: 1412.4760 [astro-ph.CO].
- [25] J. W. Henning et al. “Measurements of the Temperature and E-mode Polarization of the CMB from 500 Square Degrees of SPTpol Data”. In: *The Astrophysical Journal* 852.2, 97 (Jan. 2018), p. 97. DOI: 10.3847/1538-4357/aa9ff4. arXiv: 1707.09353 [astro-ph.CO].
- [26] POLARBEAR Collaboration et al. “A Measurement of the Cosmic Microwave Background B-mode Polarization Power Spectrum at Subdegree Scales from Two Years of polarbear Data”. In: *The Astrophysical Journal* 848.2, 121 (Oct. 2017), p. 121. DOI: 10.3847/1538-4357/aa8e9f. arXiv: 1705.02907 [astro-ph.CO].
- [27] BICEP2 and Keck Array Collaborations et al. “BICEP2/Keck Array V: Measurements of B-mode Polarization at Degree Angular Scales and 150 GHz by the Keck Array”. In: *The Astrophysical Journal* 811.2, 126 (Oct. 2015), p. 126. DOI: 10.1088/0004-637X/811/2/126. arXiv: 1502.00643 [astro-ph.CO].
- [28] BICEP2 Collaboration et al. “Improved Constraints on Cosmology and Foregrounds from BICEP2 and Keck Array Cosmic Microwave Background Data with Inclusion of 95 GHz Band”. In: *Physical Review Letters* 116.3, 031302 (Jan. 2016), p. 031302. DOI: 10.1103/PhysRevLett.116.031302. arXiv: 1510.09217 [astro-ph.CO].
- [29] Marc Kamionkowski, Arthur Kosowsky, and Albert Stebbins. “Statistics of cosmic microwave background polarization”. In: *Physical Review D* 55.12 (June 1997), pp. 7368–7388. ISSN: 1089-4918. DOI: 10.1103/physrevd.55.7368. URL: <http://dx.doi.org/10.1103/PhysRevD.55.7368>.
- [30] Uroš Seljak and Matias Zaldarriaga. “Signature of Gravity Waves in the Polarization of the Microwave Background”. In: *Physical Review Letters* 78.11 (Mar. 1997), pp. 2054–2057. ISSN: 1079-7114. DOI: 10.1103/physrevlett.78.2054. URL: <http://dx.doi.org/10.1103/PhysRevLett.78.2054>.

- [31] Alan H. Guth. “Inflationary universe: A possible solution to the horizon and flatness problems”. In: *Phys. Rev. D* 23.2 (Jan. 1981), pp. 347–356. DOI: 10.1103/PhysRevD.23.347.
- [32] Daniel Baumann. *TASI Lectures on Inflation*. 2012. arXiv: 0907.5424 [hep-th].
- [33] Marc Kamionkowski and Ely D. Kovetz. “The Quest for B Modes from Inflationary Gravitational Waves”. In: *Annual Review of Astronomy and Astrophysics* 54.1 (Sept. 2016), pp. 227–269. ISSN: 1545-4282. DOI: 10.1146/annurev-astro-081915-023433. URL: <http://dx.doi.org/10.1146/annurev-astro-081915-023433>.
- [34] Marc Kamionkowski and Arthur Kosowsky. “THE COSMIC MICROWAVE BACKGROUND AND PARTICLE PHYSICS”. In: *Annual Review of Nuclear and Particle Science* 49.1 (Dec. 1999), pp. 77–123. ISSN: 1545-4134. DOI: 10.1146/annurev.nucl.49.1.77. URL: <http://dx.doi.org/10.1146/annurev.nucl.49.1.77>.
- [35] S. Weinberg. *Cosmology*. Cosmology. OUP Oxford, 2008. ISBN: 9780191523601.
- [36] David H. Lyth. “What Would We Learn by Detecting a Gravitational Wave Signal in the Cosmic Microwave Background Anisotropy?” In: *Physical Review Letters* 78.10 (Mar. 1997), pp. 1861–1863. ISSN: 1079-7114. DOI: 10.1103/physrevlett.78.1861. URL: <http://dx.doi.org/10.1103/PhysRevLett.78.1861>.
- [37] P. A. R. Ade et al. “Constraints on Primordial Gravitational Waves Using Planck, WMAP, and New BICEP2/Keck Observations through the 2015 Season”. In: *Physical Review Letters* 121.22 (Nov. 2018). ISSN: 1079-7114. DOI: 10.1103/physrevlett.121.221301. URL: <http://dx.doi.org/10.1103/PhysRevLett.121.221301>.
- [38] A. Lazarian. “Tracing magnetic fields with aligned grains”. In: *Journal of Quantitative Spectroscopy and Radiative Transfer* 106.1-3 (July 2007), pp. 225–256. ISSN: 0022-4073. DOI: 10.1016/j.jqsrt.2007.01.038. URL: <http://dx.doi.org/10.1016/j.jqsrt.2007.01.038>.

- [39] R. Adam et al. “Planck intermediate results. XXX.” In: *Astronomy & Astrophysics* 586 (Feb. 2016), A133. ISSN: 1432-0746. DOI: 10.1051/0004-6361/201425034. URL: <http://dx.doi.org/10.1051/0004-6361/201425034>.
- [40] George B. Rybicki and Alan P. Lightman. *Radiative Processes in Astrophysics*. 1986.
- [41] M.-A. Miville-Deschênes et al. “Separation of anomalous and synchrotron emissions using WMAP polarization data”. In: *Astronomy & Astrophysics* 490.3 (Sept. 2008), pp. 1093–1102. ISSN: 1432-0746. DOI: 10.1051/0004-6361:200809484. URL: <http://dx.doi.org/10.1051/0004-6361:200809484>.
- [42] U. Fuskeland et al. “SPATIAL VARIATIONS IN THE SPECTRAL INDEX OF POLARIZED SYNCHROTRON EMISSION IN THE 9 yrWMAPSKY MAPS”. In: *The Astrophysical Journal* 790.2 (July 2014), p. 104. ISSN: 1538-4357. DOI: 10.1088/0004-637x/790/2/104. URL: <http://dx.doi.org/10.1088/0004-637X/790/2/104>.
- [43] A LEWIS and A CHALLINOR. “Weak gravitational lensing of the CMB”. In: *Physics Reports* 429.1 (June 2006), pp. 1–65. ISSN: 0370-1573. DOI: 10.1016/j.physrep.2006.03.002. URL: <http://dx.doi.org/10.1016/j.physrep.2006.03.002>.
- [44] Wayne Hu and Takemi Okamoto. “Mass Reconstruction with Cosmic Microwave Background Polarization”. In: *The Astrophysical Journal* 574.2 (Aug. 2002), pp. 566–574. ISSN: 1538-4357. DOI: 10.1086/341110. URL: <http://dx.doi.org/10.1086/341110>.
- [45] A. Manzotti et al. “CMB PolarizationB-mode Delensing with SPTpol andHerschel”. In: *The Astrophysical Journal* 846.1 (Aug. 2017), p. 45. ISSN: 1538-4357. DOI: 10.3847/1538-4357/aa82bb. URL: <http://dx.doi.org/10.3847/1538-4357/aa82bb>.
- [46] Chao-Lin Kuo. “Assessments of Ali, Dome A, and Summit Camp for mm-wave Observations Using MERRA-2 Reanalysis”. In: *The Astrophysical Journal* 848.1 (Oct. 2017), p. 64. ISSN: 1538-4357. DOI: 10.3847/1538-4357/aa8b74. URL: <http://dx.doi.org/10.3847/1538-4357/aa8b74>.

- [47] Douglas P. Finkbeiner, Marc Davis, and David J. Schlegel. “Extrapolation of Galactic Dust Emission at 100 Microns to Cosmic Microwave Background Radiation Frequencies Using FIRAS”. In: *ApJ* 524.2 (Oct. 1999), pp. 867–886. DOI: 10.1086/307852. arXiv: astro-ph/9905128 [astro-ph].
- [48] P. A. R. Ade et al. “BICEP2. II. EXPERIMENT AND THREE-YEAR DATA SET”. In: *The Astrophysical Journal* 792.1 (Aug. 2014), p. 62. ISSN: 1538-4357. DOI: 10.1088/0004-637x/792/1/62. URL: <http://dx.doi.org/10.1088/0004-637X/792/1/62>.
- [49] Howard Hui et al. “BICEP Array: a multi-frequency degree-scale CMB polarimeter”. In: *Millimeter, Submillimeter, and Far-Infrared Detectors and Instrumentation for Astronomy IX*. Ed. by Jonas Zmuidzinas and Jian-Rong Gao. Vol. 10708. Society of Photo-Optical Instrumentation Engineers (SPIE) Conference Series. July 2018, p. 1070807. DOI: 10.1117/12.2311725. arXiv: 1808.00568 [astro-ph.IM].
- [50] Michael Crumrine et al. “BICEP Array cryostat and mount design”. In: *Millimeter, Submillimeter, and Far-Infrared Detectors and Instrumentation for Astronomy IX*. Ed. by Jonas Zmuidzinas and Jian-Rong Gao. Vol. 10708. Society of Photo-Optical Instrumentation Engineers (SPIE) Conference Series. July 2018, p. 107082D. DOI: 10.1117/12.2312829. arXiv: 1808.00569 [astro-ph.IM].
- [51] Lionel Duband and Bernard Collaudin. “Sorption coolers development at CEA-SBT”. In: *Cryogenics* 39.8 (Dec. 1999), pp. 659–663. DOI: 10.1016/S0011-2275(99)00066-1.
- [52] K. D. Irwin and G. C. Hilton. “Transition-edge sensors”. In: *Cryogenic particle detection*. Ed. by C. Enss. Vol. 99. Topics in applied physics. Berlin, Germany: Springer, 2005, pp. 63–150.
- [53] C. Zhang et al. “Characterizing the Sensitivity of 40 GHz TES Bolometers for BICEP Array”. In: *Journal of Low Temperature Physics* 199.3-4 (Feb. 2020), pp. 968–975. DOI: 10.1007/s10909-020-02411-8. arXiv: 2002.05219 [astro-ph.IM].

- [54] J. A. Grayson et al. “BICEP3 performance overview and planned Keck Array upgrade”. In: *Millimeter, Submillimeter, and Far-Infrared Detectors and Instrumentation for Astronomy VIII*. Ed. by Wayne S. Holland and Jonas Zmuidzinas. Vol. 9914. Society of Photo-Optical Instrumentation Engineers (SPIE) Conference Series. July 2016, 99140S. DOI: 10.1117/12.2233894. arXiv: 1607.04668 [astro-ph.IM].
- [55] K. D. Irwin et al. “Time-division SQUID multiplexers”. In: *Low Temperature Detectors*. Ed. by F. Scott Porter et al. Vol. 605. American Institute of Physics Conference Series. Feb. 2002, pp. 301–304. DOI: 10.1063/1.1457650.
- [56] E. S. Battistelli et al. “Functional Description of Read-out Electronics for Time-Domain Multiplexed Bolometers for Millimeter and Sub-millimeter Astronomy”. In: *Journal of Low Temperature Physics* 151.3-4 (May 2008), pp. 908–914. DOI: 10.1007/s10909-008-9772-z.
- [57] L. Moncelsi et al. “Receiver development for BICEP Array, a next-generation CMB polarimeter at the South Pole”. In: *Society of Photo-Optical Instrumentation Engineers (SPIE) Conference Series*. Vol. 11453. Society of Photo-Optical Instrumentation Engineers (SPIE) Conference Series. Dec. 2020, p. 1145314. DOI: 10.1117/12.2561995. arXiv: 2012.04047 [astro-ph.IM].
- [58] Justin Willmert. “Constraining Inflationary B-modes with the BICEP/KECK Array Telescopes”. Part of the BK Collaboration. PhD thesis. University of Minnesota, Nov. 2019.
- [59] Jamie Tolan. “Testing Inflationary Cosmology with BICEP2 and the Keck Array”. Part of the BK Collaboration. PhD thesis. Stanford University, Aug. 2014.
- [60] BICEP2 Collaboration et al. “BICEP2/Keck Array XI: Beam Characterization and Temperature-to-Polarization Leakage in the BK15 Data Set”. In: *ApJ* 884.2, 114 (Oct. 2019), p. 114. DOI: 10.3847/1538-4357/ab391d. arXiv: 1904.01640 [astro-ph.IM].

- [61] Bicep2 Collaboration et al. “Bicep2 III: Instrumental Systematics”. In: *ApJ* 814.2, 110 (Dec. 2015), p. 110. DOI: 10.1088/0004-637X/814/2/110. arXiv: 1502.00608 [astro-ph.IM].
- [62] BICEP2 Collaboration et al. “Detection of B-Mode Polarization at Degree Angular Scales by BICEP2”. In: *Physical Review Letters* 112.24, 241101 (June 2014), p. 241101. DOI: 10.1103/PhysRevLett.112.241101. arXiv: 1403.3985 [astro-ph.CO].
- [63] J. Cornelison et al. “Polarization calibration of the BICEP3 CMB polarimeter at the South Pole”. In: *Society of Photo-Optical Instrumentation Engineers (SPIE) Conference Series*. Vol. 11453. Society of Photo-Optical Instrumentation Engineers (SPIE) Conference Series. Dec. 2020, p. 1145327. DOI: 10.1117/12.2562905. arXiv: 2012.05934 [astro-ph.IM].
- [64] E. E. Haller, K. M. Itoh, and J. W. Beeman. “Neutron Transmutation Depot (NTD) Germanium Thermistors for Submillimetre Bolometer Applications”. In: *Submillimetre and Far-Infrared Space Instrumentation*. Ed. by E. J. Rolfe and G. Pilbratt. Vol. 388. ESA Special Publication. Dec. 1996, p. 115.
- [65] S. J. Benton et al. “BLASTbus electronics: general-purpose readout and control for balloon-borne experiments”. In: *Ground-based and Airborne Telescopes V*. Ed. by Larry M. Stepp, Roberto Gilmozzi, and Helen J. Hall. Vol. 9145. International Society for Optics and Photonics. SPIE, 2014, pp. 317–327. URL: <https://doi.org/10.1117/12.2056693>.
- [66] K.J. King and S.J. Leeks, ed. *SPIRE Instrument User Manual*. ref: SPIRE-RAL-PRJ002395. Herschel-SPIRE. Apr. 2009. URL: <https://www.cosmos.esa.int/documents/12133/1035800/SPIRE+Instrument+User+Manual>.
- [67] J. R. Bond, A. H. Jaffe, and L. Knox. “Radical Compression of Cosmic Microwave Background Data”. In: *The Astrophysical Journal* 533.1 (Apr. 2000), pp. 19–37. ISSN: 1538-4357. DOI: 10.1086/308625. URL: <http://dx.doi.org/10.1086/308625>.

- [68] Victor Buza. “Constraining Primordial Gravitational Waves Using Present and Future CMB Experiments”. Part of the BK Collaboration. PhD thesis. Harvard University, May 2019.
- [69] N. Krachmalnicoff et al. “S-PASS view of polarized Galactic synchrotron at 2.3 GHz as a contaminant to CMB observations”. In: *Astronomy & Astrophysics* 618 (Oct. 2018), A166. ISSN: 1432-0746. DOI: 10.1051/0004-6361/201832768. URL: <http://dx.doi.org/10.1051/0004-6361/201832768>.
- [70] P. A. R. Ade et al. “Planck intermediate results. XXII. Frequency dependence of thermal emission from Galactic dust in intensity and polarization”. In: *Astronomy & Astrophysics* 576 (Apr. 2015), A107. ISSN: 1432-0746. DOI: 10.1051/0004-6361/201424088. URL: <http://dx.doi.org/10.1051/0004-6361/201424088>.
- [71] Samira Hamimeche and Antony Lewis. “Likelihood analysis of CMB temperature and polarization power spectra”. In: *Physical Review D* 77.10 (May 2008). ISSN: 1550-2368. DOI: 10.1103/physrevd.77.103013. URL: <http://dx.doi.org/10.1103/PhysRevD.77.103013>.
- [72] C. Lawrence et al. (Cosmic Microwave Background Stage 4 Concept Definition Task Force Collaboration). *Report to the astronomy and astrophysics advisory committee*. Oct. 2017. URL: https://www.nsf.gov/mps/ast/aaac/cmb_s4/report/CMBS4_final_report_NL.pdf.
- [73] B. Thorne et al. “The Python Sky Model: software for simulating the Galactic microwave sky”. In: *Monthly Notices of the Royal Astronomical Society* 469.3 (May 2017), pp. 2821–2833. ISSN: 1365-2966. DOI: 10.1093/mnras/stx949. URL: <http://dx.doi.org/10.1093/mnras/stx949>.
- [74] A G Kritsuk, S D Ustyugov, and M L Norman. “The structure and statistics of interstellar turbulence”. In: *New Journal of Physics* 19.6 (June 2017), p. 065003. ISSN: 1367-

2630. DOI: 10.1088/1367-2630/aa7156. URL: <http://dx.doi.org/10.1088/1367-2630/aa7156>.
- [75] Brandon Hensley. “On the Nature of Interstellar Grains”. <http://arks.princeton.edu/ark:/88435/dsp01> PhD thesis. Princeton University, Nov. 2015.
- [76] Gary J. Feldman and Robert D. Cousins. “Unified approach to the classical statistical analysis of small signals”. In: *Physical Review D* 57.7 (Apr. 1998), pp. 3873–3889. ISSN: 1089-4918. DOI: 10.1103/physrevd.57.3873. URL: <http://dx.doi.org/10.1103/PhysRevD.57.3873>.
- [77] Kevork N. Abazajian et al. *CMB-S4 Science Book, First Edition*. 2016. arXiv: 1610.02743 [astro-ph.CO].
- [78] S4 Collaboration et al. *CMB-S4: Forecasting Constraints on Primordial Gravitational Waves*. 2020. arXiv: 2008.12619 [astro-ph.CO].

Appendix A

Appendix

A.1 NTD Tuning

As stated in Section 3.5.3, each of the NTD bias cards need to be manually tuned for each channel. The NTD is part of a bridge topology (Figure 3.12) in which there are two tunable biases. The bias on the nulling resistor (NR) is meant to cancel out the bias on the NTD when the focal plane is at cold operating temperatures. In this appendix, we will give a procedure for how to tune the NTDs. Before going over the procedure, here are some helpful notes about the tuning:

- The bias frequency is $f_{bias} \approx 408Hz$ ¹
- $max(V_{bias}) \approx 1.2V$, $min(V_{bias}) = 0V$
- NTD warmer = lower resistance — NTD colder = higher resistance
- Approx. dynamic temperature range of NTD: $250mK(4.97M\Omega)$ to $500mK(101K\Omega)$
- The NTD resistance is $\sim 2.7M\Omega$ at $275mK$
- The bridge resistors (BR) are $15M\Omega$
- The load resistors (LR) are $3.96M\Omega$

In order to start tuning the biases, there should be a first pass on tuning the amplitudes for two reasons: (1) there needs to be a non-zero amplitude to tune the phases and (2) any

¹This value might be changed in future iterations to solve the aliasing problem.

unused bias channels should be tuned to a zero amplitude in order to prevent beat frequencies and cross-talk. The amplitudes can be tuned via a small trimmer potentiometer (trimpot) with a 12-turn screw where a clockwise turn will decrease the amplitude and a counter-clockwise turn will increase the amplitude. At maximum amplitude, the bias is $\sim 1.2V$ and the minimum is $0V$. An amplitude of $\sim 750mV$ is appropriate for an initial amplitude tuning, although this is just a guideline. Figure A.1 shows the location of the trimpots and standard headers used for tuning both the amplitude and phase.

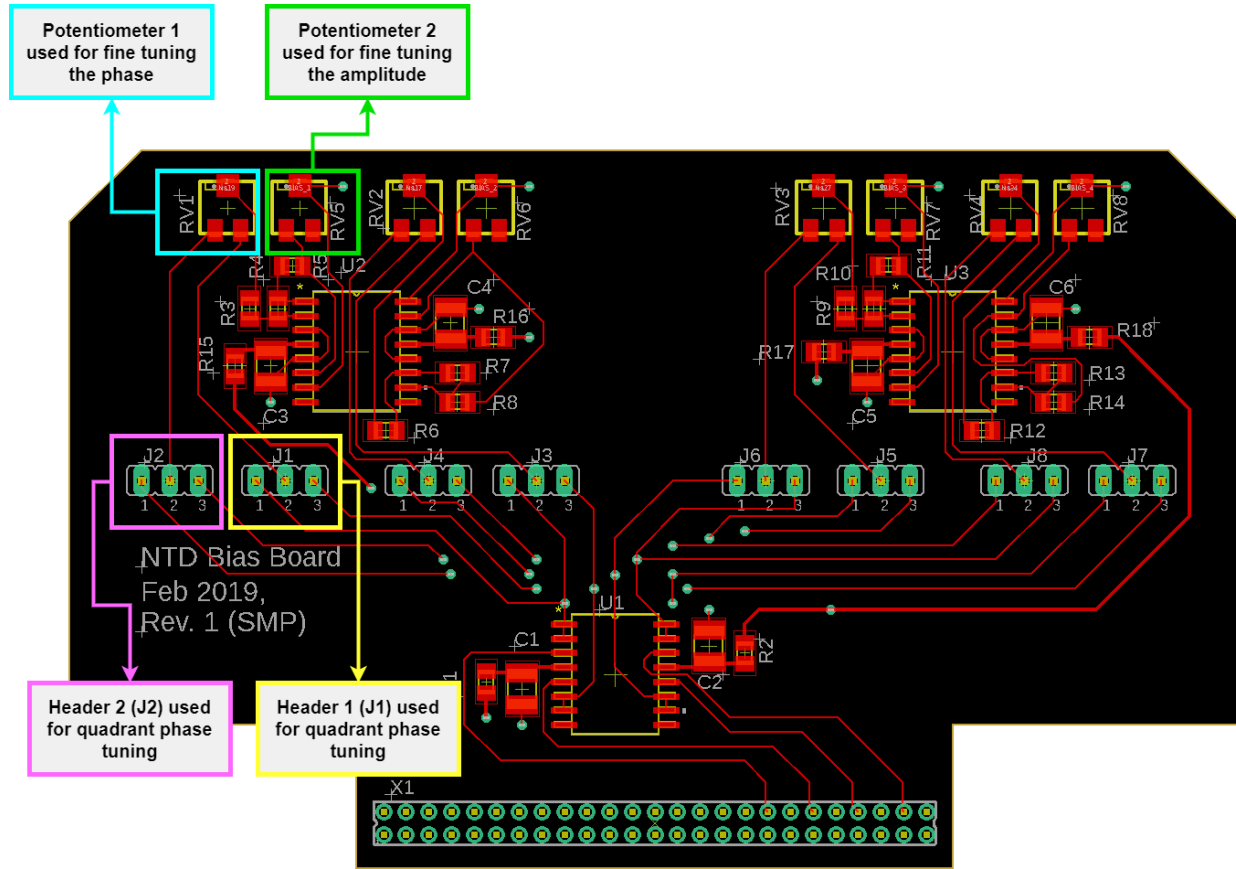


Figure A.1: NTD Bias daughter card PCB with tuning labels. Each NTD Bias daughter card has four channels and the labeled parts are all for Ch.A. The other channels (Ch.B, Ch.C, and Ch.D) follow the same pattern.

After a first pass at the amplitude, the next step is to tune the phase because it will cause a change in the amplitude (Section 3.3.6). In order to tune the phase, there are a set of two 3-pin standard headers for each channel. A shorting jumper is placed on each

of the standard headers to achieve the desired quadrant of the phase. Figure A.2 shows a diagram of how to place the jumpers in order to get the four resulting phase quadrants. In

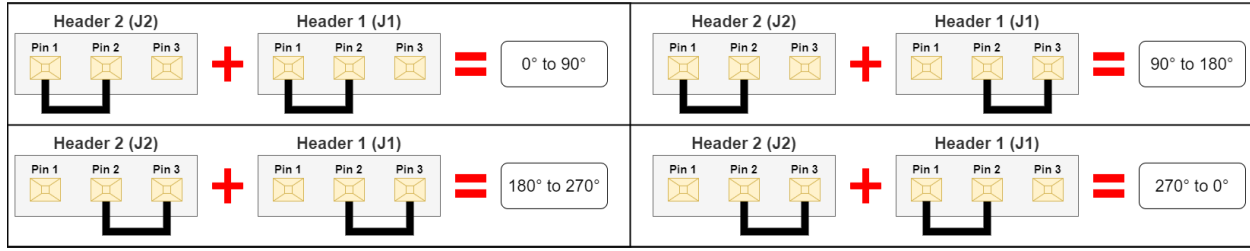


Figure A.2: NTD Phase tuning jumper configurations.

most cases, the NTD and NR are within a few degrees of each other so it is fitting to put the jumpers in the 0° to 90° configuration for both of the biases. In order to see the phase tuning in real time, it is suggested to set up an oscilloscope which is AC triggered via the original 0° oscillator bias signal (pre NTD Bias processing). Because we want to null out the signals, we need to look at the bias output after the bridge circuit. The two biases and their resulting difference can be probed by using the NTD Lock-in daughter card. There are four test points for each lock-in channel². In the list below is shown the test point labels for Ch.A:

- **INA-** – The output bias of the nulling resistor.
- **INA+** – The output bias of the NTD.
- **ADIFF** – The resulting difference between the two biases. This difference is multiplied by a gain of 173.
- **GND** – The ground of the NTD Lock-in daughter card.

It is suggested that all three channels ('IN-', 'IN+', and 'DIFF') are looked at in order to match the phase of the two biases. The 'DIFF' test point is very useful in matching the bias signals but be aware that it goes through a large gain.

After matching the phase of the two bias signals it is time to match the amplitudes. The amplitudes, after going through the bridge circuit, will have an amplitude somewhere in the range of $50mV$ to $150mV$. Although there is no precise target amplitude for biasing,

²One lock-in channel is the result of two bias channels.

a NTD bias amplitude of $60mV$ or greater is appropriate for our applications. There have been some instances of distortion in the bias signals which can make it difficult to match both the phase and amplitude at the same time. A possible fix for this might be to add a 0Ω grounding resistor onto the Motherboard in the locations labeled ‘RGND6’, ‘RGND7’, ‘RGND8’, ‘RGND9’, or some combination of these four. If the distortion is still not fixed, then just try to null the biases as best as possible.

A.2 Cernox Daughter Card Flavors

As stated in Section 3.5.5, there are several different ‘flavors’ of the Cernox daughter cards to account for the target impedance range of the different variants of the Cernox thermistors. For easier readability, I have duplicated Table 3.2 in the table below. These different variants of Cernox thermistors were present only in the BA1 receiver because future receivers used only one variant of Cernox for simplicity (Flavor0).

Cernox Daughter Card Flavor	Target Impedance Range [Ω]
Flavor 0	0.4K - 4K
Flavor 1	10K - 30K
Flavor AB	20K - 30K
Flavor 2	50K - 110K

Target Ranges for different flavors of Cernox daughter cars. Note: Flavor AB was an early flavor modification and the Flavor 1 board is now a more appropriate version of the board (Duplicate of Table 3.2).

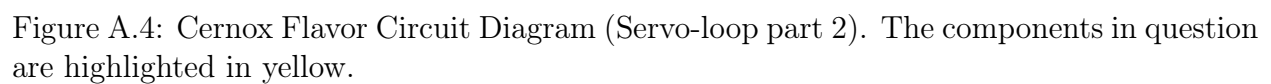
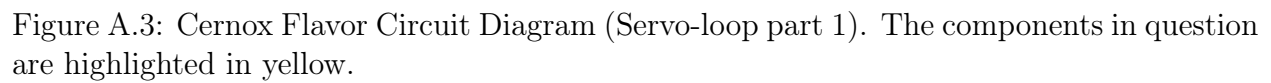
This Appendix will give the exact resistors and capacitors (and their values) to replace in the Cernox daughter cards in order to make the different flavors as well as the resulting gains and time constants. It is worth noting that there are two revisions of the Cernox board: Cernox Rev.1 (Feb 2019) and Cernox Rev.2 (Jun 2019). Cernox Rev.1 contains the outdated logarithmic output and Cernox Rev.2 is the most current revision of the BA Cernox daughter card at the time of writing this (July 2021). While there are some differences between the circuits, all of the components in question for the different flavors remain the same, i.e.,

Table A.1 is applicable for both revisions. A slight bookkeeping complication arises from the fact that there are two channels per board. This means that each Cernox daughter card component will have a Ch.A and Ch.B component. Both of the channels are shown in the table.

Component Label Ch.A (Ch.B)	Flavor 0 Values	Flavor 1 Values	Flavor AB Values	Flavor 2 Values
R21 (R93)	100 Ω	100 Ω	1KΩ	100 Ω
R24 (R96)	22K Ω	10KΩ	51KΩ	10KΩ
C19 (C45)	1 μF	10μF	1 μF	10μF
R41 (R113)	100K Ω	1MΩ	100K Ω	1MΩ
R46 (R118)	10K Ω	10K Ω	10K Ω	1MΩ
τ	0.1s	10s	0.1s	10s
R_{sense}	400K Ω	400K Ω	400K Ω	1.39MΩ
G_{loop}	109395	49995	25754	49995
R70 (R142)	open	1KΩ	open	1KΩ
R71 (R143)	0 Ω	1KΩ	0 Ω	1KΩ
R82 (R154)	10K Ω	1KΩ	22KΩ	1KΩ
R84 (R156)	10K Ω	1KΩ	22KΩ	1KΩ
G_{pl}	22	8	46	8

Table A.1: Cernox Flavor Circuit Components. The components that are changed with respect to the default Flavor0 are highlighted in gray. The top half of the table (R21 through G_{loop}) shows the components which are part of the servo-loop stages of the circuit. The bottom half of the table (R70 through G_{pl}) shows the components which are part of the post lock-in part of the circuit.

Figures A.3, A.4, and A.5 show the circuit diagrams for the parts of the circuit where components need to be modified. The components in question are highlighted in yellow. The circuit diagrams are shown for Ch.A (Cernox Rev. 2) however, Ch.B will look identical other than the component number.



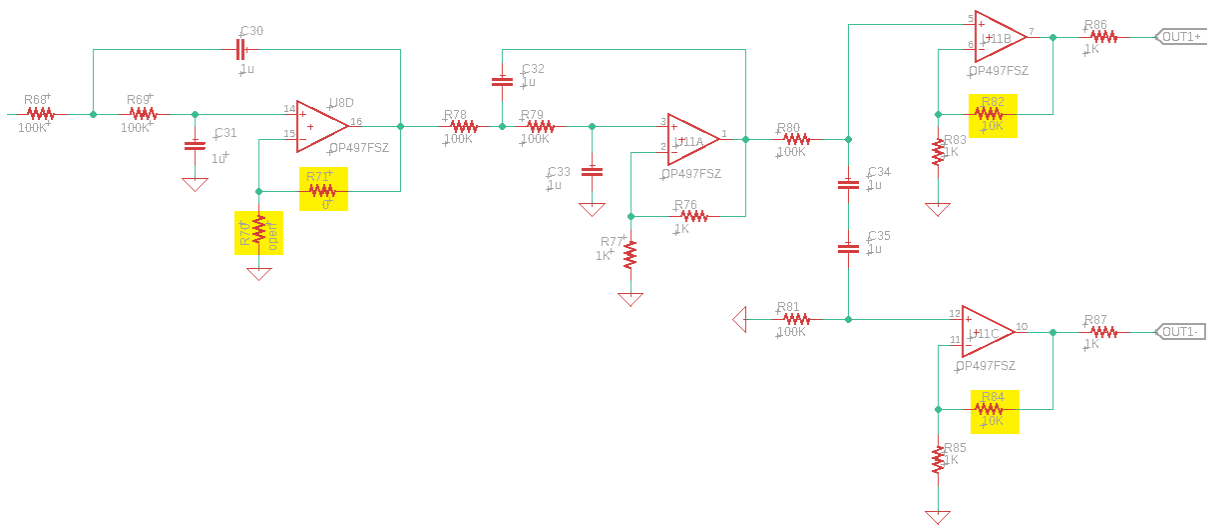


Figure A.5: Cernox Flavor Circuit Diagram (Post Lock-in). The components in question are highlighted in yellow.